Clathrin-Mediated Endocytosis as a Marker of Cell Membrane Tension in Cultured Cells and Developing Organisms

Dissertation

Presented in Partial Fulfillment of the Requirements for the Degree Doctor of Philosophy in the Graduate School of The Ohio State University

By

Joshua Paul Ferguson, M.S., B.S.

Graduate Program in Physics

The Ohio State University

2018

Dissertation Committee:

Dr. Comert Kural, Advisor

Dr. Michael Poirier

Dr. Sooryakumar Ratnasingham

Dr. Ralf Bundschuh

Copyrighted by

Joshua Paul Ferguson

2018

Abstract

Individual cells decipher and react to both their chemical and mechanical environment. Clathrin-mediated endocytosis (CME) is a major process by which cells internalize macromolecules. The triskelion-shaped clathrin protein assembles on the membrane as a spherical lattice enveloping the membrane until scission begets internalization. The membrane curvature generated by the invaginations during endocytosis associate CME with the mechanical environment of the cell. Fluorescence microscopy is used to study the dynamics of CME, and in particular to discern the time it takes for CME events to complete (i.e. their lifetime). It is our hypothesis that the lifetime of CME events relates inversely to the cell membrane tension. We will support this hypothesis with live-cell imaging on glass substrates and in living organisms. We suggest a new methodology for studying CME dynamics that enables higher spatial and temporal resolution than lifetime analysis. We will also characterize the tension response of CME by using various cell manipulation techniques. In addition, we will demonstrate the ability of CME dynamics to predict cell movement and relate gradients in clathrin coat growth rates to previously established tension gradients in cultured cells and living organisms. Finally, we will demonstrate that this process is in a state of continual curvature generation.

Acknowledgments

There have been a lot of people behind this endeavor so to keep things organized I am going to go chronologically, which must start out with my parents. They have been an endless source of love and encouragement. They instilled in me an independence that is necessary for succeeding in research. Additionally, my grandma and great-grandma have played no small part in generating a stable environment for me to discover the world and provide for me a wider range of perspectives.

My love for science has always been present, as I would seek out science-oriented documentary series on cable TV, but I would not have been able to put that passion into a career were it not for my high school physics teacher, Tim Morrison. The entire science department at Parkway South High School was a joy to learn from, but Mr. Morrison (as I knew him) is one of the kindest and most inspiring people I have had the pleasure to meet. I probably would have ended up majoring in science no matter what, but there is no doubt Mr. Morrison had a dominant role to play in my choice of physics.

My college career was lacking in strong direction. Once put on the path of physics I knew I would eventually make it to graduate school, but I must thank Dr. Dan Kosik for demonstrating the brilliant precision hidden in the mathematics of physics. Every class

with him was a joy in the specificity of the subject. He was a rather reserved man, but he was endlessly impressive in the knowledge that he would bring to the classroom.

Prior to entering graduate school, I contacted researchers at OSU to gain some lab experience that I failed to receive at my liberal arts college. Dr. KK Gan accepted me into his lab for the summer and I gained my first insight into the profession of physics. He has since provided me additional opportunities to learn, via helping his son in a science fair. He has also made an effort to chat with me while passing in the hallways, which is more than can be said for most people outside of my group.

A few years after entering graduate school I met my girlfriend, Dr. Sara Kubera. She has provided me with more joy and satisfaction in my life than anything else. Her support and love keep me going as the realities of research try their best to beat me down.

Finally, it almost goes without saying that I would like to thank the people of my group: my advisor, Dr. Comert Kural, and my group mates, Nathan Willy and Scott Huber. I did not make many friends in my first year of graduate school, but if I had, Nathan Willy would have been the person to whom I would have joined myself. As fortune would have it, we ended up in the same group and have been fast friends and close colleagues. We have worked so closely that you will find his name mentioned repeatedly in this dissertation, as it is nearly impossible to separate our work.

Vita

May 2008……Parkway South High School, St. Louis, MO

December 2011……B.S., Physics, Math Minor, Butler University, Indianapolis, IN

Publications

Ferguson, J.P., Willy, N.M., Heidotting, S.P., Huber, S.D., Webber, M.J., and Kural, C. (2016). Deciphering dynamics of clathrin-mediated endocytosis in a living organism. J. Cell Biol. *214*, 347–358.

Willy, N.M., Ferguson, J.P., Huber, S.D., Heidotting, S.P., Aygün, E., Wurm, S.A., Johnston-Halperin, E., Poirier, M.G., and Kural, C. (2017). Membrane mechanics govern spatiotemporal heterogeneity of endocytic clathrin coat dynamics. Mol. Biol. Cell *28*, 3480–3488.

Ferguson, J.P., Huber, S.D., Willy, N.M., Aygün, E., Goker, S., Atabey, T., and Kural, C. (2017). Mechanoregulation of clathrin-mediated endocytosis. J. Cell Sci. *130*, 3631–3636.

Fields of Study

Major Field: Physics

Table of Contents

Abstract ii

Acknowledgments iii

Vita v

Table of Contents vi

List of Figures xi

List of Abbreviations/Jargon xiv

Chapter 1 Introduction 1

1.1 Details of Clathrin Formation 2

1.2 Data Acquisition 3

1.3 Plasma Membrane Tension Effects on CME Dynamics 7

Chapter 2 Deciphering Dynamics of Clathrin-Mediated Endocytosis in a Living Organism 10

2.1 Abstract 10

2.2 Introduction 11

2.3 Results 13

2.3.1 CCS growth rates are robust reporters of CME dynamics 13

2.3.2 Accuracy of growth rate distributions does not depend on determining complete traces of CCSs 20

2.3.3 Spatiotemporal variations in CME dynamics can be resolved in real time using CCS growth rates 22

2.3.4 CCS intensity profiles can be reproduced from growth rate distributions 25

2.3.5 CME dynamics slow down during dorsal closure of Drosophila embryos 28

2.4 Discussion 33

2.5 Materials and Methods 36

2.5.1 Fluorescence imaging 36

2.5.2 Micropipette Aspiration 37

2.5.3 Single-particle tracking 37

2.5.4 3D tracking of CCSs within amnioserosa tissues 40

2.5.5 Classification of apical and basal CCSs and blobs 40

2.5.6 Determining amnioserosa cell boundaries 41

2.5.7 Growth rate distributions 41

2.5.8 Hierarchical clustering of intensity profiles and library lookup 42

2.7 Acknowledgements 43

Chapter 3 Mechanoregulation of clathrin-mediated endocytosis 44

3.1 Abstract 44

3.2 Introduction 45

3.3 Results 45

3.4 Discussion 54

3.5 Materials and Methods 57

3.5.1 Cell culture, reagents and fluorescence imaging 57

3.5.2 Squeezing, micropipette aspiration and osmotic shock 58

3.5.3 Single-particle tracking 60

Chapter 4 Membrane mechanics govern spatiotemporal heterogeneity of endocytic clathrin coat dynamics 62

4.1 Abstract 62

4.2 Introduction 63

4.3 Results 63

4.3.1 Clathrin coat dynamics in spreading and migrating cells 66

4.3.2 Spatiotemporal variations in clathrin dynamics of Drosophila embryos 74

4.4 Discussion 77

4.5 Materials and Methods 78
4.5.1 Cell culture and fluorescence microscopy 78
4.5.2 Fly strains and in vivo imaging 79
4.5.3 Two-dimensional tracking of clathrin-coated structures 80
4.5.4 Three-dimensional tracking of clathrin-coated structures 81
4.5.5 Growth rate distributions 81
4.5.6 Lifetime maps and dipole vectors 82
4.5.7 Tether force measurements 83
4.7 Acknowledgements 84
Chapter 5 Curvature Generation by Endocytic Clathrin Coats 85
5.1 Abstract 85
5.2 Introduction 86
5.3 Results 89
5.4 Discussion 95
5.5 Materials and Methods 97
5.5.1 Cell Culture 97
5.5.2 Drosophila embryos 98
5.5.3 TIRF-SIM 98

5.5.4 Image Analysis 99

5.7 Acknowledgements 103

Chapter 6 Conclusions and Future Work 104

Bibliography 108

Appendix A Micropipette Aspiration 117

Appendix B Three Dimensional Tracking 120

List of Figures

Figure 1.1 Electron microscopy images of clathrin. 2

Figure 1.2 Electron microscopy image of curved clathrin pits, and flat clathrin plaques. . 3

Figure 1.3 Time course of clathrin-mediated endocytosis. 4

Figure 1.4 Schematic of spinning disk confocal microscopy. 6

Figure 1.5 Membrane tethering. 8

Figure 2.1 Determining CCS growth rate distributions. 14

Figure 2.2 Using growth rate histograms as reporters of clathrin dynamics. 16

Figure 2.3 Hierarchical clustering of CCS traces. 18

Figure 2.4 CCSs in proximity of substrate adhesion sites have reduced dynamics. 19

Figure 2.5 Growth rate analysis does not depend on determining the complete traces of CCSs. 21

Figure 2.6 CCS dynamics in cholesterol-depleted cells. 23

Figure 2.7 Real-time monitoring of CCS dynamics in cholesterol-depleted cells. 24

Figure 2.8 A novel analytical toolbox for CME dynamics. 26

Figure 2.9 Determining CCS intensity profiles using growth rate distributions. 27

Figure 2.10 3D tracking of CCSs in apical and basal surfaces of Drosophila amnioserosa. 29

Figure 2.11. CCS motility in cultured cells and Drosophila embryos. 31
Figure 2.12 CME dynamics in Drosophila amnioserosa. 32
Figure 2.13 Flat CCSs and clathrin-coated pits. 35
Figure 2.14 Classification of CCS traces. 39
Figure 3.1 Aspiration of the plasma membrane slows down clathrin coat dynamics. 46
Figure 3.2 Cell squeezing induces fast and reversible alterations in clathrin coat dynamics. 48
Figure 3.3 Growth rate histograms of cell compression. 49
Figure 3.4 Recovery from cell compression. 50
Figure 3.5 Hypotonic swelling inhibits clathrin coat dynamics temporarily. 51
Figure 3.6 Actin dynamics mediate the inward movement of clathrin coats prior to disassembly. 53
Figure 3.7 Compression is less than in developmental processes. 56
Figure 4.1 Monitoring mechanoregulation of clathrin coat dynamics in real time. 65
Figure 4.2 Clathrin coat dynamics reflect changing membrane tension throughout cell spreading. 68
Figure 4.3 Heterogeneous clathrin dynamics maps the tension gradient in protruding cells. 71
Figure 4.4 Heterogeneous CME during in vitro and in vivo cell migration. 74
Figure 4.5 Spatiotemporal variations in clathrin dynamics can be detected within tissues of Drosophila embryo. 77

Figure 5.1 Flat-to-curved transition necessitates a major change in the projected area of clathrin coats. 88
Figure 5.2 TIRF-SIM allows analysis of clathrin-coated pit formation in cultured cells and in tissues of Drosophila embryos with high spatiotemporal resolution. 90
Figure 5.3 Clathrin coats reach maximum projected area by formation of pits. 92
Figure 5.4 Clathrin-coated pits have the maximum footprint. 93
Figure 5.5 Average of all images in a decile. 94
Figure 5.6 Examples of rejected traces. 96
Figure 5.7 User selection of incomplete edge finding. 100
Figure 5.8 Demonstration of temporal interpolation. 102
Figure 5.9 Radial kymographs for each cell type. 103

List of Abbreviations/Jargon

AP2: Clathrin adaptor complex

AS: Amnioserosa

CLC: Clathrin light chain

CME: Clathrin mediated endocytosis

CCP: Clathrin-coated pit

CCS: Clathrin-coated structure

EGFP: Enhanced green fluorescent protein

EMCCD: Electron-multiplying charge-coupled device

FBS: Fetal bovine serum

IMS: Integrated movie segment

In vivo: In a living organism

In vitro: An experiment done outside of a living organism (e.g. an individual cell adhered to a glass substrate).

LatB: Latrunculin B

LE: Lateral epidermis

MβCD: methyl-β-cyclodextrin

PFS: Perfect focus system

SD: Standard deviation

SDCM: Spinning disk confocal microscopy

SNR: Signal-to-noise ratio

Chapter 1 Introduction

Organisms must interpret and react to both the chemical makeup of their surroundings and the physical forces impacting them, even at the single-cellular level (Diz-Muñoz, Fletcher, and Weiner, 2013). These interaction requirements are fulfilled by numerous and interconnected systems of cellular machinery. One such system involves the eponymous protein clathrin, and the process of clathrin-mediated endocytosis (CME). While this system explicitly effects the chemical environment of the cell by internalizing material from the extracellular space, I will delineate the ways in which it is also impacted by the mechanical environment of the cell.

Clathrin is a triskelion-shaped protein formed out of three heavy chain subunits and attached to each of these along their length is a light chain subunit (Heuser et al., 1987; Fig.1.1). The legs of each triskelion bind to one another at such an angle that clathrin can polymerize into locally flat hexagons, or locally curved pentagons (Heuser, 1989; Fig.1.2). This assembly is referred to as a clathrin-coated structure (CCS). When sufficient pentagons aggregate, a spherical cage surrounds and shapes the plasma membrane into an invaginating "bud" (Fig.1.3). Additional proteins then aggregate to catalyze membrane scission, resulting in the internalization of membrane-bound proteins

Figure 1.1 Electron microscopy images of clathrin.

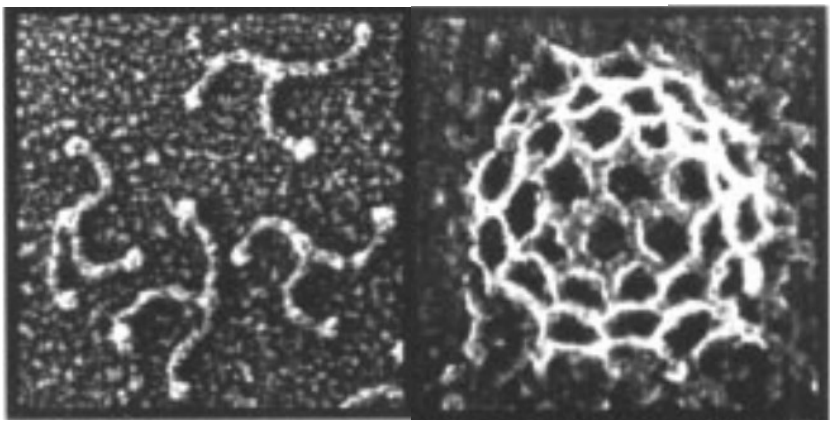

Individual clathrin triskelia captured using electron microscopy (left). An assembled, curved, clathrin-coated structure (right). This figure was adapted from Schmidt (1997) with images provided by John Heuser from Washington University in St. Louis.

(Koenig and Ikeda, 1989; Damke et al., 1994; Ferguson et al., 2007). The mechanism of membrane-curvature generation is still under much scientific debate and will be discussed in Chapter 5, but the eventual requirement of membrane curvature is well accepted.

1.1 Details of Clathrin Formation

Canonically, there are two distinct paths that the aggregation of membrane-bound clathrin can follow (Fig.1.2). First, clathrin may form flat structures of heterogeneous size and shape that can reach hundreds of nanometers in diameter (Saffarian et al., 2009; Grove et al., 2014). These objects are very long lasting, existing for minutes to hours and it is unclear what role these structures play in supporting cell function. Alternatively, there is the canonical clathrin-coated pit (CCP). As will be argued in Chapter 5, this structure forms via continuous invagination of the membrane, where curvature is steadily

Figure 1.2 Electron microscopy image of curved clathrin pits, and flat clathrin plaques.

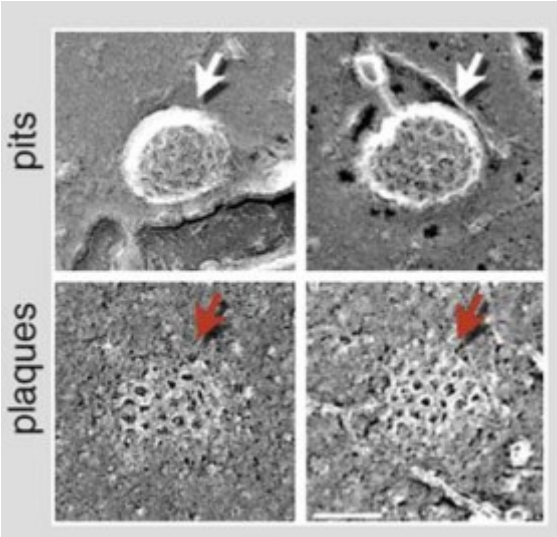

Figure from Kirchhausen, 2009

generated by the polymerization of clathrin and associated proteins. This is the structure, described previously, which ends with a spherical clathrin coat followed by membrane scission and vesicle internalization (Fig.1.3). The structure reaches ~100nm in diameter and the process requires ~1 minute for cells adhered to a glass substrate, but the time can vary based on the extracellular environment (Kural and Kirchhausen, 2012).

1.2 Data Acquisition

Fluorescence microscopy is the predominant observational technique to elucidate the dynamics of clathrin at the cell surface. Fluorescence is the light emitted by a molecule, in our case a protein, upon excitation via light of a greater energy. For our experiments, cells are seeded on a substrate, usually glass, through which light of a selected wavelength is passed that will excite the fluorescent proteins bound to the

Figure 1.3 Time course of clathrin-mediated endocytosis.

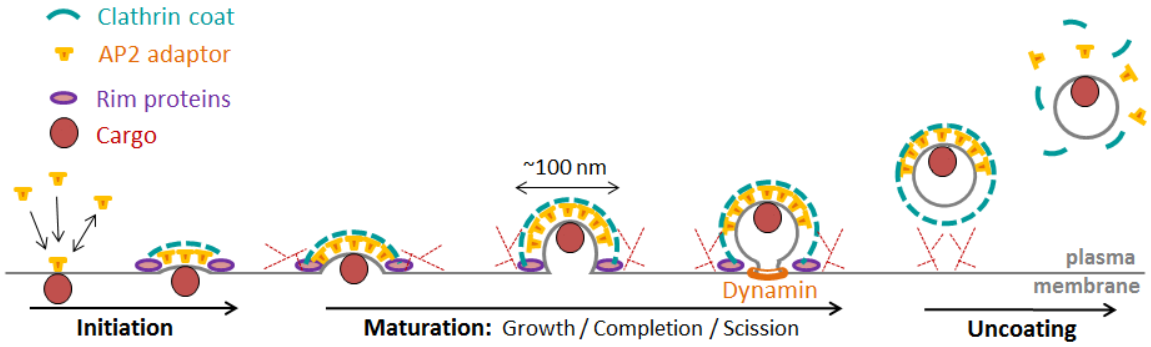

Clathrin-mediated endocytosis initiates with the recruitment of adapter protein 2 (AP2) to the site of membrane-bound cargo. Curvature is continually generated with the recruitment of clathrin until it is nearly spherical. Finally, dynamin is recruited to perform membrane scission allowing for vesicle internalization followed by coat dissociation.

protein of interest. We use fluorescent proteins because the cells can be engineered to produce them directly attached to a protein of interest. This is done via genetic modification by either altering the cells' original genome, or introducing a bacterial plasmid wherein the DNA for the fluorescent tag is adjacent to the protein of interest.

Clathrin participates in vesiculation on many different membranes within and surrounding the cell, but we are primarily interested in the mechanics of the exterior plasma membrane. Clathrin does not interface directly with the membrane. Instead, the interaction is mediated by a multitude of adaptor complexes. The AP2 adaptor complex functions exclusively on the exterior plasma membrane, so we study cells that have the σ2-subunit of the AP2 complex tagged with the enhanced green fluorescent protein (EGFP). We tag a single subunit because AP2 is made of an aggregation of different subunits, rather than being a complete protein in its own right, so only one subunit needs to be tagged to detect its location.

In our lab, the predominant imaging technique is a variant of fluorescence microscopy called spinning-disk confocal microscopy (SDCM, Fig.1.4). For this system, excitation light is focused with a microlens array, passed through a concentric pinhole array, and finally focused on the sample with an objective lens. To illuminate the entire sample, the microlens array rotates rapidly to sweep a corresponding array of focused beams across the field of view. The focus of the light only provides enough energy to illuminate a thin section of the sample in the direction parallel to the light path. Light emitted by the fluorescent proteins follows a return path similar to the excitation light. It is focused by the same objective lens through the same pinhole array, but before encountering the microlens array a beamsplitter alters its path toward a camera. The function of the pinhole is to reject out-of-focus light and generate an image exclusively of fluorescent proteins from the plane of interest. This system gives the researcher the ability to image a large volume in sequential steps parallel to the illumination path. We can use this system to image entire cells or even whole tissues.

However, we primarily capture images of all clathrin on the singular surface of the cell adhered to the substrate. The ability of SDCM to reject out of focus light is essential to achieving a high signal-to-noise ratio (SNR). Sequentially captured images act as inputs to a program that tracks each fluorescent spot (Auget et al., 2013). The spherical cages formed by clathrin are small enough (~100nm diameter) to appear as diffraction-limited spots on the camera. This means that despite a cage being composed of dozens of clathrin molecules it appears as a single spot on the camera. Details such as

Figure 1.4 Schematic of spinning disk confocal microscopy.

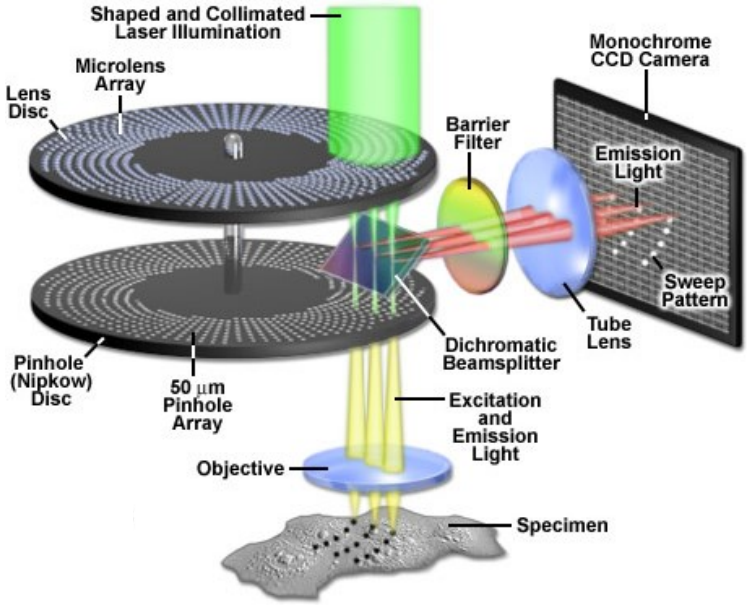

Laser light impinges upon the (spinning) microlens array from the top of the figure. This focusses the light through a dichromatic beamsplitter and a pinhole disk spinning in the same way as the microlens array. After leaving the pinhole array the light is focused by an objective lens on the specimen (which is usually plated on a glass substrate). The spinning of the disk results in light sweeping across the specimen. Fluorescence from the specimen is returned through the objective and the pinhole to be reflected by the dichromatic beamsplitter towards an additional filter and focused by a final lens onto a camera sensor. Figure from Toomre, Langhorst, and Davidson, n.d.

the intensity and position of each spot in each frame are recorded for analysis. The most common metric for describing the dynamics of CME is the lifetime of these spots (time from formation to extinction). However, Chapter 2 will introduce the methodology of growth rate analysis to study the dynamics of CME with greater spatial and temporal resolution than lifetime analysis.

1.3 Plasma Membrane Tension Effects on CME Dynamics

It is evident that CME would put the cell into chemical contact with its environment due to the internalization of extracellular material. However, the requirement of membrane curvature also links CME to the mechanical environment of the cell (Saleem et al., 2015). If the membrane is tense it will require more energy to form such extreme curvature, and if it is loose it will require less energy. These energy requirements manifest in the time it takes for the process to complete, which is why we study the dynamics of CME. In analyzing these dynamics, we hypothesize that one could also discern mechanical properties of the cell, particularly the tension of the membrane.

Most methods for measuring the tension of the membrane require active and precise alteration of the cell, e.g. through generation of membrane tethers (Fig.1.5). By measuring the force required to pull a thin strand of membrane from the cell body there is a simple way to calculate the tension on the membrane (Dai and Sheetz, 1999). However, this technique is only capable of measuring local tension values. A single measurement of membrane tension from a tether is insufficient to understand the behavior of the cell in a more complex environment. Additionally, it is impossible to generate a membrane tether from a cell in a fully enclosed, three dimensional environment, which is the case when performing measurements on a living organism.

To observe cellular forces on a larger scale, a researcher can observe the cell in an environment of known physical properties. These are often three-dimensional gel environments that simulate the mechanical properties of tissues, where cells from multi-

Figure 1.5 Membrane tethering.

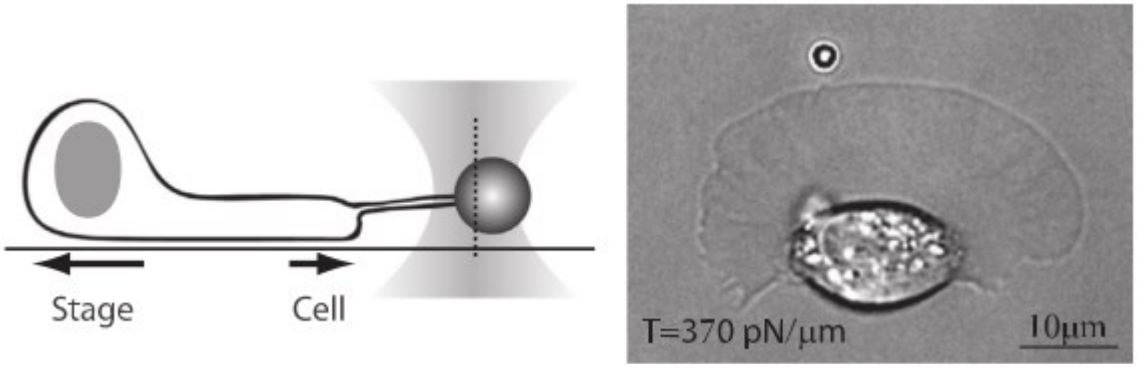

Schematic of a membrane tethering experiment (left). Example of a membrane tether being pulled from a live cell membrane (right). Figure from Lieber et al., 2015.

cellular organisms would naturally be found. These gels can be formed with fluorescent particles dispersed throughout and the forces applied to the environment may be inferred via the displacement of the particles. While very useful for observing large-scale forces, the optical bulk of the gel partially scatters both excitation and emitted light, which reduces the ability to resolve activity inside of the cell via fluorescence microscopy. In order to monitor CME dynamics accurately we must be able to observe intracellular fluorescence with the highest possible spatial and temporal resolution.

The ideal arrangement for cellular study is in the most evolutionarily natural environment, i.e. the original organism (referred to here as in vivo). However, this shares a similar hindrance as the aforementioned gels that the optical bulk of the organism greatly impedes the resolution power of fluorescence microscopy. So for high-resolution imaging we must rely on interesting cellular phenomena near the surface of the organism.

This dissertation will outline methods of experimentation and analysis to allow for in vivo measurement of CME dynamics, and ultimately relate this process to membrane tension. Chapter 2 will introduce the methodology of growth rate analysis, which allows for higher spatial and temporal resolution than lifetime analysis. Chapter 3 will outline the effects of membrane tension on the dynamics of CME. Chapter 4 will utilize measurements of CME dynamics to predict the distribution of tension in the membrane of individual cells and tissues in vivo. Chapter 5 will discuss the generation of curvature during the formation of clathrin-coated pits (CCPs), which is necessary for its role as an ongoing marker of tension. Finally, Chapter 6 will summarize the results in this dissertation and present future avenues of study in pursuit and in potential.

Chapter 2 Deciphering Dynamics of Clathrin-Mediated Endocytosis in a Living Organism

Derived from: Ferguson, J.P., Willy, N.M., Heidotting, S.P., Huber, S.D., Webber, M.J., and Kural, C. (2016). Deciphering dynamics of clathrin-mediated endocytosis in a living organism. J. Cell Biol. *214*, 347–358.

In this chapter my contributions are the development of growth rate analysis; some micropipette aspiration experiments; analysis of low and high pits and plaques; development of integrated movie segments; analysis and some experiments of cholesterol depleted cells; and analysis of amnioserosa data, including development of 3D tracking, segmentation into apical, basal, and blobs, growth rate analysis, and individual cell segmentation.

2.1 Abstract

Technical limitations inherent to detection and tracking of single fluorescent particles prevent the characterization of CME dynamics in vivo. Therefore, the effects of mechanical cues generated during the development of multicellular organisms on formation and dissolution of clathrin-coated structures (CCSs) have not been directly observed. Here, we use growth rates of fluorescence signals obtained from short CCS

intensity trace fragments to assess CME dynamics. This methodology does not rely on determining the complete lifespan of individual endocytic assemblies. Therefore, it allows for real-time monitoring of spatiotemporal changes in CME dynamics and is less prone to errors associated with particle detection and tracking. We validate the applicability of this approach to in vivo systems by demonstrating the reduction of CME dynamics during dorsal closure of Drosophila melanogaster embryos.

2.2 Introduction

Dynamics of endocytic pathways are inversely related to plasma membrane tension, because membrane internalization machinery are required to do work against the two major constituents of tension (i.e., in-plane tension and membrane-cytoskeleton adhesion) to create invaginations (Dai et al., 1997; Raucher and Sheetz, 1999; Sheetz, 2001; Apodaca, 2002; Gauthier et al., 2012; Diz-Muñoz et al., 2013). Tension regulates formation and curvature of clathrin coats reconstructed on giant unilamellar vesicles (Saleem et al., 2015). Studies in yeast and in polarized and mitotic mammalian cells show that CME is inhibited unless plasma membrane tension is counteracted by actin dynamics (Aghamohammadzadeh and Ayscough, 2009; Boulant et al., 2011; Kaur et al., 2014). Regulation of endocytic rates by mechanical cues has important roles in development; during the early stages of Drosophila melanogaster embryogenesis, increased tension inhibits Fog receptor endocytosis, which is required for completion of ventral furrow formation (Pouille et al., 2009).

Our current understanding of CME dynamics is based on in vitro imaging studies that are limited in their potential to mimic physical properties of tissue micro-environments. In a majority of these studies, dynamics of CCSs were monitored at the plasma membrane–coverglass interface, which has no physiological correspondence. Plating conditions, membrane–substrate interactions, and cell spreading area can regulate clathrin dynamics in in vitro experiments (Batchelder and Yarar, 2010; Tan et al., 2015). A holistic understanding of CME requires elucidating clathrin coat dynamics in cells residing within tissues of multicellular organisms.

Determining lifetime distributions of CCSs is the prevalent technique for monitoring CME dynamics. This approach necessitates identifying complete traces of individual CCSs (from initiation to dissolution), which is error prone within high-density particle fields and regimes with low signal to noise (Aguet et al., 2013; Mettlen and Danuser, 2014). CME dynamics have not been reported for any in vivo systems, because determining lifetimes of individual CCSs is more challenging within complex, 3D geometries of living tissues. In this chapter, we show that the rate of incorporation or dispersion of clathrin coat components during formation of endocytic vesicles can be used as reporters for clathrin dynamics. Because hundreds of clathrin-coated endocytic carriers can be detected within a cell at a given instant, distributions spanning the entire range of formation and disassembly rates can be obtained within temporal windows shorter than the lifetime of clathrin coats. This advantage makes growth rate distributions a superior alternative to clathrin lifetime analyses, especially within cellular contexts

where the fidelity of fluorescent particle tracking is low. Using this approach, we provide the first experimental evidence of CME mechanoregulation in tissues of live Drosophila embryos.

2.3 Results

2.3.1 CCS growth rates are robust reporters of CME dynamics

In fluorescence imaging assays, endocytic CCS formation is marked by appearance of a diffraction-limited spot that steadily increases in intensity because of accumulation of fluorescently tagged coat components. The internalization of the clathrin-coated vesicle is followed by a relatively fast dimming of the fluorescence caused by dissolution of the coat (Kural and Kirchhausen, 2012; Fig. 2.1, A and B). Lifetime is an extensively used metric for characterizing CME dynamics. Factors that elongate CCS lifetimes reduce the efficacy of ligand endocytosis (Cureton et al., 2010; Boulant et al., 2011). Any factor that affects the rate of formation and/or dissolution of clathrin coats is a potential regulator of CCS lifetimes and, hence, CME dynamics. To establish whether we can use growth rates of CCS signal as metrics for endocytic dynamics, we quantified formation and dissolution (negative growth) rates of individual CCSs by determining the slope of the normalized fluorescence intensity within 12-s temporal windows (Fig. 2.1 C). Because hundreds of CCS traces can be detected within a single cell at a given instant, we were able to assemble distributions of growth rates for each frame of time-lapse acquisitions. When applied to cells that produce predominantly clathrin-coated pits, the majority of the growth rates obtained in this way were positive (i.e., corresponding to increasing

Figure 2.1 Determining CCS growth rate distributions.

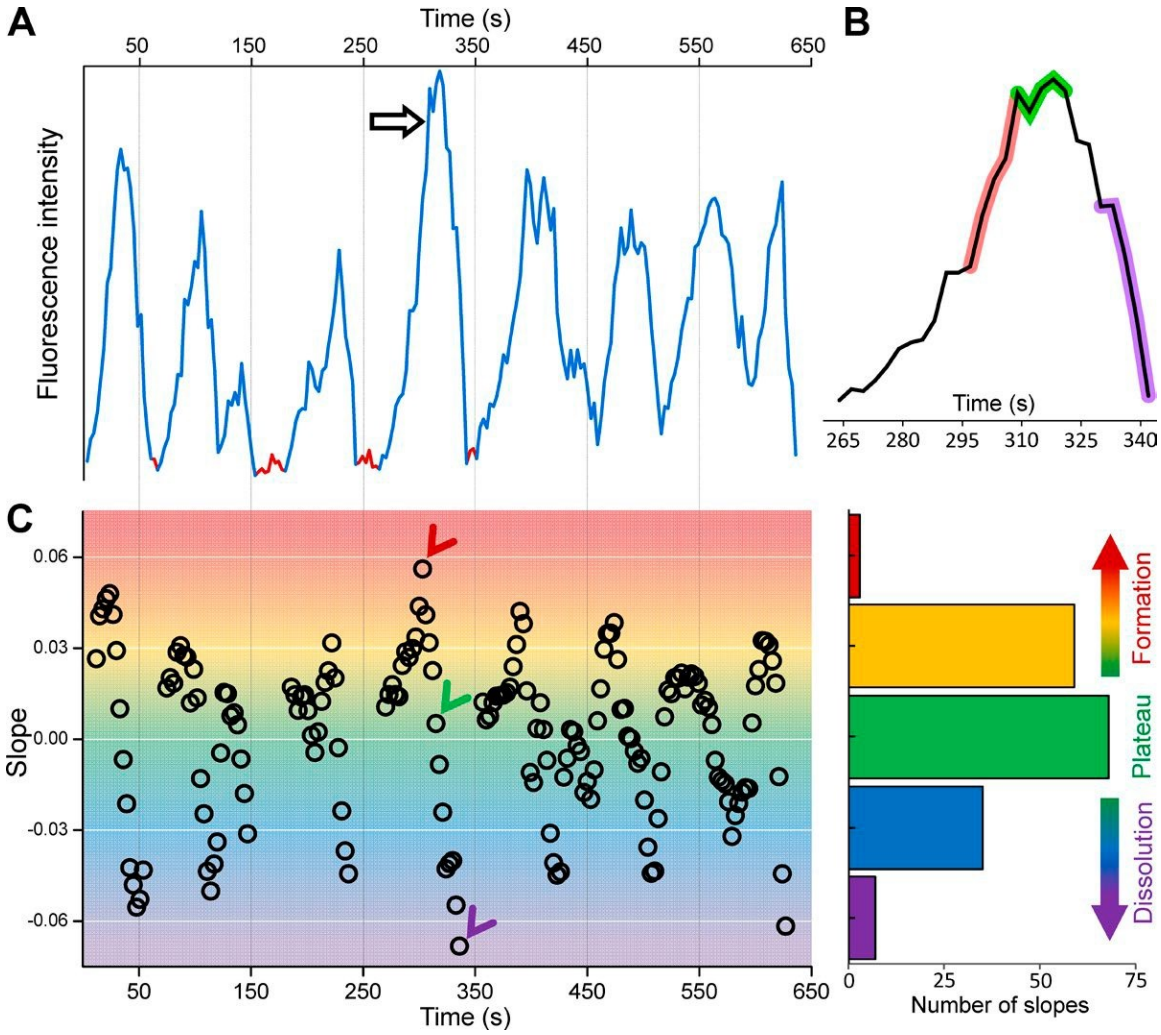

(A) Fluorescence intensity trace of a clathrin hotspot imaged at the ventral surface of a BSC-1 cell expressing AP2-GFP. Traces segments that are not used in growth rate calculation are shown in red, as they were considered the background signal. (B) Zoomed version of the clathrin-coated pit trace marked by the arrow in A. Shaded regions show 12-s-long fragments dwelling at formation (red), plateau (green), and dissolution (purple) phases of the pit. (C, left) For the intensity trace in A, slope values representing the growth rates are determined from 12-s-long fragments centered on each time point. Red, green, and purple arrowheads mark the slopes corresponding to the growth, plateau, and dissolution fragments highlighted in B, respectively. (C, right) Bar plot shows the distribution of the growth rates shown in the left panel. Positive and negative values correspond to formation and dissolution phases, respectively.

fluorescence signal; Fig. 2.2 B, blue lines). This is consistent with the characteristic

intensity profile of pits, which has a steady formation phase followed by a relatively abrupt dissolution (Ehrlich et al., 2004; Massol et al., 2006; Fig. 2.1 B).

As a means to alter CME efficiency, we used micropipette aspiration to increase in-plane membrane tension in cells (Houk et al., 2012). We detected a significant increase in CCS lifetimes when micropipette aspiration was applied (45.5 ± 27.1 s versus 80.1 ± 86.6 s, N_{cells}= 7, N_{traces}= 38,136; Fig. 2.2 A). Asymmetry of the growth rate distributions is abolished upon aspiration, and a greater fraction of intensity traces were associated with steady levels of fluorescence signal (i.e., the plateau phase). High-magnitude slopes, which represent fast formation and dissolution phases, are diminished with the increasing membrane tension (Fig. 2.2, B and C). These transformations in the growth rate distributions suggest that obstruction of both coat formation and dissolution is the prevalent factor behind elongation of the mean CCS lifetime under increased membrane tension. Nathan Willy used two independent visualization tools to validate these results. First, he created 2D histograms assembled by superposition of CCS intensity profiles that are synchronized at the beginning, middle, or end of traces (Fig. 2.2 D). Even though CCSs have a wide distribution of lifetimes, 2D histograms assembled from traces obtained before aspiration displayed the characteristic intensity profile of coated pits (Fig. 2.2 D, top row, middle column). However, the histograms assembled using aspirated cell traces were wider and displayed significant elongation in formation, plateau, and dissolution phases (Fig. 2.2 D, bottom row). In the second approach, he used a hierarchical clustering algorithm (see Section 2.3.4) to create groups of CCS traces that

Figure 2.2 Using growth rate histograms as reporters of clathrin dynamics.

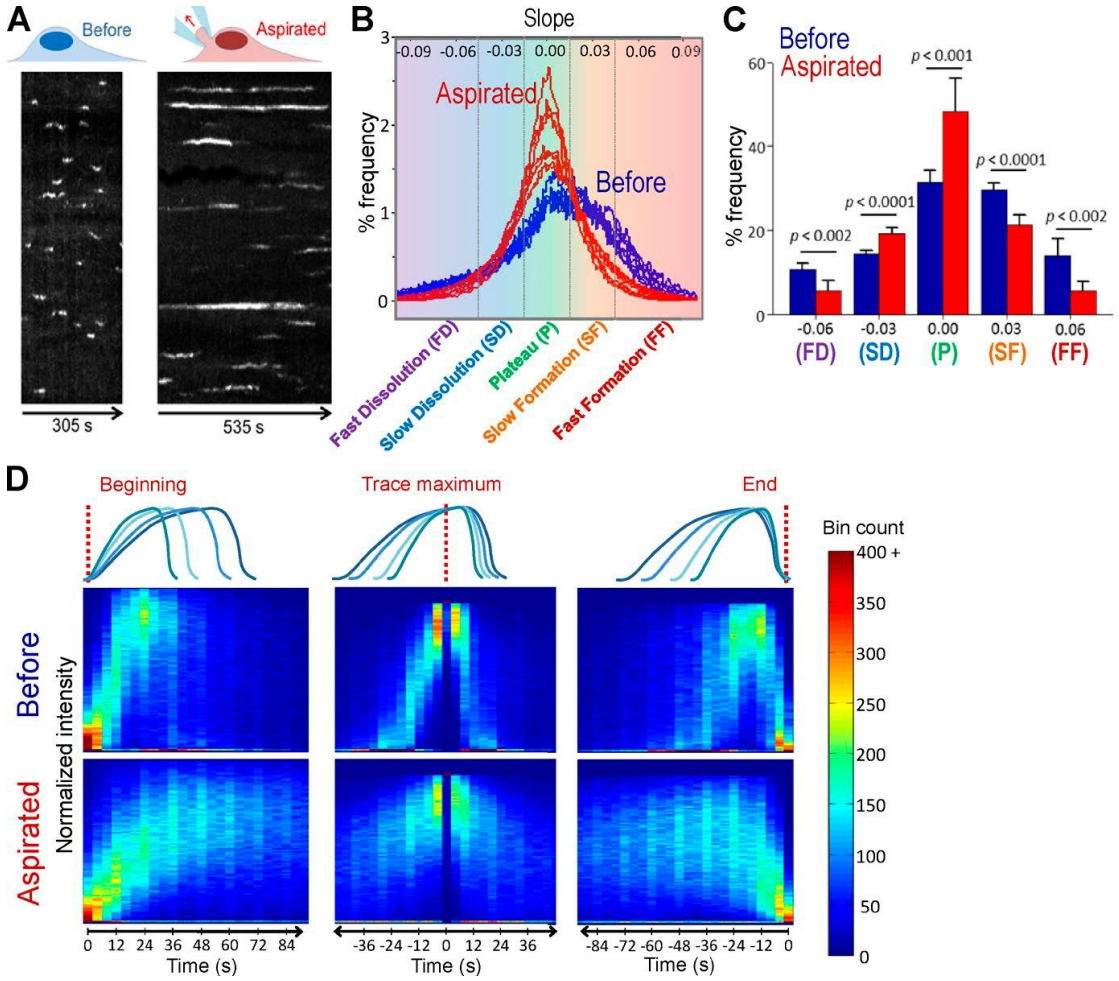

(A) Kymographs are generated from the same BSC-1 cell before and during microaspiration, respectively. Elongated AP2 traces demonstrate longer CCS lifetimes under increased membrane tension. (B) Growth rate distributions are shown for seven different cells before and during aspiration. Change in CCS dynamics induced by micropipette aspiration can be observed in growth rate distributions. In the control experiments (cells before aspiration), CCSs spend more time in the formation phase (i.e., the distribution is inclined toward positive slopes). The asymmetry was abolished upon aspiration and plateau phases got relatively longer (N_{cells}= 7 and N_{traces} = 38136). (C) Growth rate distributions in B are assembled in five bins to better delineate different phases of clathrin-coated vesicle formation (FD, fast dissolution; FF, fast formation; P, plateau; SD, slow dissolution; SF, slow formation). The bars show mean + standard deviation to illustrate dispersion between cells. P-values were obtained using the two-tailed t test. (D) 2D histograms of normalized intensity traces aligned at different time points (beginning, trace maximum, and end) and superposed as represented by the cartoons. In each alignment, the aspirated cells show a significantly widened distribution, demonstrating a preference for slopes lower in magnitude. Bins corresponding to multiples of 12s are more populated, as they contain trace data from both 3- and 4-s frame rate acquisitions.

have similar intensity profiles. As expected, clusters obtained from aspirated cells displayed longer plateau phases and slower formation and dissolution rates (Fig. 2.3).

To elucidate the effects of membrane–substrate interactions on CCS growth rates, we used a 3D particle tracking algorithm to determine the relative axial positions and fluorescence intensities of CCSs at the ventral surface of cultured cells (Kural et al., 2012, 2015). Along with pits, we observed formation of clathrin-coated plaques at the ventral surfaces of BSC-1 cells that are plated for >72 h (Fig. 2.4 A). Based on the intensity and position information, we categorized the CCSs as plaques (bright and close to substrate), "low" pits (dim and close to substrate), and "high" pits (dim and far from the substrate; Fig. 2.4, B and C). In good agreement with the previous studies, we found that CCSs positioned closer to the substrate contact sites are significantly longer lived (plaques, 174.5 ± 160.5 s; low pits, 75.2 ± 78.3 s; high pits, 48.3 ± 27.8 s, N_{cells} = 6, N_{traces}= 11,482; Fig. 2.4 C; Batchelder and Yarar, 2010). Growth rate analyses establish that impairment of clathrin dynamics in the proximity of adhesion regions is associated with extension of the plateau and diminishing of the high slope phases, consistent with the measurements performed in aspirated cells (Fig. 2.4 D). Our combined results demonstrate significant alterations in CCS growth rates caused by physical factors that hinder endocytic dynamics.

Figure 2.3 Hierarchical clustering of CCS traces.

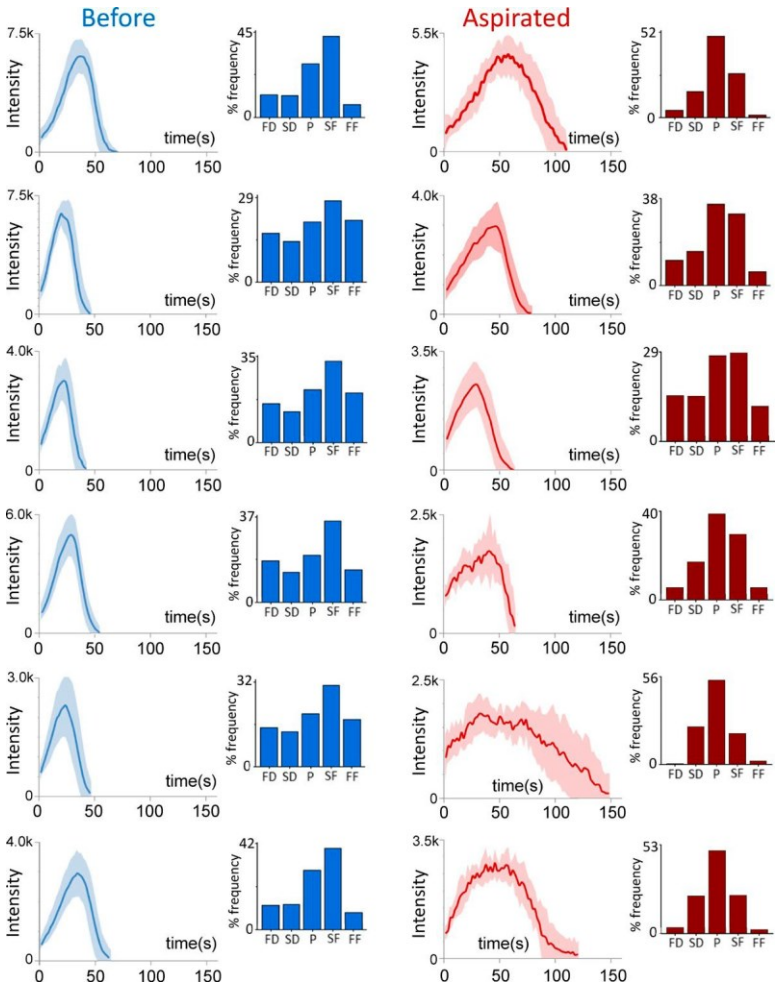

CCS trace clusters emerging before (blue) and during (red) micropipette aspiration are shown as mean ± standard deviation (shaded area). Growth rate histograms obtained using the traces in each cluster are shown next to the intensity profiles. FD, fast dissolution; FF, fast formation; P, plateau; SD, slow dissolution; SF, slow formation.

Figure 2.4 CCSs in proximity of substrate adhesion sites have reduced dynamics.

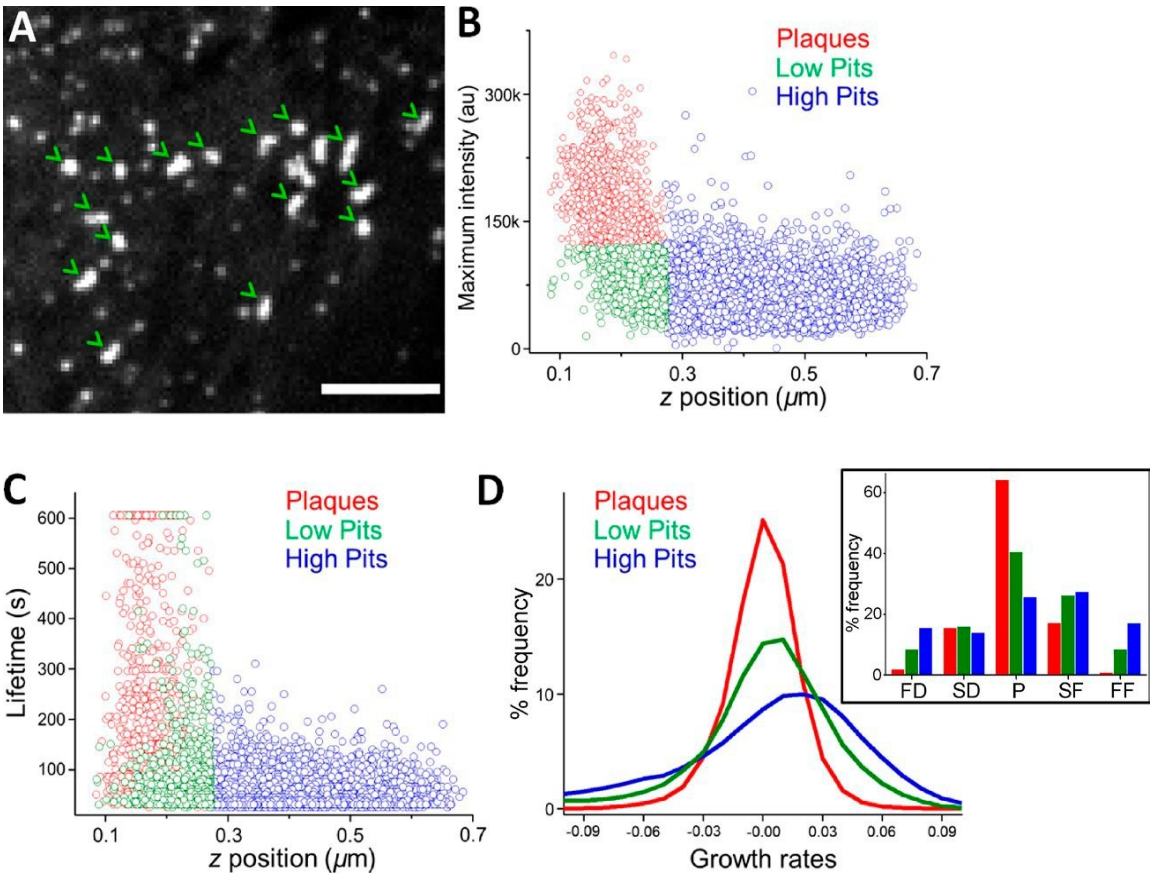

(A) Arrowheads mark clathrin-coated plaques at the ventral surface of a BSC-1 cell stably expressing AP2-GFP. Bar, 5 μm. Scatterplot shows maximum intensity versus the axial positions of CCSs detected at the ventral surface. The positions are relative to the lower bound of the confocal volume used for 3D tracking (Kural et al., 2012). CCS traces are divided into plaque (red) and pit (green and blue) populations based on their maximum intensities. Clathrin pits positioned closer to the substrate are in green (N_{cells} = 6 and N_{traces} = 11,482). Scatterplot shows the lifetime versus axial positions of the CCSs shown in B. (D) Growth rate distributions of the pit and plaque populations. The inset shows the distributions as bar plots.

2.3.2 Accuracy of growth rate distributions does not depend on determining complete traces of CCSs

Errors associated with particle detection and tracking result in significant underestimation of CCS lifetimes (Aguet et al., 2013; Mettlen and Danuser, 2014). Slope values populating the growth rate histograms, however, are calculated using trace information within 12-s-long windows and thus do not rely on determining the complete CCS traces. We tested the reproducibility of growth rate distributions on 24-s-long integrated movie segments (IMSs) that are the quadrature sum of four different temporal sections of a movie (Fig. 2.5, A–C). Faithful assessment of CCS lifetimes from IMSs is impractical because (1) density of CCSs is on average four times greater than the original acquisition, (2) background noise level is increased due to error propagation, and (3) IMSs are significantly shorter than the mean coated pit lifetime (24 s versus 1 min). Despite these impediments, we found that CCS growth rate distributions could be reproduced very accurately from the IMSs (Fig. 2.5, B and C). We also found that distortion of the growth rate distributions caused by increased tension could be observed in the IMSs of microaspirated cells regardless of the algorithm used for tracking CCSs (Fig. 2.5 D).

Figure 2.5 Growth rate analysis does not depend on determining the complete traces of CCSs.

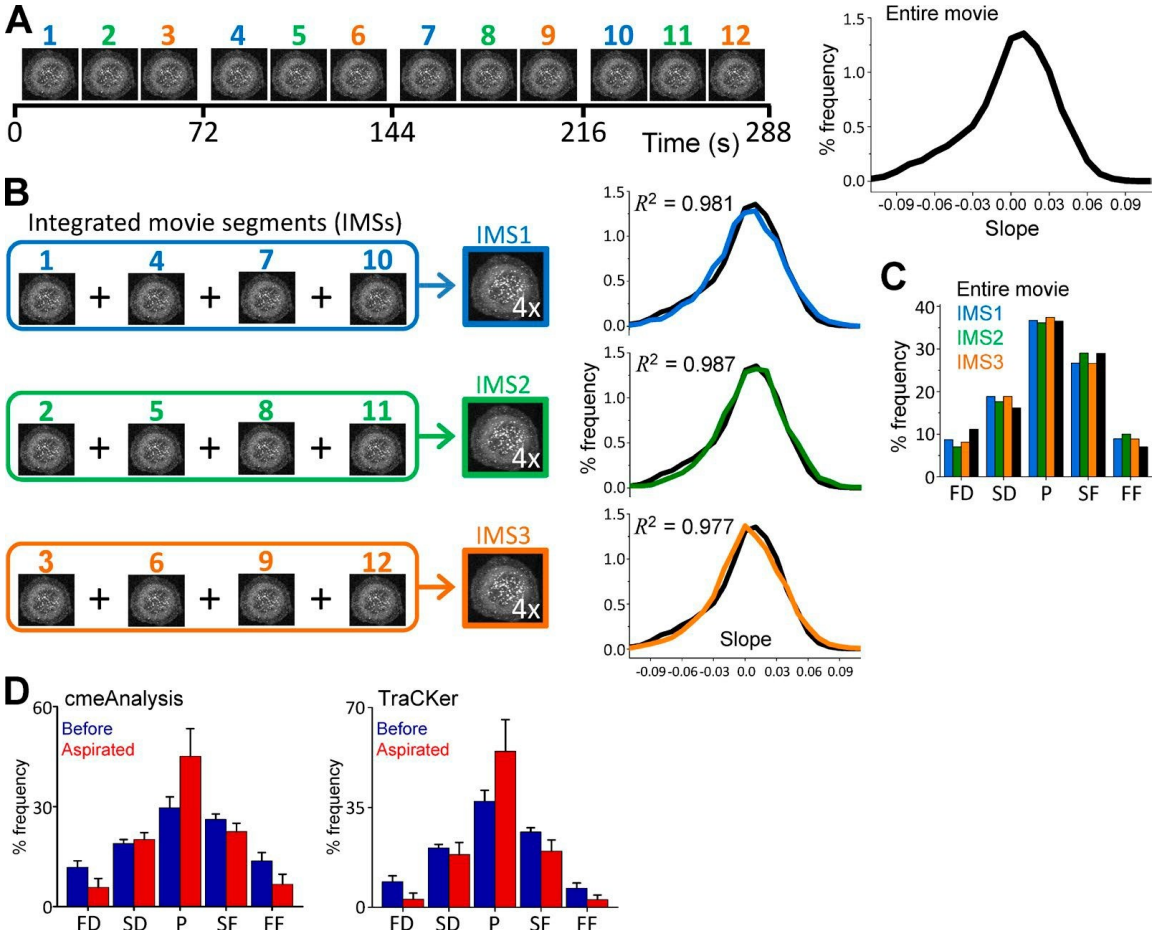

(A, left) Thumbnails represent 12 temporal sections (24 s each) of a 288-s-long fluorescence movie of a BSC-1 cell stably expressing AP2-GFP. (right) CCS growth rate distribution of the entire movie. (B, left) Integrated movie segments (IMSs) are the quadrature sum of four 24-s-long segments in which density of CCSs is approximately four times larger than the original movie. Temporal separation is maximized between the segments to minimize the number of self-overlapping clathrin spots. (right) Growth rate distributions obtained from each IMS is plotted in comparison with the distribution obtained from the entire movie (black). (C) Growth rate distributions of the IMSs and the entire movie are displayed as bar plots. (D) We tested the reproducibility of growth rate distributions using the CCS traces produced by cmeAnalysis (Aguet et al., 2013) and TraCKer (homemade particle tracking program). Changes in slope distributions upon micropipette aspiration can be observed in both datasets. Numbers of the analyzed IMSs are 25 and 64 for before and during aspiration conditions, respectively (N_{cells} = 7). Error bars show standard deviations. FD, fast dissolution; FF, fast formation; P, plateau; SD, slow dissolution; SF, slow formation.

2.3.3 Spatiotemporal variations in CME dynamics can be resolved in real time using CCS growth rates

When CCS lifetime distributions are used as metrics for CME efficiency, the mean lifetime of clathrin-coated pits (∼1 min) sets the limit of the temporal resolution for distinguishing the changes in clathrin coat dynamics. Consequently, the factors that influence endocytic processes at shorter time scales become indiscernible. Growth rate distributions, however, are constructed before the completion of traces and thus enable real-time monitoring of CCS dynamics in cells. We used growth rate analysis to monitor gradual changes in CCS dynamics upon acute cholesterol depletion. Structural studies show that cholesterol depletion reduces CME efficiency by replacing clathrin-coated pits with flat clathrin arrays (plaques) at the cell membrane (Subtil et al., 1999; Fig. 2.6 A). When cells are treated with methyl-β-cyclodextrin (MβCD), in line with our micropipette aspiration experiments, we found that impairment of CCS dynamics is coupled with disappearance of high-magnitude slopes in CCS growth rate distributions (Fig. 2.7, A and B). This result was anticipated, as cholesterol depletion increases the effective membrane tension through escalation of membrane–cytoskeleton adhesion energy (Khatibzadeh et al., 2012; Fig. 2.6 B). We used standard deviation of regional CCS growth rates to generate a visualization tool for monitoring spatiotemporal changes in clathrin dynamics in real time (Fig. 2.7 C). In regions with impeded CCS dynamics, standard deviations of the growth rates were reduced because of the disappearance of the high-magnitude slopes (Fig. 2.7 D). Using this approach, we found that MβCD treatment can affect CME

Figure 2.6 CCS dynamics in cholesterol-depleted cells.

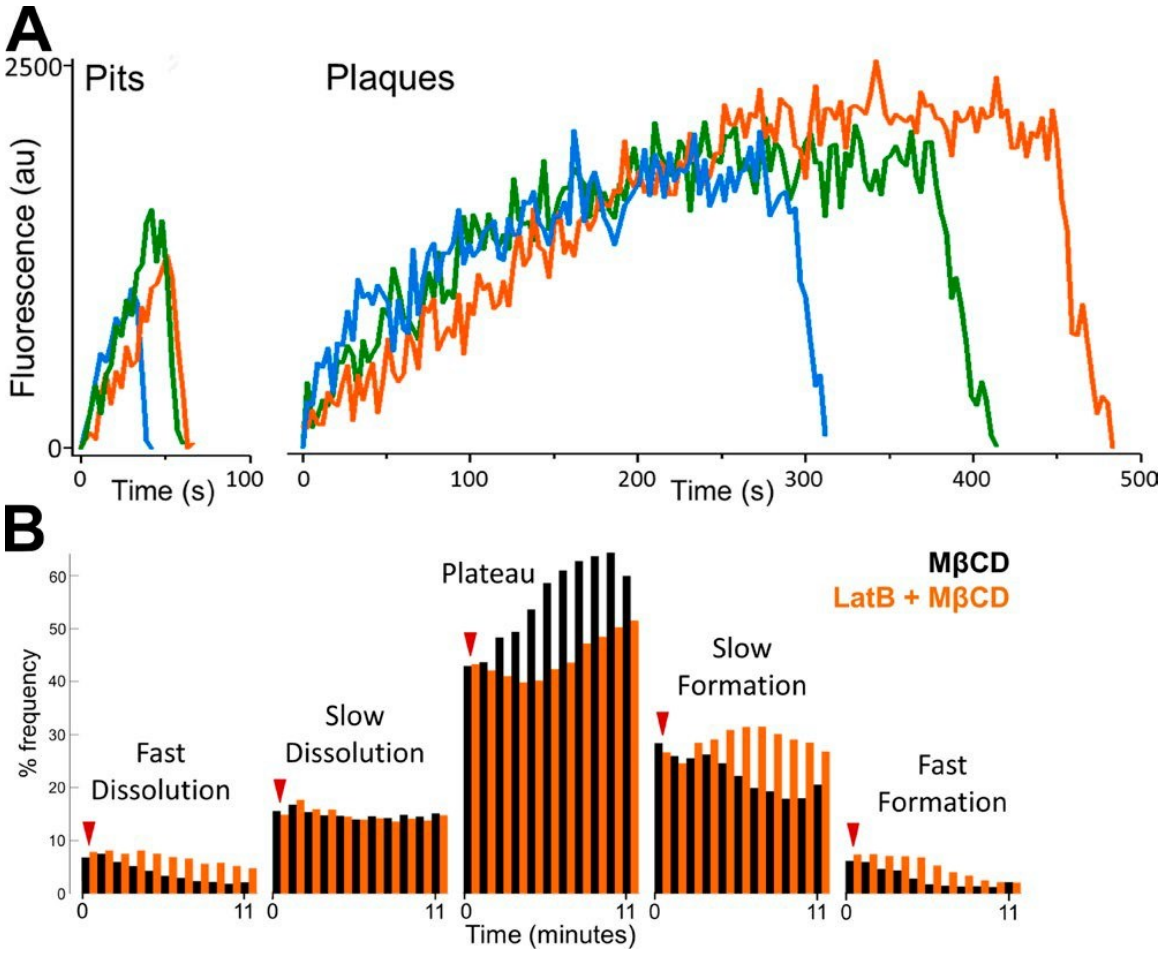

(A) Example intensity traces of clathrin-coated pits and plaques detected in a BSC1 cell before and after cholesterol depletion by MβCD treatment, respectively. (B) Percentage frequencies of the five growth phases are plotted as a function of time after addition of MβCD (4 mM final concentration; marked by the red arrowheads). Each bar in the histograms represents the frequency of CCS growth rates obtained from 1-min-long temporal windows. For each minute, growth rate histograms are calculated from a pool of CCS traces assembled from multiple cells (MβCD only: $N_{cells} = 6$ and $N_{traces} = 23{,}667$; latrunculin B [LatB] + MβCD: $N_{cells} = 4$ and $N_{traces} = 37{,}911$). Inhibition of CCS dynamics is less effective within cells that are pretreated with latrunculin B (2 μM final concentration; orange bars) 5 min before MβCD. Latrunculin B antagonizes the effect of MβCD by reducing the membrane–cytoskeleton adhesion energy (Hochmuth et al., 1996; Marcus and Hochmuth, 2002).

Figure 2.7 Real-time monitoring of CCS dynamics in cholesterol-depleted cells.

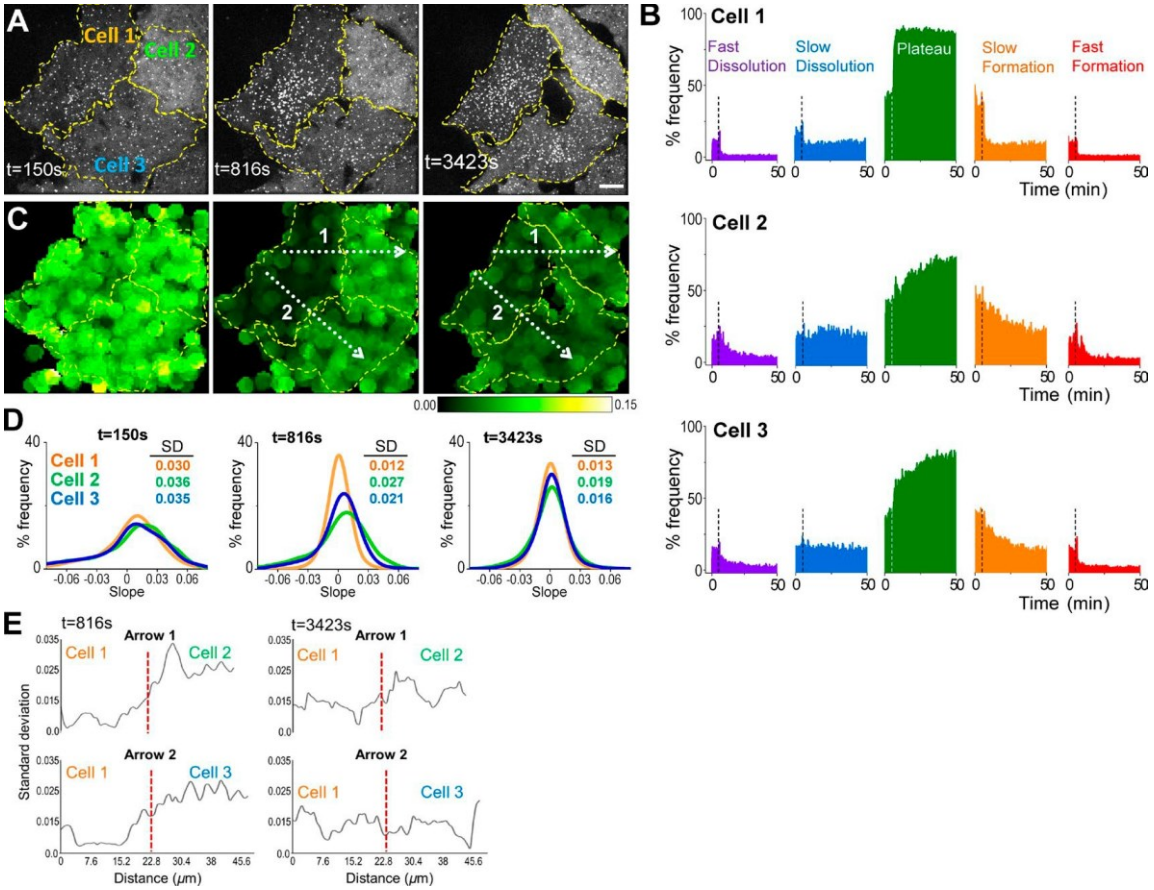

(A) Fluorescence images show snapshots of three BSC-1 cells stably expressing AP2-GFP. 10 mM MβCD was applied at the sixth minute (t = 360 s) to initiate cholesterol depletion. Dashed lines demarcate the cell boundaries. Bar, 10 μm. (B) For the three cells shown in A, percentage frequency of the five growth phases are plotted as a function of time. The dashed lines denote the time point of MβCD addition. The fastest change in CCS dynamics is observed in cell 1. (C) Figures show standard deviation (of local clathrin growth rates for the snapshots shown in A. Each pixel in the image is given the value of standard deviation of the growth rates detected from CCSs found in a radius of 4.8 μm. This representation is used for illustrating temporal and spatial variations in CCS dynamics. Standard deviation is lower in regions where the growth rate distribution is narrow, a signature of impeded CCS dynamics. Cell 1 responds to cholesterol depletion the earliest, as observed at t = 816 s. (D) Growth rate histograms are shown for the three cells at the time points of the snapshots in A and C. Spatial and temporal heterogeneity of CCS dynamics can be detected using the standard deviation of growth rate histograms, which change at different rates for the three cells. (E) Plots show spatial variation in standard deviation of local CCS growth rates over the distances shown by the dashed arrows in C. Positions of the cell boundaries are marked by the dashed red lines.

dynamics at different rates in neighboring cells (Fig. 2.7 D, E). Cell-to-cell variation may

stem from cells' mitotic state or position with respect to cell islet edges, as described earlier (Snijder et al., 2009).

Reduction in CCS formation rates (positive slopes) upon cholesterol depletion could be attributed to depletion of free clathrin coat components in the cytosol caused by increased CCS lifetime, as they are contained within existing coats. In that case, we would expect dissolution rates to disappear the earliest. However, we found that both positive and negative slopes (i.e., fast formation and dissolution phases) diminish simultaneously (Fig. 2.7 B), which indicates that flat clathrin arrays have slower formation rates than clathrin-coated pits (Fig. 2.6 A). Therefore, at variance with earlier interpretations (Subtil et al., 1999), our results indicate that flat clathrin arrays found in cholesterol-depleted cells cannot be considered as direct precursors of clathrin-coated pits, as they have distinct formation dynamics.

2.3.4 CCS intensity profiles can be reproduced from growth rate distributions

Note: Most work on hierarchical clustering and the cluster library was done by Nathan Willy.

Hierarchical clustering of CCS traces allows us to determine growth rate distributions corresponding to different intensity profiles (Fig. 2.8 A). An interesting question that arises is whether we can reverse the flow of information in this process (i.e., reproduce the mean intensity profiles using growth rate distributions). Our IMS analyses show that growth rate distributions can be accurately assembled even in the absence of complete CCS intensity profiles (Fig. 2.8 B). Therefore, whatever the design, such a

Figure 2.8 A novel analytical toolbox for CME dynamics.

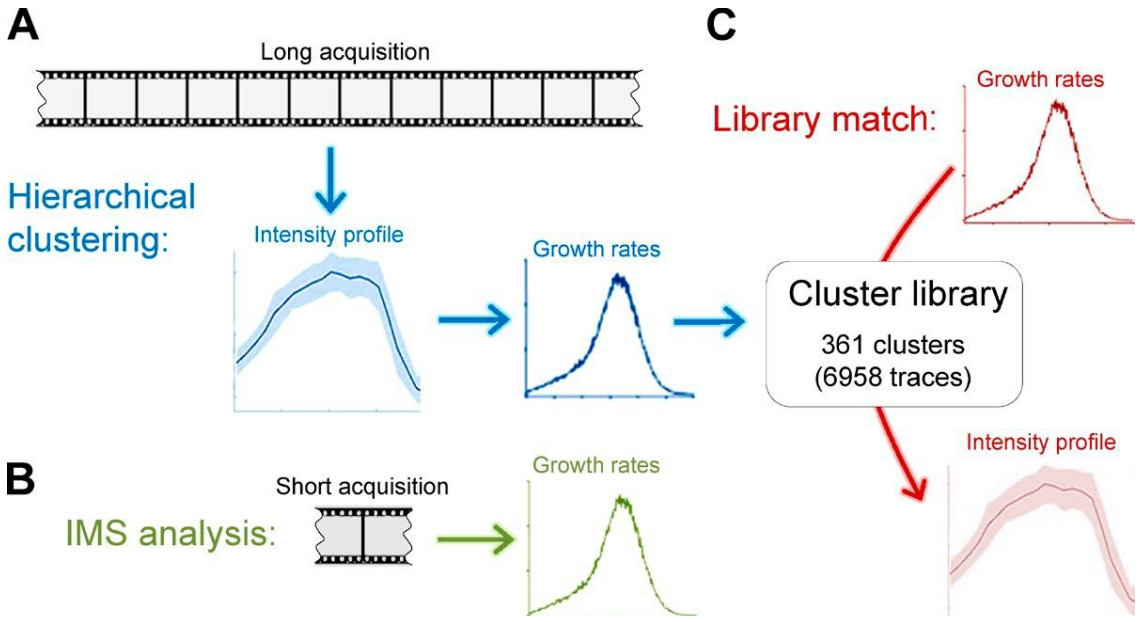

(A) CCS traces with similar intensity profiles can be grouped using a hierarchical clustering algorithm. This is applicable to acquisitions longer than the mean CCS lifetime. Growth rate distributions obtained from different clusters are used to develop a cluster library. (B) As validated by IMS analysis, growth rate distributions can be assembled using short fragments of CCS traces. (C) For a given growth rate distribution, an accurate estimation of the corresponding intensity profile is possible by determining analogous growth rate distributions in the cluster library.

methodology would be immensely useful for interpreting the CCS growth rates that are obtained from acquisitions in which monitoring complete CCS traces is infeasible. We used a strategy based on determining the analogous growth rate distributions within a library of CCS clusters (Fig. 2.8 C). We assembled a library of growth rate histograms that are obtained from 361 clusters containing a total count of 6,958 CCS traces. When we used test clusters obtained from various cellular contexts, we were able to make accurate predictions of their intensity profiles solely by determining the most analogous growth rate distribution within the cluster library (Fig. 2.9 A). When applied to cells coexpressing fluorescently tagged AP2 and clathrin, we found that the AP2 growth rate

Figure 2.9 Determining CCS intensity profiles using growth rate distributions.

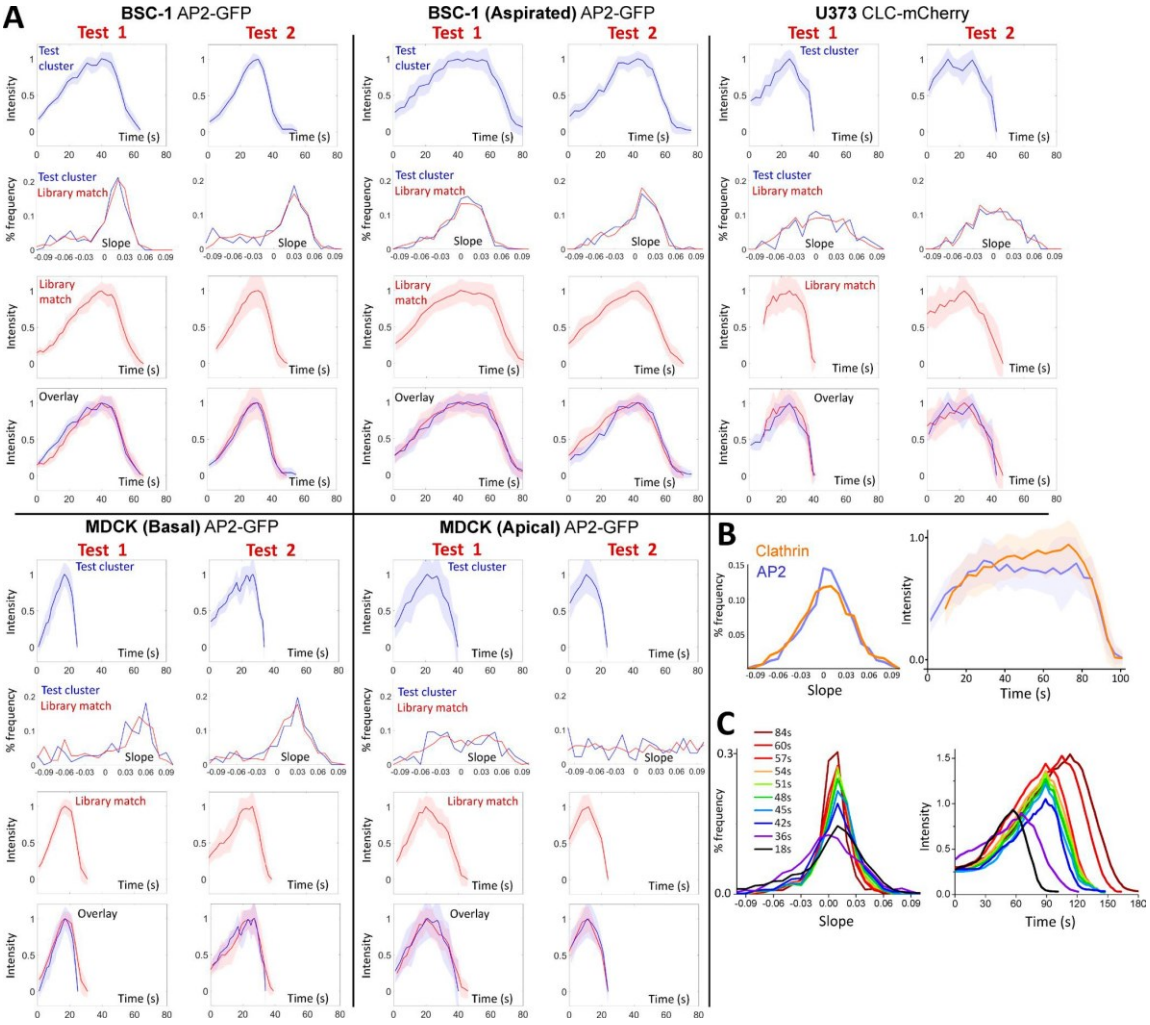

(A) Trace clusters from test cells (excluded from the library) are matched with clusters from the CCS library by their growth rate histograms. Successful reproductions of the cluster traces occurred in multiple cell types and conditions. Two clusters and library matches are shown per condition. Intensity profiles of test clusters and corresponding growth rate distributions are shown in blue, and library matches are in red. Shaded regions in intensity profiles mark the standard deviation of the cluster. (B) In a U373 cell coexpressing fluorescently tagged AP2 and clathrin, the growth rate of AP2 is more peaked at low slope magnitudes (left). Corresponding library matches show continuing increase in clathrin signal after AP2 signal plateaued (right). (C) MβCD is added to BSC1 cells at t = 0. Growth rate distributions determined at different time points of the treatment are shown on the left. (right) Predicted intensity profiles for the given growth rate distributions. Gradual changes in growth rates result in increasing trace lifetime and peak intensity.

distribution has higher frequencies at the low-magnitude slope region, and its predicted

intensity profile has a longer plateau before dissolution (Fig. 2.9 B). This result is in accord with the previous studies, which show that AP2 fluorescence growth halts earlier than the clathrin signal during the completion of the coat (Saffarian and Kirchhausen, 2008). When cells are treated with MβCD, incremental changes in mean CCS intensity profiles taking place within short intervals could be resolved in real time (Fig. 2.9 C). Upon cholesterol depletion, intensity profiles predicted using growth rate distributions became longer lived and reached higher maximum intensities in time. This was expected, as clathrin-coated pits are gradually replaced by larger and less dynamic CCSs in these cells (Fig. 2.6 A). Although the extent of the cluster library is a critical determinant of the fidelity of predicted intensity profiles, the presented strategy is a powerful tool for analyzing the changes in CCS growth rates obtained from in vivo datasets.

2.3.5 CME dynamics slow down during dorsal closure of Drosophila embryos

Note: The care and imaging of Drosophila was done by Spencer Heidotting.

Taking advantage of the new set of analytical tools at hand, we investigated the dynamics of CME in amnioserosa tissue of developing Drosophila embryos. Amnioserosa consists of a single layer of polarized cells that covers the dorsal surface of the embryo after germ band retraction. The tissue is entirely curtained by lateral epidermal cells in ~4 h by a process called dorsal closure (Jacinto et al., 2002). CCSs originating at the apical and basal surfaces of the amnioserosa can be detected in embryos expressing clathrin light chain (CLC) fused with GFP, using spinning disk confocal

Figure 2.10 3D tracking of CCSs in apical and basal surfaces of Drosophila amnioserosa.

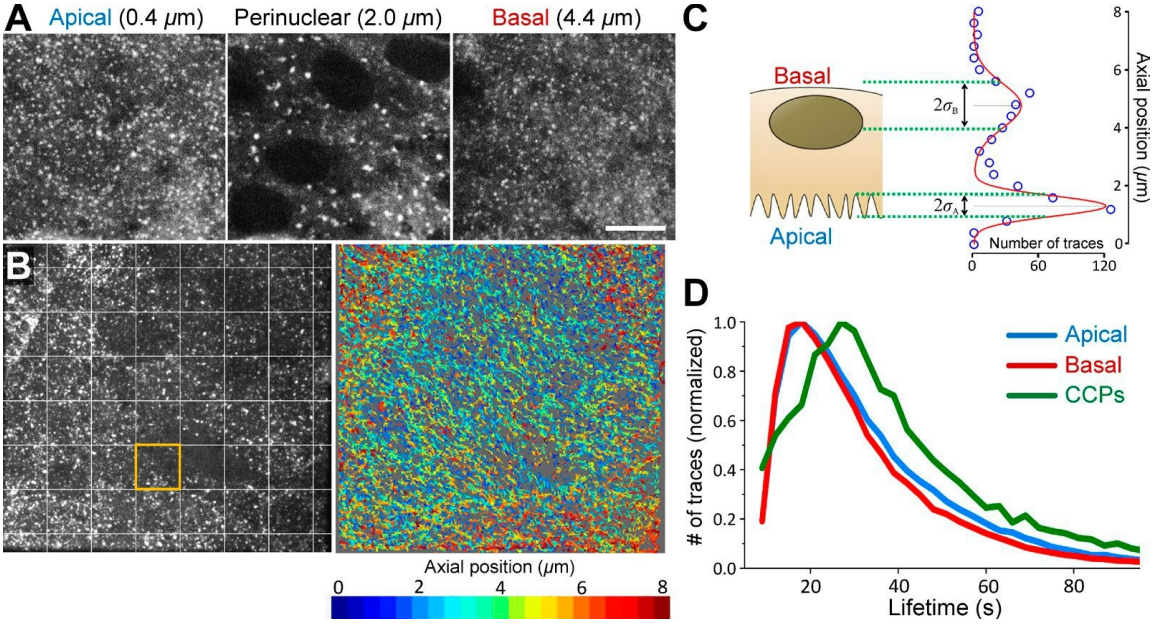

(A) Three sections of a confocal z-stack show apical, perinuclear, and basal regions of Drosophila amnioserosa cells expressing clathrin light chain fused with GFP (CLC-GFP). CCSs originating on organelles are observed mostly at the perinuclear regions as non-diffraction-limited bright fluorescent puncta (blobs). Bar, 10 μm. (B, left) Maximum projection image of a z-stack acquired at the amnioserosa tissue of a live Drosophila embryo. The image is divided into windows of 10 × 10 μm for determination of basal and apical surfaces (expanded in C). (right) Snapshot of CCS traces that are detected within the left panel, color-coded according to their axial positions. The projection of the entire 3D time-lapse acquisition and the corresponding CCS traces are shown in. (C) In each frame of the 3D time-lapse acquisition, axial positions of the apical and basal surfaces are determined separately for the 10 × 10 μm windows. Cartoon represents an amnioserosa cell oriented in a way that its apical surface faces the detection optics. The adjacent histogram shows the distribution of traces detected within the orange square shown in B with respect to their axial positions. The distribution is bimodal because of increased CCS density at the apical and basal surfaces and can be fit with a sum of two Gaussians. CCSs falling within one standard deviation of the respective means (± σ) are considered apical or basal. (D) A comparison of CCS lifetime distributions obtained from apical and basal amnioserosa with clathrin-coated pits (CCPs) detected in cultured BSC-1 cells stably expressing AP2-GFP (Amnioserosa: $N_{embryos}$ = 2, N_{cells} = 75, and N_{traces} = 124,013; CCPs: N_{cells} = 3 and N_{traces} = 12,002).

fluorescence imaging (Fig. 2.10 A). CCSs forming on intracellular organelles appear as bright blobs at the perinuclear regions. To determine individual CCS traces at the aminoserosa, we used a robust 2D particle tracking software (Aguet et al., 2013) and processed the output data using a trace combination algorithm to correct for particle

disappearances caused by movements in the axial dimension (Fig. 2.10 B; Appendix B). We used local distributions of the number of CCS traces to determine the axial positions of apical and basal surfaces (Fig. 2.10 C). We found that lifetime distributions for both of the surfaces are dominated by short CCS traces in comparison with the distributions obtained for clathrin-coated pits originating in cultured cells (Fig. 2.10 D). We believe the anomaly in lifetime distributions obtained from the amnioserosa has no biological basis but is a consequence of single-particle tracking errors caused by high CCS motility in this tissue and increased ratio of incomplete trace fragments (Fig. 2.11). When we used CCS growth rates as the alternative approach, we noted rapid changes in the distributions obtained from individual amnioserosa cells. However, we found no correlation between the temporal evolution of the distributions at the apical and basal surfaces (Fig. 2.12, A and B). We extended the duration of the imaging assays by acquiring CCS growth rates from 30-s-long acquisitions that are separated by temporal gaps of 3 or 10 min (Fig. 2.12 C). In this experimental scheme, monitoring CCS dynamics of individual cells throughout the entire assay was not achievable because the cellular organization of amnioserosa is not preserved over long durations, as the tissue is gradually replaced by lateral epidermis. When the growth rates are calculated for the entire tissue, we found that the intensity traces predicted using CCS growth rates were significantly longer lived than typical clathrin-coated pits (Fig. 2.12 E), in striking contrast with the results of the lifetime distributions (Fig. 2.10 D). In all of the four embryos we have analyzed in this way, we recorded significant change in growth rate distributions at the apical surface,

Figure 2.11. CCS motility in cultured cells and Drosophila embryos.

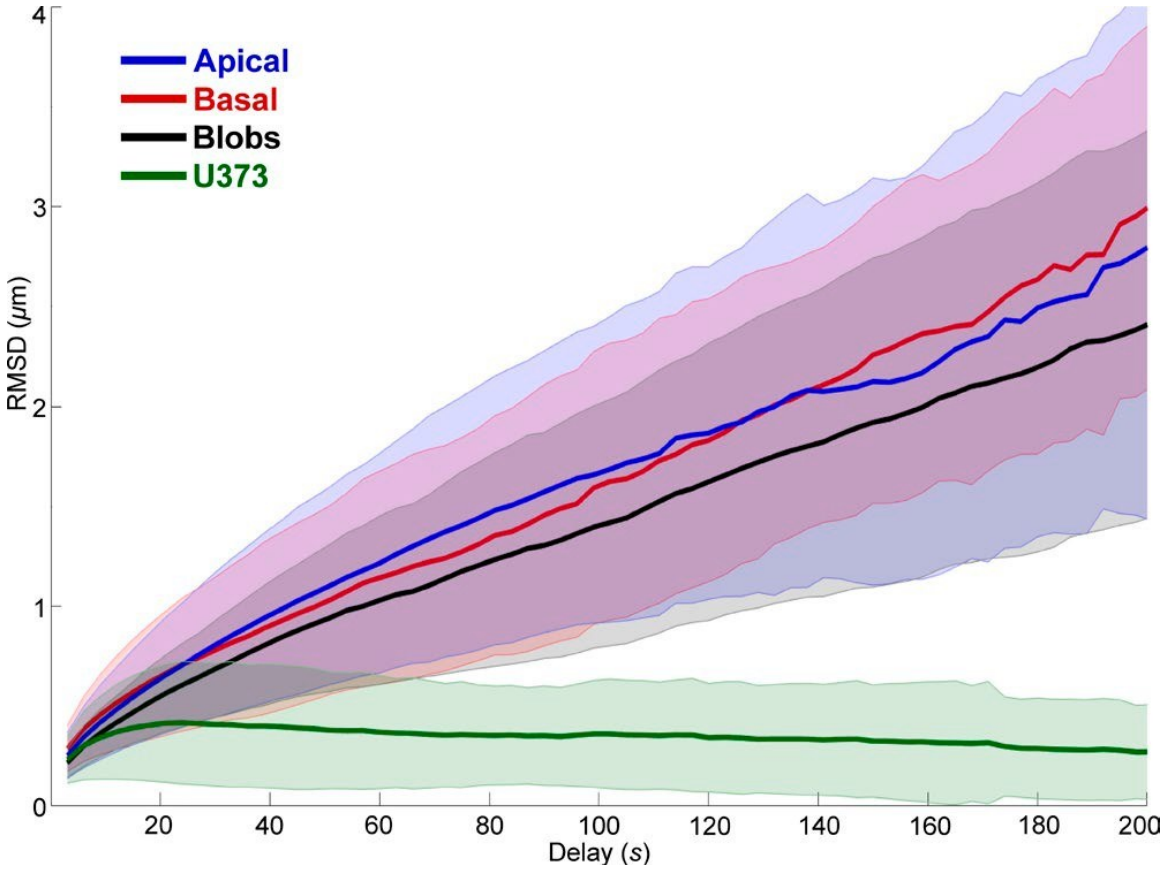

Root mean square displacements (mean ± standard deviation) are measured at different lag times for CCS traces detected in Drosophila amnioserosa cells (N_{apical} = 16,279, N_{basal} = 8,714, and N_{blobs} = 1,407) and U373 cells transiently expressing CLC-mCherry (N_{cells} = 4 and N_{traces} = 23,630).

which correspond to slower CCS dynamics and elongated lifetimes over time (Fig. 2.12, D–F).

Figure 2.12 CME dynamics in Drosophila amnioserosa.

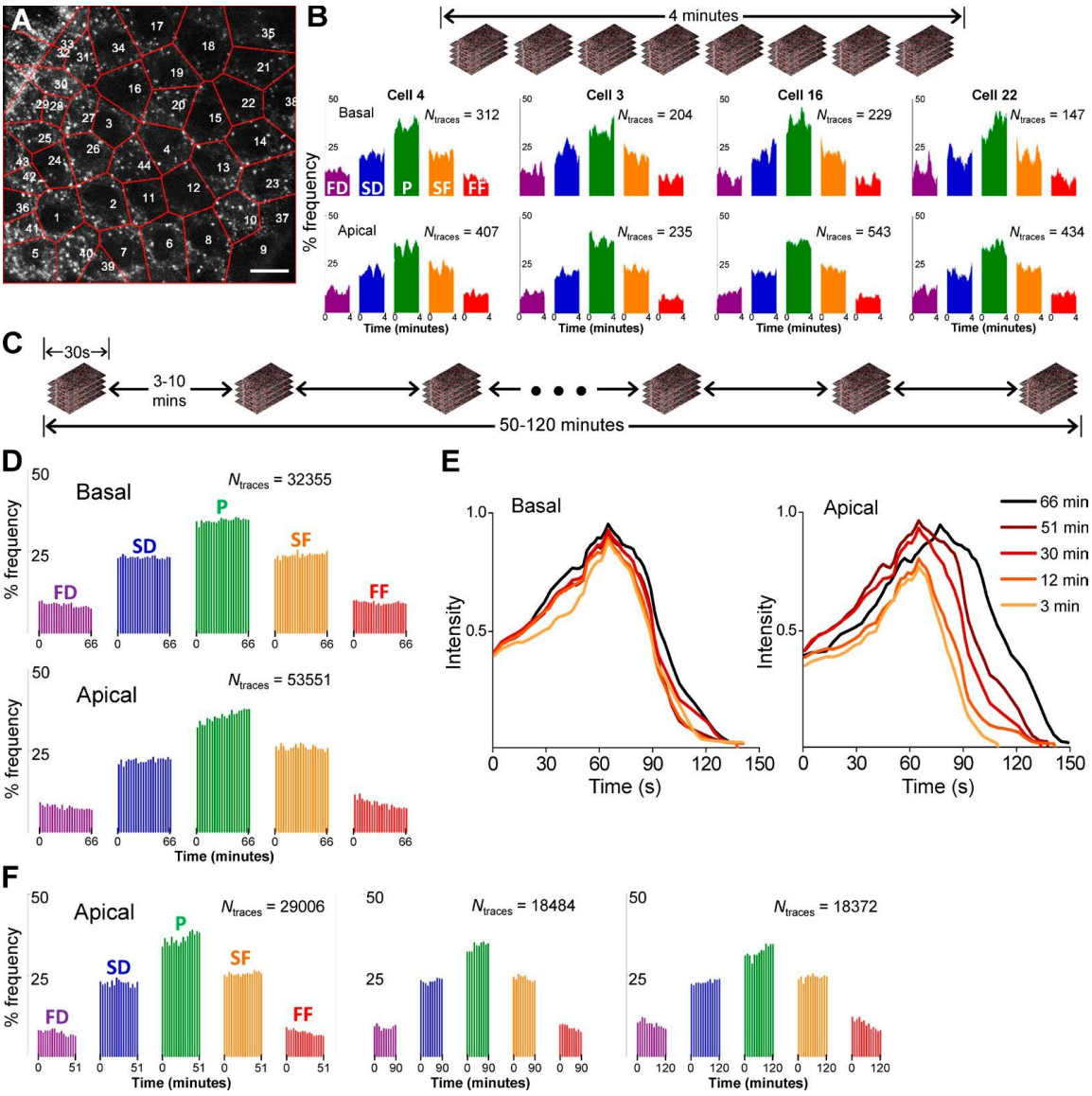

(A) Amnioserosa tissue of a late Drosophila embryo is imaged for 4 min using confocal z-stacks acquired every 3 s. Representative frame is an image section at the middle of a stack. Red lines represent the boundaries between amnioserosa cell centers, which are marked by numbers. Cell boundaries determined in each frame of a 3D time-lapse acquisition. Bar 10 µm. (B) Histograms show evolution of the growth rates corresponding to different cells selected from the amnioserosa tissue in A. Frequencies of the five phases are plotted as a function of time for the apical and basal surfaces. (C) Thumbnails represent 30-s-long 3D time-lapse acquisitions separated by intermissions.

Continued

Figure 2.9: Continued

(D) Transformation of CCS growth rates at the basal and apical surfaces of the amnioserosa during dorsal closure of a *Drosophila* embryo. Each bar in the histograms represents the frequency of growth rates obtained from CCS traces detected in individual 30-s-long acquisitions. A significant change in the growth rates is observed at the apical surface. (E) CCS intensity profiles predicted using the growth rates in (D). The change in the apical CCS dynamics is observed as gradually elongated lifetime (right). No major change is observed in the basal surface dynamics (left). (F) Histograms show the CCS growth rates at the apical amnioserosa of three embryos. Increasing frequency of the plateau phase is a hallmark of reduced CCS dynamics. FD, fast dissolution; FF, fast formation; P, plateau; SD, slow dissolution; SF, slow formation.

2.4 Discussion

We show that clathrin coat growth rates can be used as quantitative reporters of CME dynamics in cellular contexts where errors associated with single-particle tracking are significant. Growth rate distributions obtained from short fragments of CCS traces offer the ability to assess clathrin dynamics from acquisitions shorter than the mean CCS lifetime. Gradual changes in endocytic dynamics can be detected in real time. Mean intensity profiles of the CCS traces that are used to generate growth rate distributions can be reconstructed by finding analogous growth rates in a library of trace clusters. These advantages make growth rate analysis a strong alternative to existing methodologies, which rely on quantifying lifetimes of individual CCSs.

Growth rate analyses reveal that physical factors increasing the energy cost of membrane deformation (e.g., in-plane tension, membrane–cytoskeleton adhesion, and membrane–substrate interactions) slow down formation and dissolution of CCSs. It has been shown that the same energy cost also reduces the curvature of CCSs (Saleem et al.,

2015). In-plane tension is assumed to be homogenous in a cell, but membrane–cytoskeleton adhesion and membrane–substrate interactions are not uniform and, therefore, may induce spatial heterogeneities in dynamics and geometries of CCSs. This heterogeneity may account for the coexistence of clathrin-coated pits and plaques at the ventral surface of certain cell types (Saffarian et al., 2009). Growth rate analyses suggest that flat clathrin arrays and clathrin-coated pits have distinct formation dynamics. Even though flat lattices may acquire curvature over time (Avinoam et al., 2015), our data suggest that this mechanism cannot account for the formation of clathrin-coated pits. Transition of flat clathrin lattices to curved pits requires four-fold reduction in the projected area of clathrin coats on the x–y plane (Fig. 2.13). Such abrupt shape transformations are not observed in recent super-resolved fluorescence acquisitions displaying the formation of clathrin-coated pits (Li et al., 2015), which suggests that curvature of the clathrin coat is constant during pit formation.

Strategies described here lay the groundwork for other quantitative assays that aim to elucidate endocytic processes in various multicellular contexts. Experimental and analytical deficiencies that distort CCS lifetime distributions are less detrimental to growth rates, as their quantification does not rely on tracing the complete lifetime of CCSs. Our research shows that CME dynamics can be assessed within tissues of developing organisms through quantification of the fluorescence growth rates of individual endocytic assemblies. Lifetime distributions obtained from Drosophila amnioserosa are overpopulated by traces that last <20 s, which would be regarded as

Figure 2.13 Flat CCSs and clathrin-coated pits.

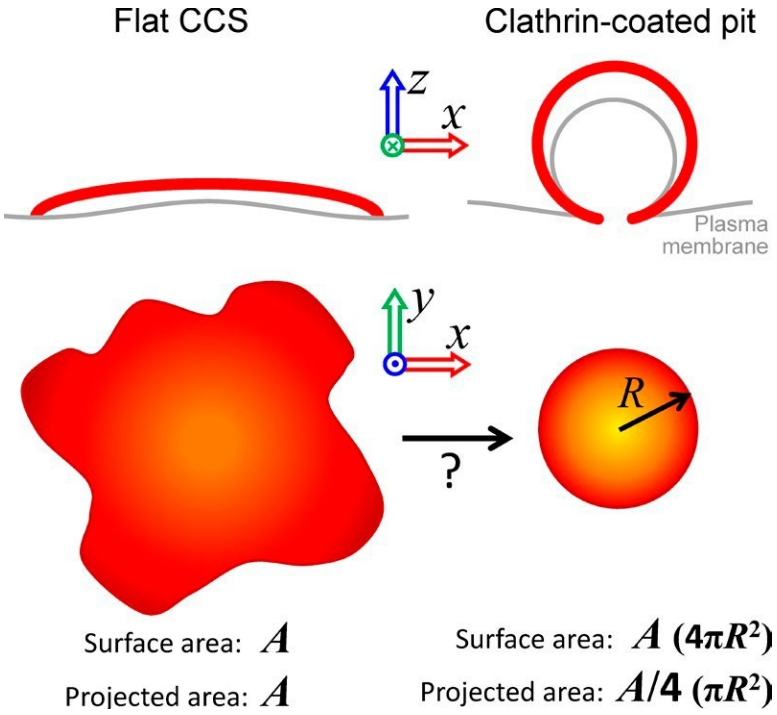

Surface area (A) of a flat CCS is equal to its projected area on the x–y plane. For a clathrin-coated pit, however, the surface area ($A = 4\pi R^2$, where R is the pit radius) is approximately fourfold greater than the projected area (πR^2). Therefore, transformation of a flat CCS into a pit requires a fourfold reduction in the projected area.

abortive structures in in vitro assays. The intensity traces reproduced using growth rate distributions extended to durations longer than the mean clathrin-coated pit lifetime. Longer CCS lifetimes may be a result of the intrinsic tension of the amnioserosa tissue (Kiehart et al., 2000). Likewise, gradual increase in CCS lifetimes during dorsal closure may be induced by the changes in tension levels. This assumption is in accord with a recent study showing that reduction in volume of amnioserosa cells leads to increasing tension during dorsal closure (Saias et al., 2015). Drosophila amnioserosa cells undergo periodic but asynchronous shape changes at shorter time scales (Solon et al., 2009).

Further research is needed to elucidate if rapid fluctuations of CCS growth rates observed in individual cells are correlated with temporal changes in amnioserosa mechanics. Such studies may also elucidate whether dynamics of CCSs can be used as reporters for mechanical states of cells and tissues.

2.5 Materials and Methods

2.5.1 Fluorescence imaging

The imaging system was an Eclipse TI-E microscope (Nikon) equipped with a temperature controlled chamber, a CSU-W1 spinning disk confocal unit (Yokogawa Electric Corporation), a 100× objective lens (Nikon CFI Plan-Apochromat Lambda, NA 1.45) and an EMCCD camera (iXon DU897 Ultra; Andor Technology). 2D and 3D time series were obtained using NIS Elements image acquisition software.

S. Boulant (University of Heidelberg, Heidelberg, Germany) provided BSC-1, MDCK, and U373 cells stably expressing σ2-EGFP. Imaging of cultured cells was performed 8–24 h after plating on glass bottom dishes at 37°C ambient temperature (Greiner Bio-One), unless stated otherwise. Cells were imaged at a rate of 0.25–0.5 Hz and laser exposure of 50–300 ms per frame. Imaging medium was phenol red–free L15 (Thermo Fisher Scientific) supplemented with 10% FBS. Serum-free L15 was used for cholesterol depletion experiments. Final concentration of MβCD (Sigma-Aldrich) was 10 mM in Fig. 2.7, Fig. 2.9 C, and 4mM in Fig. 2.6B. Latrunculin B (SigmaAldrich) was used at the final concentration of 2 μM.

Drosophila embryos were harvested from a cross between male flies homozygous for GAL4-Arm and female flies homozygous for CLC-GFP (Bloomington Drosophila Stock Center). Eggs laid by this cross were collected and allowed to develop for ~11 h at 25°C (stage 14 of development). The embryos were then mounted on a slide with glue (ventral side up), immersed in halocarbon oil (to prevent drying out), and covered with a coverslip. Amnioserosa tissues were imaged at 22°C using 3D time-lapse acquisitions containing ~20 planes (400 nm apart) exposed for 50–100 ms. Temporal gap between adjacent z-stacks was 3 s.

2.5.2 Micropipette Aspiration

Glass micropipettes (BF100-58-10) were pulled using a micropipette puller (P-97; Sutter Instrument). A custom stage was built to mount a Sutter Instrument BRM/E micromanipulator to the live-cell imaging platform. Suction pressure was controlled with a Sutter Instrument BRE110/E microinjection system. Cell aspiration was performed with a 5- to 10-μm microneedle at the dorsal surface of cells, and the clathrin activity at the ventral surface was recorded with spinning-disk fluorescence imaging. P. Selvin (University of Illinois at Urbana-Champaign, Urbana, IL) provided the micromanipulator and injection system. See Appendix A for additional details.

2.5.3 Single-particle tracking

2D particle tracking was performed using the cmeAnalysis software (obtained from http://lccb.hms.harvard.edu/software.html) unless stated otherwise. TraCKer software is a less sophisticated but faster tracking algorithm that lacks the advanced forward-

backward-forward rechecking and intelligent thresholding of cmeAnalysis. It also lacks the 2D Gaussian fitting of point-spread functions and uses integrated pixel intensity as the CCS signal. TraCKer uses a simple threshold determined over a Mexican hat filtered image for detection of fluorescent spots. CCS positions are located using the intensity-weighted center of the point-spread function. In this work, TraCKer was used for the sole purpose of testing growth rate analysis on IMSs.

cmeAnalysis software occasionally detects objects that last a single frame or persist consistently in the background without following an intensity path that could be considered as a CCS. We implemented a sorting scheme for these traces, requiring that they be at least three frames long and at some point meet statistical criteria for demonstrating a linear increase or decrease in intensity (corresponding to CCS growth and dissolution, respectively). We went over every three or four consecutive intensity points (three for traces that last for <10 frames and four for longer traces) and performed a least-squares fit. Traces that had no fits with r^2 value >0.75 were rejected. Rejected traces were not used in calculation of growth rate distributions. Traces with at least two separate high r^2 values of both positive slope (growth) and negative slope (dissolution) were valued most highly. Figure 2.14 shows the classification of CCS traces obtained from amnioserosa tissues.

Figure 2.14 Classification of CCS traces.

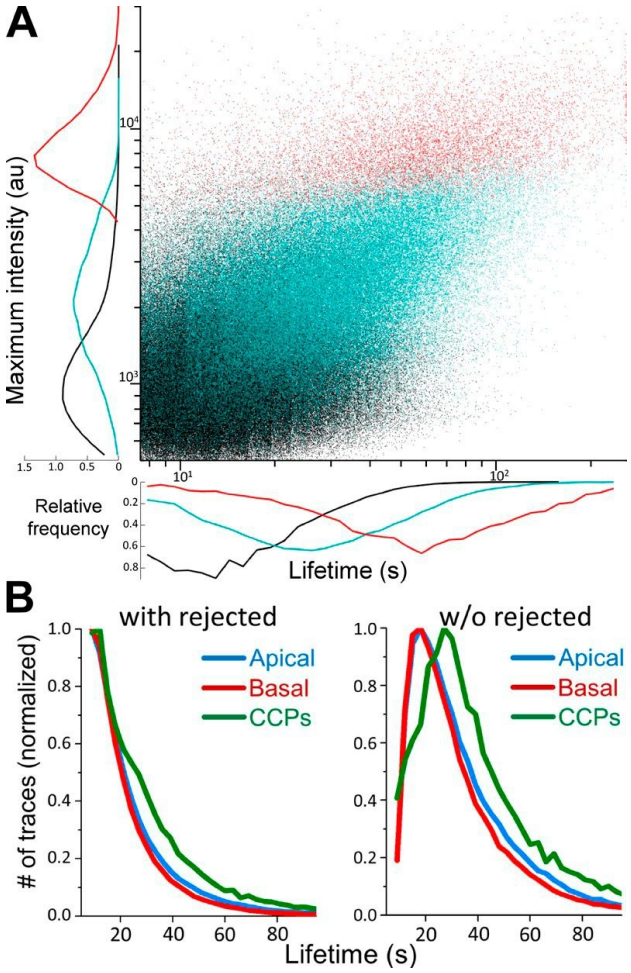

(A) Scatterplot shows lifetime (x-axis) and maximum intensity (y-axis) of CCS traces detected at Drosophila amnioserosa (N_{cells} = 38). We classified the traces into three categories (see Materials an methods): (1) Rejected (black spots, N_{traces} = 204,308). These traces that have very low signal to noise and their growth or dissolutions cannot be determined. Rejected traces are not used in calculation of growth rate distributions. (2) Blobs (red; N_{traces} = 8,805). These are very bright traces that are generally located at the perinuclear regions. (3) Bona fide endocytic carriers (cyan; N_{traces} = 115,253). Next to each axis are normalized histograms to help elucidate the density of points. Because lifetimes are in discrete frames, they have been spread with an even random distribution to make the figure intelligible. (B) A comparison of CCS lifetime distributions obtained from apical and basal amnioserosa with clathrin-coated pits (CCPs) detected in cultured BSC-1 cells stably expressing AP2-GFP. The distribution on the right omits the rejected traces, which have low signal to noise (Amnioserosa: $N_{embryos}$ = 2, N_{cells} = 75, N_{traces} = 329,871, and $N_{rejected}$ = 205,858; CCPs: N_{cells} = 3, N_{traces} = 32,743, and $N_{rejected}$ = 20,741).

2.5.4 3D tracking of CCSs within amnioserosa tissues

Each z-plane of a 3D time-lapse movie was analyzed using cmeAnalysis software. Detected 2D traces were then run through our trace rejection scheme. The resulting data were analyzed to combine traces that occur at the same lateral position in two adjacent z-planes. Coincident traces had to be within one pixel (160 nm) x–y distance for at least three consecutive frames. For each time point in the movie, the resulting trace contains the maximum intensity value of all traces considered for combination. Axial positions were assigned by calculating the intensity-weighted mean z-position of all traces considered. The algorithm for trace combination ran from the outermost z-planes to the innermost (alternating between the top and the bottom) to ensure that there was no directional bias and all possible trace combinations were considered. The resulting data structure will have the duplicate traces deleted and contain sub-plane z-position data where possible. See Appendix B for additional details.

2.5.5 Classification of apical and basal CCSs and blobs

Because of the curvature of the dorsal surface, cells in the amnioserosa tissue are not coplanar. Therefore, the field of view was divided into 64 equal square regions, and apical and basal surfaces were determined for each region independently (Fig. 2.10 B). Axial positions of the traces detected inside each square region were put together within a two-frame temporal radius. These values were binned into discrete z-plane positions, and the resulting count-value graph was fit with two Gaussian functions. The fit for the apical surface has a low standard deviation. The basal surface was found at a higher axial

position and the corresponding Gaussian fit had a larger standard deviation in general. Traces found at the mean or within one standard deviation of their respective Gaussian fits were classified as apical or basal for each of the 64 squares. The brightest 2% of all traces were classified as blobs and were excluded from the apical and basal populations.

2.5.6 Determining amnioserosa cell boundaries

To determine the positions of amnioserosa nuclei, the middle imaging plane of each z-stack was filtered with a Gaussian filter. Each frame was then inverted and local maxima were determined using the FastPeakFind function (A. Natan, PULSE Institute, Stanford, CA). After multiple nuclei positions were determined for each frame, they were tracked using the TraCKer algorithm. Once the centers were known and connected for each frame, the boundaries were determined by creating a Voronoi diagram using the cell centers in each frame.

2.5.7 Growth rate distributions

Slopes were extracted from CCS traces that pass the trace rejection scheme. We found that CCS lifetime distributions obtained from accepted (non-rejected) traces were very similar to those reproduced by others who used different parameters to distinguish genuine endocytic transporters (Fig. 2.14; Aguet et al., 2013). Each trace was normalized by subtracting a global background and dividing by the new maximum of the trace. From this normalized trace, every 12-s interval was used in a least-squares fit to determine the slope of the trace at all frames (Fig. 2.1 C). A trace had to be at least 12 s long to be considered for slope extraction. 12 s was chosen because it evenly divides 1-, 2-, 3-, and

4-s frame rates, which are the most common frame rates used. An arbitrary bin width (0.03) was assigned for the histograms displaying the five distinct growth phases.

2.5.8 Hierarchical clustering of intensity profiles and library lookup

Representative traces were created by combining similar intensity traces within a single cell using a standard hierarchical clustering algorithm. The metric used was the mean squared Euclidean distance, with the condition that the lifetimes of the traces were within 10 s of each other. To compare clusters, we used complete linkage clustering; that is, we used the distance between the farthest two component traces. After clustering, clusters with a minimum of eight traces were added to our trace library. For such clusters, the mean of the component traces was calculated. These mean traces were normalized to the mean maximum trace intensity of the cell to compensate for cells' differing expression levels and imaging conditions. Additionally, for each of these clusters, a single growth rate histogram was generated from the combined data of the constituent traces. The library was assembled from clusters obtained from the following cell types and conditions: BSC-1 cells expressing σ2-GFP (before and during aspiration), polarized MDCK cells expressing σ2-GFP (apical and basal surfaces), and U373 cells expressing CLCa-mCherry. Growth rate histograms of test clusters were compared with the histograms of library clusters using the squared Euclidean metric. If the input histogram was generated from trace data that were confined spatially (e.g., single cell in a culture or tissue) and/or temporally (e.g., half a minute long acquisition of the whole tissue), predicted traces are the weighted averages of the 10 closest cluster matches from the CCS

library (Fig. 2.9 C and Fig. 2.12 E). For this procedure, the library clusters were sorted from closest to farthest by calculating the squared Euclidean distance between their growth slope histograms, and each cluster's contribution to the mean is weighted by the factor $(10 - i)$, where i is the cluster's index in the sorted list and the first index is $i = 0$.

2.7 Acknowledgements

We thank Dr. Steve Boulant for BSC-1, MDCK, and U373 cells stably expressing σ2-EGFP; Dr. Paul Selvin for the micromanipulator and injection system; Vannimul Hem (Ohio State University) for the help with the micromanipulation experiments; and Dr. Michael Sheetz (Columbia University) and members of our laboratory for helpful discussions.

Chapter 3 Mechanoregulation of clathrin-mediated endocytosis

Derived from: Ferguson, J.P., Huber, S.D., Willy, N.M., Aygün, E., Goker, S., Atabey, T., and Kural, C. (2017). Mechanoregulation of clathrin-mediated endocytosis. J. Cell Sci. *130*, 3631–3636.

In this chapter my contributions are some micropipette aspiration experiments; simplification of growth rate histograms into a single standard deviation value; analysis of micropipette aspiration data; all cell compression experiments and analysis; some osmoshock experiments and analysis; and overnight imaging for viability of cells following compression.

3.1 Abstract

We characterized the tension response of clathrin-mediated endocytosis by using various cell manipulation methodologies. Elevated tension in a cell hinders clathrin-mediated endocytosis through inhibition of de novo coat initiation, elongation of clathrin coat lifetimes and reduction of high-magnitude growth rates. Actin machinery supplies an inward pulling force necessary for internalization of clathrin coats under high tension. These findings suggest that the physical cues cells receive from their microenvironment are major determinants of clathrin-mediated endocytic activity.

3.2 Introduction

During formation of an endocytic vesicle, clathrin heterohexamers assemble into a multifaceted cage that is linked to the plasma membrane by clathrin adaptors. Tension on the membrane hinders this process as it increases the energy cost of curvature formation (Sheetz, 2001). Curvature-bearing clathrin-coated pits are replaced by less-dynamic shallow coats when tension is elevated (Saleem et al., 2015). In various cellular contexts, actin dynamics supplements the energy required for formation of clathrin-coated vesicles under high membrane tension (Aghamohammadzadeh and Ayscough, 2009; Boulant et al., 2011; Kaur et al., 2014). However, actin-dependent clathrin-mediated endocytic events have a longer duration than their counterparts taking place at lower tension levels (Boulant et al., 2011). Here, we characterized the regulation of clathrin coat dynamics by membrane tension by using cell manipulation techniques (i.e. microaspiration, cell squeezing and hypo-osmotic swelling) coupled with fluorescence live-cell imaging. Our results show that the density of endocytic clathrin-coated structures on the plasma membrane depends on tension, and actin machinery rescues internalization of clathrin coats under high tension by moving clathrin coats away from the membrane.

3.3 Results

We used three independent approaches to increase the tension on the plasma membrane while monitoring clathrin coat dynamics at the ventral (adherent) surface of cells. Applying negative pressure on the plasma membrane by micropipette aspiration is an

Figure 3.1 Aspiration of the plasma membrane slows down clathrin coat dynamics.

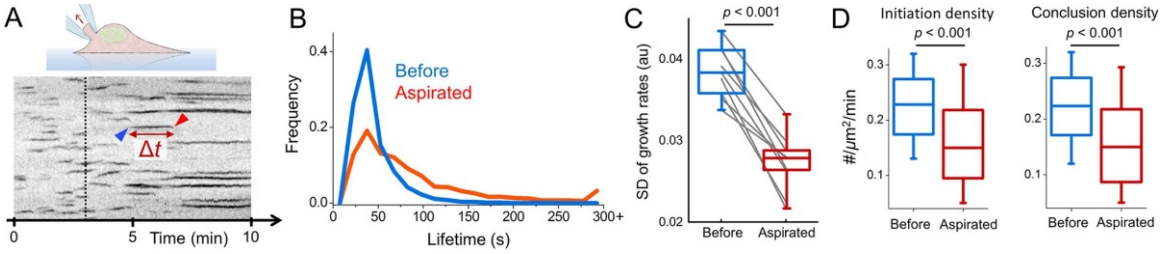

(A) Kymograph showing the clathrin activity at the ventral surface of a BSC1 cell expressing AP2–eGFP. Clathrin coat traces elongate gradually upon microaspiration (dashed line). Blue and red arrowheads mark the initiation and conclusion of a clathrin-coated structure, respectively. Δt is its lifetime. (B) Clathrin coat lifetime distributions are shown for nine BSC1 cells imaged before and during microaspiration (n_{traces}=40,943). (C) For the same nine cells, the standard deviation of the clathrin growth rate distributions are shown in boxplots. Lines connect the standard deviation values obtained from the same cell before and during aspiration. The narrower growth rate distributions indicate slower clathrin coat dynamics. (D) Box plots are the initiation and conclusion densities of clathrin-coated structures before and during aspiration. In the boxplots, the box represents the 25–75th percentiles, and the median is indicated. The whiskers show the 10–90th percentiles. P-values were obtained with a two-tailed t-test.

effective way to increase tension (Herant et al., 2005; Houk et al., 2012). We detected a significant increase in average clathrin coat lifetime (time elapsed between the origination and conclusion of the coat; 44±23 s versus 88±73 s, mean±s.d., P< 0.001; n_{cells}=9, n_{traces}=40,943; Fig. 3.1A,B) in BSC1 cells upon microaspiration of the membrane. The impeded clathrin coat dynamics is also observed as gradual disappearance of high-magnitude growth rates in clathrin traces (Chapter 2). As a result, the standard deviation of clathrin growth rate distributions reduced [0.038±0.003 (before aspiration) versus 0.027±0.004 (during aspiration), P< 0.001; Fig. 3.1C]. We also found that increased tension reduced the surface density of clathrin coat initiation and conclusion events (Fig. 3.1D).

To induce faster changes in plasma membrane tension, we increased the hydrostatic pressure in cells by squeezing them with a micromanipulator-controlled polymer cushion (Fig. 3.2A, B). We used growth rate distributions obtained from clathrin coat intensity profiles to temporally resolve the fast alterations in endocytic dynamics (Chapter 2). In good agreement with the microaspiration experiments, fast dissolution and fast formation phases in the growth rate distributions diminished with the increasing tension, whereas the frequency of the plateau phase increased (Fig. 3.2C; Fig. 3.3). Discrete changes in the tension could be resolved as a stepwise reduction in the standard deviation of clathrin growth rates (Fig. 3.2D). Furthermore, the average clathrin coat lifetimes increased while initiation and conclusion densities reduced (Fig. 3.2B, E). When we relieved the squeezing to verify the viability of cells, we found that the parameters determining clathrin coat dynamics reverted to normal (Fig. 3.2F; Fig. 3.4).

Figure 3.2 Cell squeezing induces fast and reversible alterations in clathrin coat dynamics.

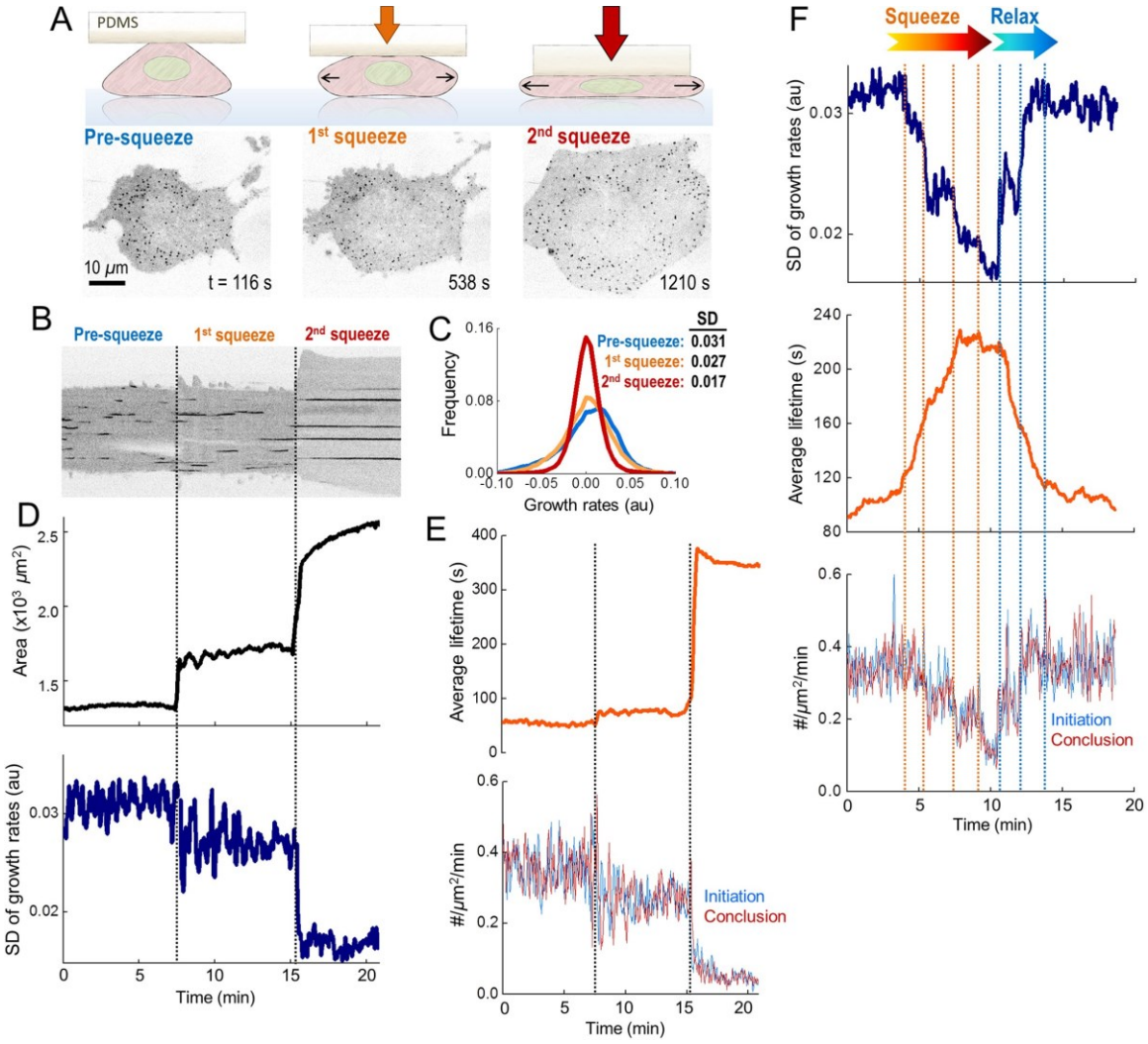

(A) Cartoon and representative frames of a BSC1 cell are shown at different stages of squeezing. (B) Kymograph showing the temporal evolution of the clathrin traces detected at the ventral surface of the cell shown in A. Dashed lines mark the squeezing steps. (C) For the cell in A, normalized distributions of clathrin growth rates are plotted for different squeezing levels (Fig. 3.3). The standard deviation of the distribution reduces as the tension increases. (D) For the same cell, the time variation of the ventral surface area (upper) and the standard deviation of the clathrin growth rates (lower). The stepwise changes in these parameters are due to discrete levels of squeezing. (E) The response of the same cell to squeezing is shown as the mean clathrin lifetime (upper) and initiation and conclusion densities (lower). Dashed lines indicate change in squeezing (n_{traces}=8217). (F) Standard deviation of clathrin growth rates (upper), mean lifetime (middle), and initiation and conclusion densities (lower) from a cell that undergoes increased stepwise squeezing (orange dashed lines) and relaxation (blue dashed lines) (n_{traces}=8255).

Figure 3.3 Growth rate histograms of cell compression.

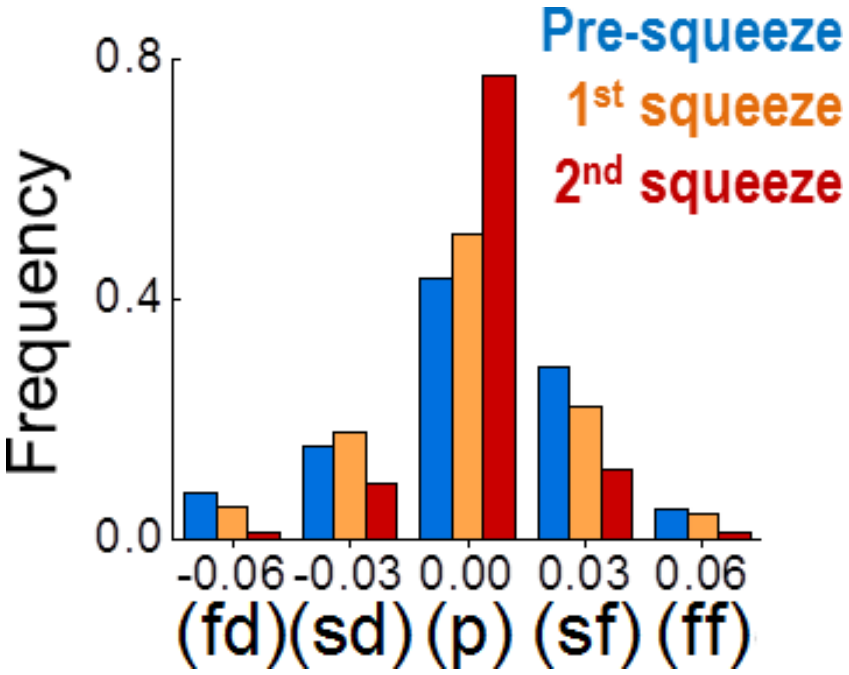

The growth rates at distinct levels of squeezing (Fig. 3.2C) are assembled in five bins that represent the different phases of clathrin-coated vesicle formation (fd, fast dissolution; sd, slow dissolution; p, plateau; sf, slow formation; ff, fast formation).

Hypotonic swelling is a straightforward and widely used approach to increase membrane tension (Boulant et al., 2011; Cocucci et al., 2014; Diz-Muñoz et al., 2016). Upon reducing the osmolarity of the imaging medium, we found that the hypotonic swelling takes effect within minutes but the volume of cells converges back to the original values within an hour (Fig. 3.5A). As expected, the temporary increase of the tension due to stretching of the membrane affected endocytic clathrin coat dynamics only temporarily (Fig. 3.5B). We found that the average lifetime of clathrin-coated structures increased significantly in SUM159 cells (Aguet et al., 2016) under hypo-osmotic shock (87±86 s versus 161.2±208.1 s, mean±s.d., $P< 0.001$; $n_{cells}=12$, $n_{traces}=34,113$; Fig. 3.5C).

Figure 3.4 Recovery from cell compression.

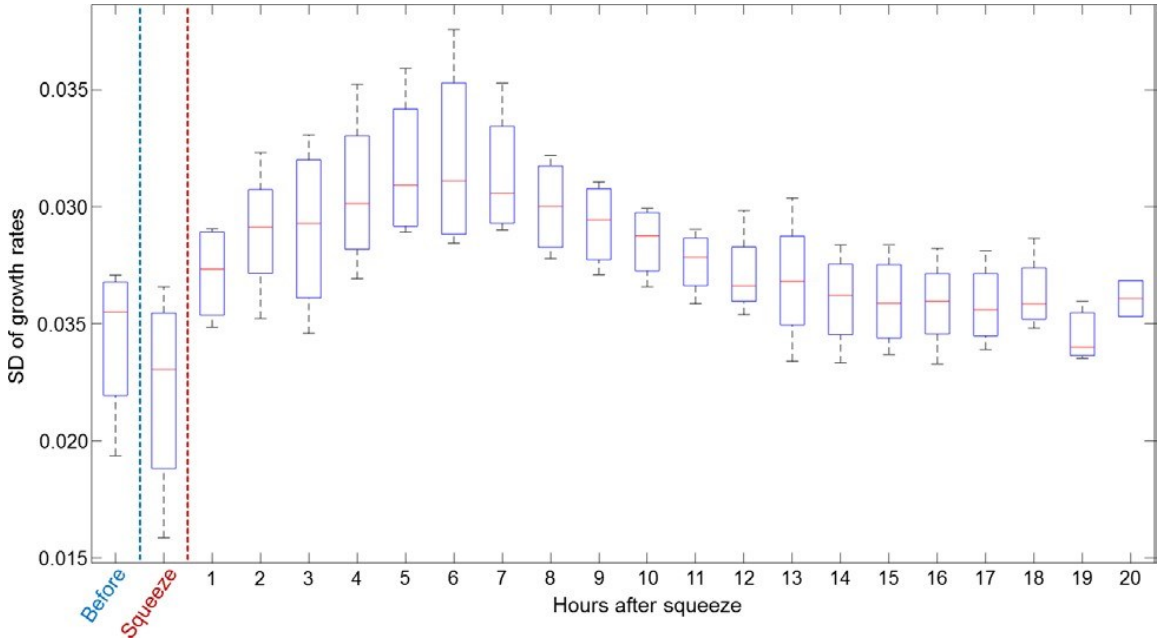

To verify the viability of BSC-1 cells after squeezing we monitored the clathrin coat activity for up to 20 hours. We imaged cells for 2 minutes in each hour to minimize photobleaching and phototoxicity. The box plots show the SD of clathrin coat growth rates determined at different time points (N_{cells} = 4, N_{traces} = 139678). The increased SD of growth rates after squeezing step signifies the retrieval of the endocytic dynamics in cells. Boxes extend to the quartiles, with a line at the median. Whiskers extend from the minimum to the maximum value.

In accordance with the microaspiration and cell squeezing assays, increased tension resulted in reduction of the standard deviation of clathrin growth rates [0.018 ±0.003 (pre-osmoshock) versus 0.014±0.002 (post-osmoshock), P< 0.001; Fig. 3.5D], and initiation and conclusion densities (Fig. 3.5E).

Figure 3.5 Hypotonic swelling inhibits clathrin coat dynamics temporarily.

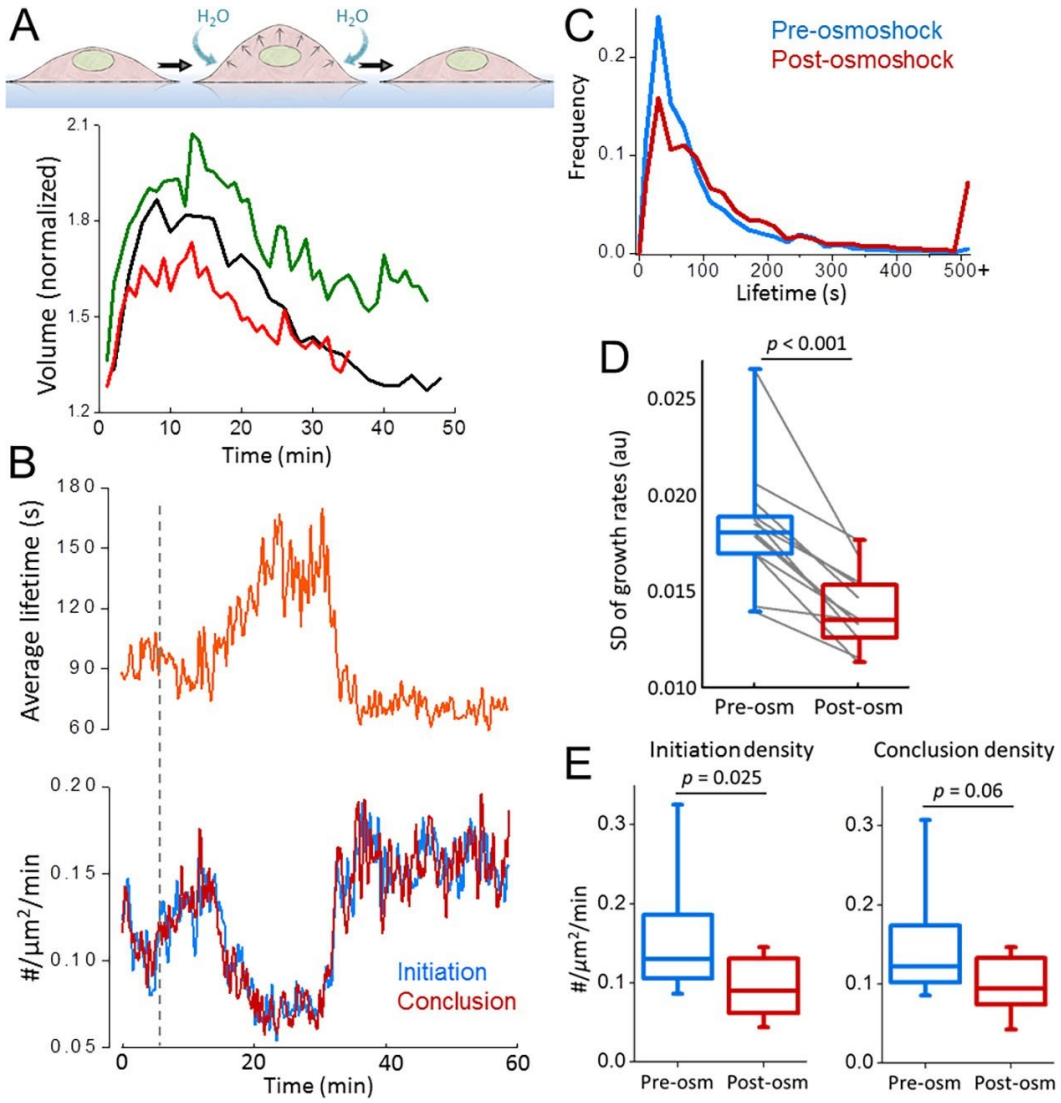

(A) Change in the volume (normalized to the initial value) is plotted for three BSC1 cells during hypotonic swelling (i.e. osmoshock). (B) Mean clathrin coat lifetime (upper), and initiation and conclusion densities (lower) are plotted against time for a BSC1 cell treated with hypotonic shock (dashed line). (C) Clathrin lifetime distributions are assembled pre- and post-osmoshock for 12 gene-edited SUM159 cells expressing AP2–eGFP (n_{traces}=34,113). (D, E) For the same cells, the standard deviation of clathrin growth rates (D) and initiation and conclusion densities of clathrin-coated structures pre- and post-osmotic shock (E) are shown in boxplots. Lines connect the standard deviation values obtained from the same cell pre- and post-osmoshock. In the boxplots, the box represents the 25–75th percentiles, and the median is indicated. The whiskers show the 10–90th percentiles. P-values were obtained with a two-tailed t-test.

As plasma membrane tension increases, actin polymerization energy becomes indispensable for narrowing of the neck between clathrin-coated pits and the plasma membrane. Therefore, inhibition of the actin machinery arrests clathrin coats prior to the scission phase (Boulant et al., 2011). There are two proposed models for actin-dependent formation of clathrin-coated vesicles under high tension (Hassinger et al., 2017). The first model predicts a vertical force generated by actin polymerization to move the clathrin coat away from the plasma membrane. The second model suggests formation of an actin collar that constricts the neck region directly (Collins et al., 2011). By tracing the three-dimensional (3D) displacement of clathrin-coated structures, Scott Huber found that coats move ∼100 nm into the cell before uncoating, and the inward displacement is significantly higher when the membrane tension is increased by hypotonic swelling (Fig. 3.6A, B). He also found that the axial velocity of the inward movement is the highest during the fast dissolution phase of clathrin coats (Fig. 3.6C). He adapted a master–slave approach (Aguet et al., 2013) to monitor the intensity profiles of clathrin coats (AP2σ1–eGFP as the master; hereafter denoted AP2–eGFP) and colocalizing actin filaments (LifeAct– mCherry as the slave), simultaneously. As expected, the LifeAct signal peaked during the later stages of clathrin-coated vesicle formation (Fig. 3.6D), and the axial velocity detected during the fast dissolution phase reduced significantly when the actin dynamics is inhibited upon jasplakinolide treatment (Fig. 3.6E). These results indicate that actin polymerization provides the inward force that is required for constriction of the

Figure 3.6 Actin dynamics mediate the inward movement of clathrin coats prior to disassembly.

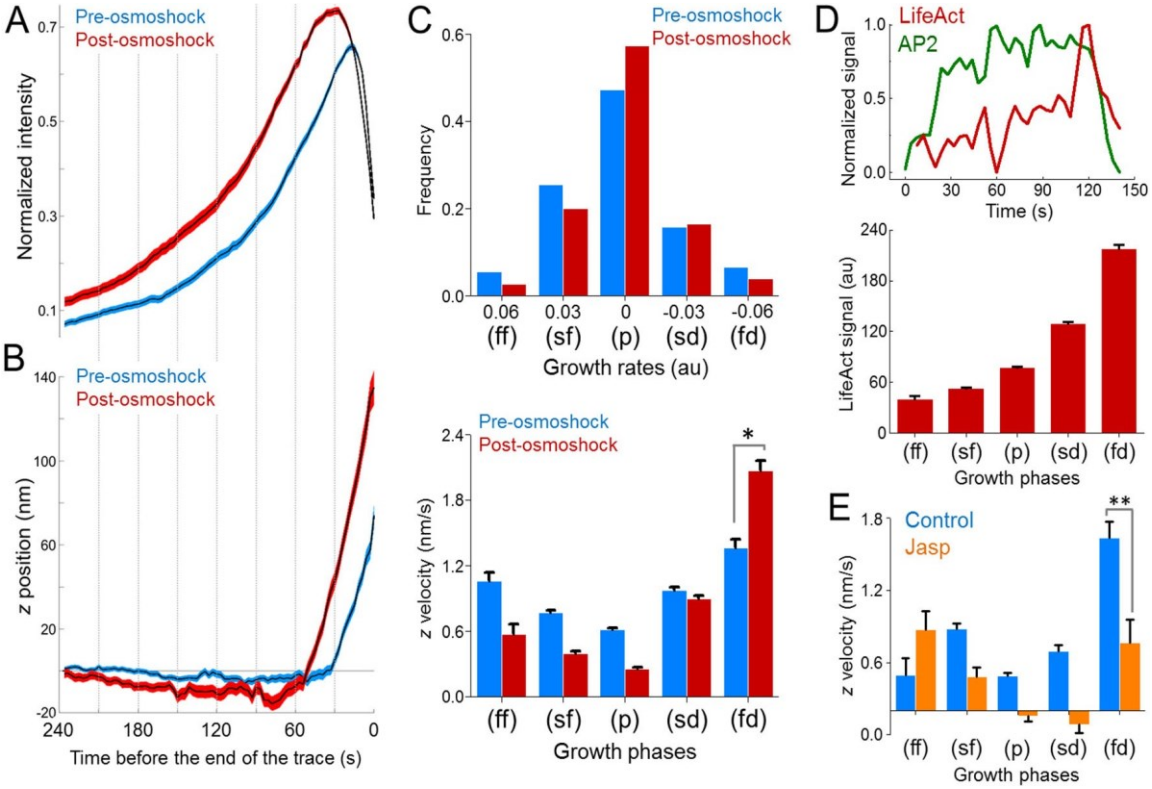

(A) Mean±s.e.m. values for of normalized AP2 intensity traces (determined for a SUM159 cell before and after hypotonic swelling; n_{traces}=3728). The traces are aligned at the end point before averaging. (B) Mean±s.e.m. z displacements are shown for the two trace groups in A. (C) Top, growth rate distributions are assembled for eight SUM159 cells before and after hypotonic swelling (n_{traces}=30,409). Different growth phases (ff, fast formation; sf, slow formation; p, plateau; sd, slow dissolution; fd, fast dissolution) were determined by quantifying the change in the clathrin coat signal over 12-s-long time windows (Chapter 2). Bottom, for the same cells, bar plots show the mean+s.e.m. of the z velocities of the trace fragments (12 s long) that are used to generate the growth rate distributions above. Trace fragments that have the highest z velocity are found in the fast dissolution (fd) phase. (D) Top, representative intensity traces of AP2 (green) and LifeAct (red) fluorescence during the formation of a clathrin-coated vesicle at the ventral surface of a BSC1 cell. Bottom, the relative LifeAct intensity (mean±s.e.m.) colocalizing with clathrin coats is shown for different growth phases (n_{cells}=4, n_{traces}=28,795). Note that the growth phases are determined by using the master (AP2–eGFP) signal. (E) Bar plots show the z velocities (mean±s.e.m.) corresponding to different growth phases for AP2 traces obtained from BSC1 cells in the absence and presence of jasplakinolide (Jasp) (Control, n_{cells}=7, n_{traces}=20,204; Jasp, n_{cells}=6, n_{traces}=35,972). *P<0.0001; **P<0.001 (two-tailed t-test). Note: The data presented in this figure was collected and analyzed by Scott Huber.

neck under high membrane tension, a mechanism analogous to clathrin-mediated endocytosis in yeast (Aghamohammadzadeh and Ayscough, 2009).

3.4 Discussion

We used quantitative live-cell imaging in combination with diverse cell manipulation techniques to detect the changes in clathrin coat dynamics as cells undergo mechanical perturbations. This powerful approach allowed us to investigate the response of individual cells to mechanical stimuli in real time, rather than making a comparative analysis between different cells. Collectively, our assays reveal an inverse relationship between plasma membrane tension and endocytic clathrin coat dynamics. Increased tension manifests itself as reduced initiation and conclusion densities, elongated lifetime, and a reduced standard deviation of clathrin coat growth rates. These results suggest that the reduced density of clathrin-coated structures observed during mitosis (Aguet et al., 2016) and at the lamellae of migrating cells (Kural et al., 2015) can be a product of increased membrane tension (Fogelson and Mogilner, 2014; Kaur et al., 2014; Lieber et al., 2015; Raucher and Sheetz, 1999). Correspondingly, previously described feedback regulation between membrane tension and membrane-bending proteins in migrating cells (Tsujita et al., 2015) can explain the stark increase in clathrin coat density upon mechanical inhibition of cell protrusion.

Our results show that tension is an effective, fast-acting and reversible regulator of clathrin-mediated endocytosis. To induce hypotonic swelling, we reduced the osmolarity of the imaging medium to 63 mOsm. In a recent study, comparable changes in osmolarity are shown to increase the membrane tension ~2-fold (Diz-Muñoz et al., 2016). This is within the boundaries of physiologically relevant variances in plasma

membrane tension given that spreading of a cell results in an ~3-fold reduction in membrane tension (Gauthier et al., 2009), and the tension at the apical surface of polarized cells is ~2.5-fold higher than that at the basal surface (Dai and Sheetz, 1999). Compression of cells by surrounding mechanical cues has been proposed to control tissue morphogenesis at different stages of metazoan development (Desprat et al., 2008; Legoff et al., 2013; Rauskolb et al., 2014). In our cell-squeezing assays, we observed changes in clathrin-mediated endocytic activity even when the relative fold change in the cell area is lower than the levels detected in developmental processes associated with cell compression (Aegerter-Wilmsen et al., 2012) (Fig. 3.7). Dynamics and organization of the actin cytoskeleton were unperturbed in these assays. These findings suggest that morphological alterations involving mechanical forces within physiological contexts can induce abrupt changes in clathrin coat dynamics. Consequently, mechanoregulation of clathrin-mediated endocytosis can influence related biological processes that are central for development and homeostasis of multicellular organisms, such as signal transduction and cell shape regulation.

Figure 3.7 Compression is less than in developmental processes.

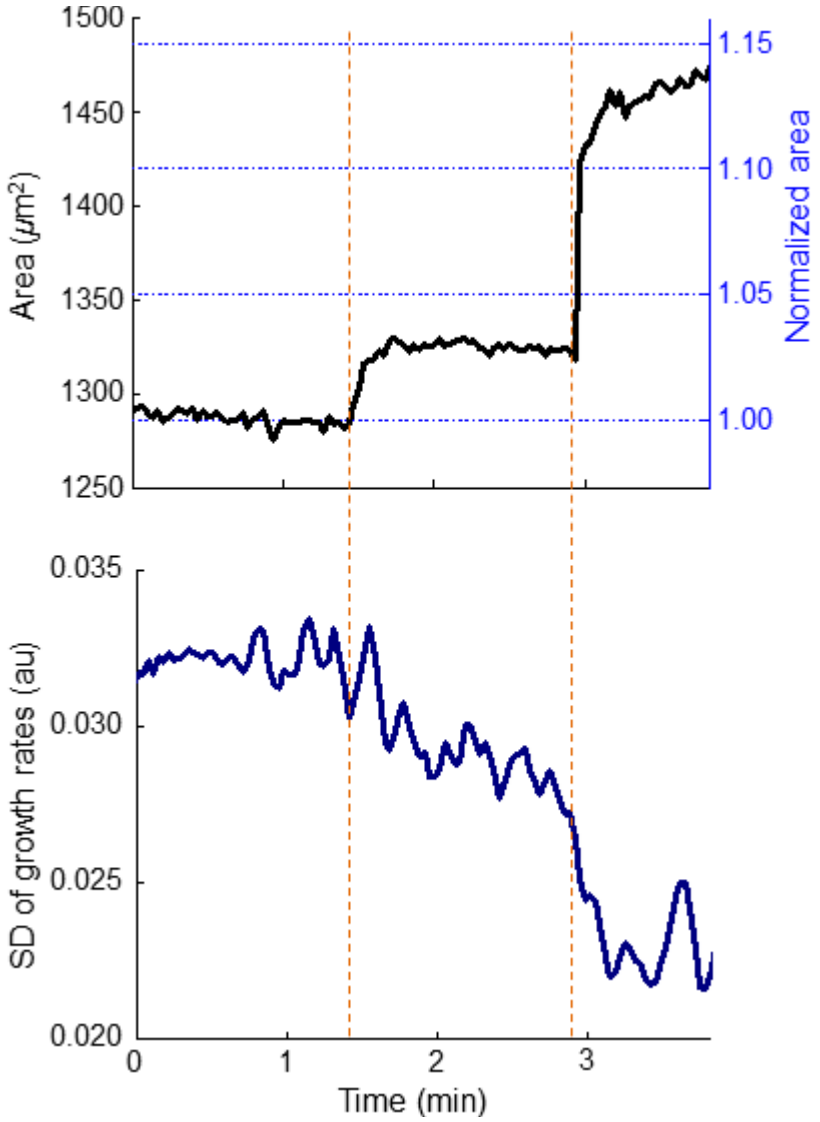

During development of the Drosophila wing imaginal disc, compression of the tissue changes the projected area of the center cells ~1.5 fold (Aegerter-Wilmsen et al., 2012). In our squeezing experiments, compressions that result in milder changes in the projected cell area produce observable changes in clathrin coat dynamics. The upper panel shows the change in the area of a BSC-1 cell during two squeezing steps (shown by the orange dashed lines). The axis on the right shows the cell area normalized to the average pre-squeeze level. The lower panel is the change in the SD of clathrin coat growth rates.

3.5 Materials and Methods

3.5.1 Cell culture, reagents and fluorescence imaging

BSC1 cells stably expressing AP2–eGFP (gift of Steeve Boulant, Department of Infectious Diseases, Virology, Heidelberg University, Germany) were grown in Dulbecco's modified Eagle's medium (DMEM) containing 10% fetal bovine serum, penicillin/streptomycin. SUM159 cell gene edited to express AP2–eGFP (Aguet et al., 2016) (gift of Tomas Kirchhausen, Departments of Cell Biology and Pediatrics, Harvard Medical School Boston, MA) were grown in F-12 medium containing 5% fetal bovine serum (FBS), penicillin-streptomycin and hydrocortisone. Transient expression of LifeAct–mCherry (gift of Patrick M. Reeves, Vaccine & Immunotherapy Center, Charlestown, MA) in BSC1 cells stably expressing AP2–eGFP was carried out using Lipofectamine 2000 (Invitrogen) following the manufacturer's instructions, and imaging was performed 24–48 h after transfection. The final jasplakinolide (Enzo Life Sciences) concentration used to inhibit actin dynamics was 1 μm.

The fluorescence imaging system is composed of an Eclipse TI-E microscope (Nikon) equipped with a perfect focusing system (PFS), a temperature-controlled chamber, a CSU-W1 spinning disk confocal unit (Yokogawa Electric Corporation), a 100× objective lens (Nikon CFI PlanApochromat Lambda, NA 1.45) and an EMCCD camera (iXon DU897 Ultra; Andor Technology). All image acquisition was performed by using NIS Elements software.

Imaging of cultured cells was performed 30 min after plating on glass bottom dishes (Greiner Bio-One) in the case of squeezing cells. The plating time prior to aspiration and osmotic shock experiments was 24 h. All cells were maintained at an ambient temperature of 37°C during imaging. Images were acquired at rate of 0.25–0.5 Hz with a laser exposure of 50–300 ms per frame. Imaging medium was Phenol Red-free L15 (Thermo Fisher Scientific) supplemented with 10% FBS. The snapshots and movies of fluorescence acquisitions are inverted to increase visibility.

3.5.2 Squeezing, micropipette aspiration and osmotic shock

In squeezing experiments, a 15 µl suspension of cells and imaging medium is plated in the middle of the imaging dish, forming a small droplet. A polydimethylsiloxane (PDMS) brick of ~10 mm×10 mm×2.5 mm is placed on top of the droplet. The dish is capped and the cells are allowed to spread for ~30 min (at this point cells are not in contact with the PDMS). Additional waiting might result in evaporation reducing the height of the PDMS brick where it begins prematurely compressing the cells. After spreading, a micromanipulator (Narishige MMO-202ND, Narishige MMN-1) fitted with a rounded glass pipette tip is slowly brought into contact with the PDMS brick from above. After the glass tip has contacted the brick, L15 is flowed in to fill the chamber to a level just below the top surface of the brick. This procedure is designed to prevent the PDMS brick being displaced from a position directly above adherent cells. The micromanipulator is used to press down on the PDMS while observing the cells under brightfield illumination. Fluorescence acquisitions start after the PDMS brick is brought into the barest contact

with the cells. The maximum acceptable level of compression is signaled by complete halting of clathrin coat activity. Further imaging is performed at various stages while the compression is released. In the microaspiration experiments, a microinjection system (BRE110/E; Sutter Instrument) was used to control the negative pressure applied on the dorsal surface of cells via a 5–10-μm-thick microneedle (see Appendix A for additional details of microaspiration).

For osmotic shock experiments, SUM159 cells are cultured on four-well glass bottom plates (Fisher Scientific) and imaged every 3 s. At 5 min after the start of the experiment, 800 μl of ddH2O is added to the 200 μl of imaging medium to induce hypo-osmotic shock. The measured osmolarity level after this dilution is 63 mOsm. The cells are then imaged for another 20 min to study the cellular response. To compare clathrin coat dynamics before and after osmotic shock, two time windows are analyzed: the preosmoshock time window consists of the 5 min immediately prior to addition of water, whereas the post-osmoshock time window starts 2.5 min after water addition (to allow time for osmotic shock effects fully take hold) and runs for 5 min. For lifetime analyses, only traces whose mean time-point lies within the window are considered.

For the calculation of the cell volume, we used the 3D time-lapse spinning-disk confocal microscopy acquisitions. A custom MATLAB program was written to allow the user to select the boundary of the cell for each plane in a z-stack. The number of pixels inside of these boundaries was multiplied by the size of the pixels to determine the area

of the cell in that stack. The volume was calculated by multiplying this area by the difference in position between the stacks and adding all those values together.

3.5.3 Single-particle tracking

cmeAnalysis software was used for two dimensional (2D) particle tracking (obtained from http://lccb.hms.harvard.edu/software.html) (Aguet et al., 2013). We used exclusionary criteria for the traces that last a single frame or persist consistently in the background without following a characteristic clathrin intensity profile (Chapter 2). Selected traces are at least three frames long and contain a sequence which meets statistical criteria for demonstrating a linear increase or decrease in intensity (corresponding to clathrin coat growth and dissolution, respectively). For each group of three or four consecutive intensity points (three for traces >10 frames and four for longer traces), we performed a least-squares fit. Traces that had no fits with an r^2 value >0.5 were rejected. Rejected traces were excluded from the calculation of initiation and dissolution densities, growth rate distributions, lifetime distributions and lifetime dipoles.

We used the traces that passed the rejection scheme to determine the average clathrin coat lifetime per frame. In each frame, we added together the lifetime of each trace that exists in that frame, and divided by the number of traces considered. The beginning and end of each trace is considered as an initiation and conclusion event, respectively. For each frame, initiation and conclusion densities (number/μm^2 /minute) were determined by finding the number of traces that begin and end in that frame,

multiplying by the frame length (2–4 s), dividing by the visible cell area (in μm^2) and by 60 s.

Scott Huber developed a custom MATLAB program for the master–slave analysis. The traces in the master channel were determined by using the cmeAnalysis software as described above. To quantify the intensity in the slave channel, we determined the average intensity in a 5×5 pixel region around the structure, and then subtracted the background intensity, which was calculated as the average intensity of the outside pixels of the 7×7 pixel region around the structure.

3D traces and growth rate distributions of clathrin coats were determined as described previously (Chapter 2; Appendix B). z-velocities are calculated for each 12-s long trace fragments, which were used to determine the corresponding clathrin growth rates.

Chapter 4 Membrane mechanics govern spatiotemporal heterogeneity of endocytic clathrin coat dynamics

Derived from: Willy, N.M., Ferguson, J.P., Huber, S.D., Heidotting, S.P., Aygün, E., Wurm, S.A., Johnston-Halperin, E., Poirier, M.G., and Kural, C. (2017). Membrane mechanics govern spatiotemporal heterogeneity of endocytic clathrin coat dynamics. Mol. Biol. Cell *28*, 3480–3488.

In this chapter my contributions are some cholesterol depletion experiments and analysis; some cell spreading experiments and analysis; post-mitotic migration experiments; development of growth rate SD maps; analysis of hemocyte frames; and application of growth rate SD maps to the amnioserosa.

4.1 Abstract

Dynamics of endocytic clathrin-coated structures can be remarkably divergent across different cell types, cells within the same culture, or even distinct surfaces of the same cell. The origin of this astounding heterogeneity remains to be elucidated. Here we show that cellular processes associated with changes in effective plasma membrane tension induce significant spatiotemporal alterations in endocytic clathrin coat dynamics. Spatiotemporal heterogeneity of clathrin coat dynamics is also observed during

morphological changes taking place within developing multicellular organisms. These findings suggest that tension gradients can lead to patterning and differentiation of tissues through mechanoregulation of clathrin-mediated endocytosis.

4.2 Introduction

The dynamic properties of clathrin-coated structures can be strikingly diverse. Lifetime can be an order of magnitude disparate within the same cell (Chapter 2). Here we show that cellular processes associated with membrane tension gradients, i.e. spreading and migration, result in increased spatiotemporal heterogeneity of endocytic clathrin coat dynamics. The variations in clathrin coat dynamics coincide with the gradients in plasma membrane tension, which is a potent regulator of endocytic processes (Dai and Sheetz, 1995). We also show that spatiotemporal changes in clathrin coat dynamics take place during developmental processes shaping Drosophila melanogaster embryos.

4.3 Results

Physical factors that increase the energy cost of curvature generation on the plasma membrane slow down formation of clathrin-coated vesicles. Using quantitative imaging of fluorescently tagged clathrin coat components (clathrin or AP2) within live cells, this phenomenon can be observed as elongated coat lifetime (Fig. 4.1A; Boulant et al., 2011). Alternatively, mechanoregulation of CME dynamics can be monitored at distinct surfaces of a cell through growth rate distributions which are assembled by quantifying the changes in the fluorescence signal of individual clathrin coats within short time windows

(Chapter 2). High magnitude growth rates, that is, rapid changes in the clathrin coat intensity corresponding to fast formation and fast dissolution of the coat, diminish with increasing plasma membrane tension. Therefore, the standard deviation (SD) of the growth rate distributions reduces when the effective membrane tension is increased by cholesterol depletion or hypotonic swelling (Fig. 4.1, B–E; Dai et al., 1998; Khatibzadeh et al., 2012; Diz-Muñoz et al., 2016; Sun et al., 2007). Conversely, SD of growth rate distributions increases when tension is reduced on deoxycholate treatment (Fig. 4.1, D and E; Raucher and Sheetz, 1999; Batchelder et al., 2011).

Figure 4.1 Monitoring mechanoregulation of clathrin coat dynamics in real time.

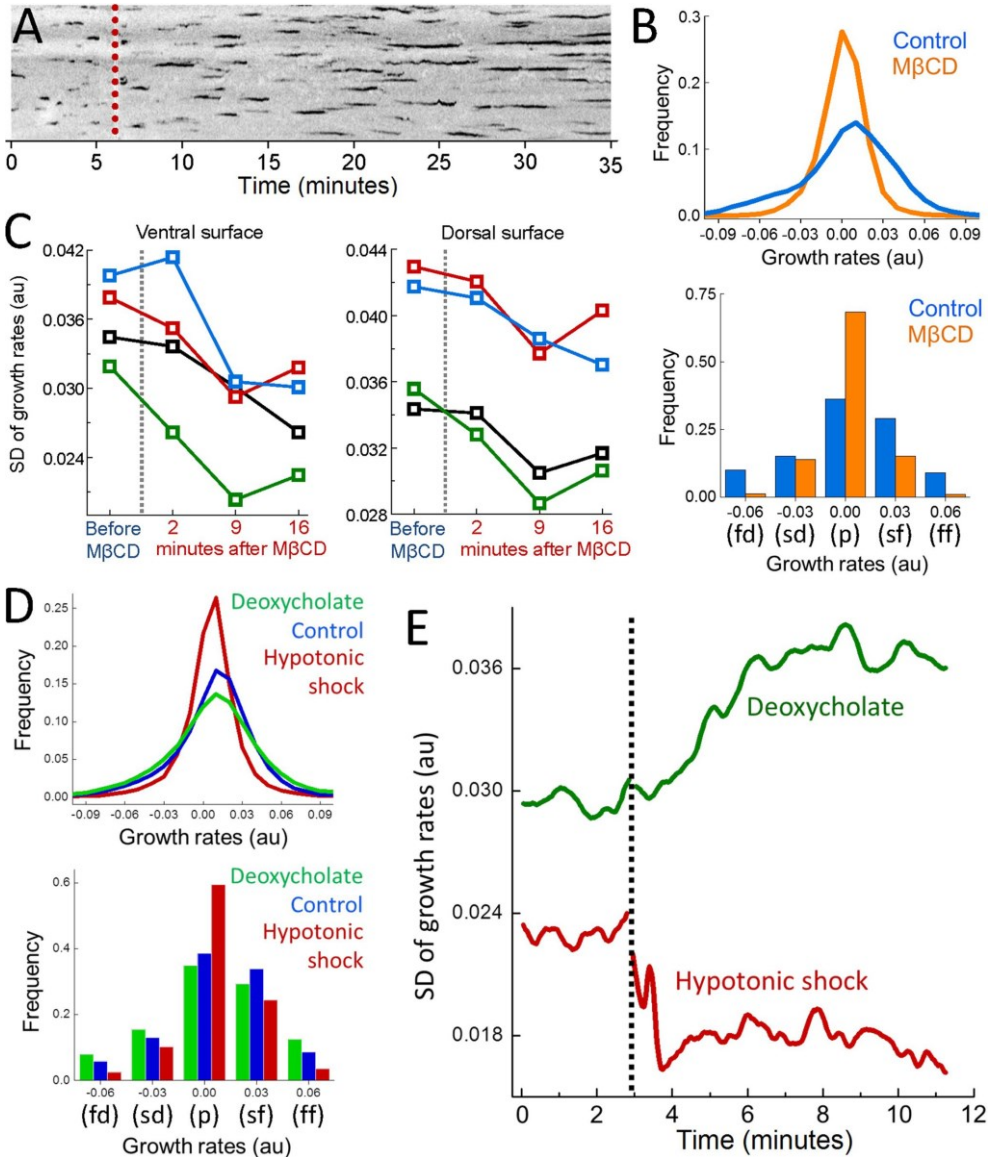

(A) Depletion of plasma membrane cholesterol by methyl-ß-cyclodextrin (MßCD) increases the adhesion energy between membrane and the cytoskeleton and, thereby, inhibits curvature formation by clathrin-coats (Subtil et al., 1999; Sun et al., 2007; Khatibzadeh et al., 2012). A 35-min-long kymograph shows clathrin coat dynamics at the ventral surface of a BSC1 cell stably expressing the σ2 subunit of AP2 fused with enhanced green fluorescent protein (EGFP). The dashed line marks the addition of MßCD. The traces corresponding to individual clathrin-coated structures elongate as clathrin pits are gradually replaced by less dynamic flat arrays (plaques).

Continued

Figure 4.1: Continued

(B) For the cell in A, growth rate distributions are assembled using the traces detected before cholesterol depletion (Control; the first 5 min of the acquisition) and after (MßCD; the last 5 min of the acquisition). As clathrin coat dynamics slow down, growth rate distribution gets narrower (top). The distribution is also displayed using five bins corresponding to five growth phases (bottom; fd: fast dissolution, sd: slow dissolution, p: plateau, sf: slow formation, ff: fast formation). High-magnitude slopes, corresponding to fd and ff phases, diminish due to inhibition of CME. (C) SD of clathrin growth rate distributions are shown for the ventral and dorsal surfaces of four BSC1 cells before and after MßCD treatment. (D) Growth rate distributions are assembled using AP2 traces detected in SUM159 cells under different conditions (top; $N_{cells} = 4$). With application of hypotonic shock (Dai et al., 1998; Diz-Muñoz et al., 2016), CME slows down due to increasing in-plane tension. Deoxycholate treatment reduces membrane tension (Raucher and Sheetz, 1999; Batchelder et al., 2011) and results in increased clathrin coat dynamics. The distributions are also displayed using five bins corresponding to distinct growth phases (bottom). (E) Temporal change in the SD of clathrin coat growth rates is plotted for two SUM159 cells. The dashed line marks the application of hypotonic shock and deoxycholate.

4.3.1 Clathrin coat dynamics in spreading and migrating cells

Membrane tension reduces gradually during cell spreading (Gauthier et al., 2009). Rounded-up cells have approximately threefold greater membrane tension compared with well-spread cells (Fig. 4.2A.; Gauthier et al., 2012; Note: Scott Huber undertook the arduous process of obtaining these measurements of cell tension via membrane tether. He was instructed by Ariel Wurm, a student of Dr. Michael Poirier, and the equipment belonged to Dr. Ezekiel Johnston-Halperin.). We found that the factors defining CME dynamics change significantly in the course of spreading. Figure 4.2B shows the ventral (adherent) surface of a BSC1 cell at different time points of its spreading. AP2 traces are color coded according to the lifetime to illustrate the changes in density and dynamics of clathrin coats throughout spreading. Decreasing membrane tension results in gradual shortening of the average clathrin coat lifetime (Fig. 4.2C). Changes in the SD of growth rates in both ventral and dorsal surfaces demonstrate that clathrin coat dynamics increase

across the entire cell (Fig. 4.2, D and G). We also found that initiation and dissolution densities of clathrin-coated structures increase significantly with the completion of spreading (Fig. 4.2, E and F).

Extension of the cell surface area is associated with increasing membrane tension (Gauthier et al., 2011; Houk et al., 2012; Masters et al., 2013). In good agreement with this observation, we detected a strong correlation between the rate of area extension and average clathrin coat lifetime in spreading cells (Pearson's $r = 0.67$; Fig. 4.2H). This phenomenon is particularly conspicuous in cells that undergo multiple rounds of extension. When spreading is interrupted temporarily, clathrin coat lifetimes converge to the values observed during low tension phases. Lifetimes elongate back to the values observed under high tension as soon as the cells start to spread again (Fig. 4.2I). Together, our findings show that temporal variations in tension have direct effects on dynamics and distribution of endocytic clathrin coats in cells.

Figure 4.2 Clathrin coat dynamics reflect changing membrane tension throughout cell spreading.

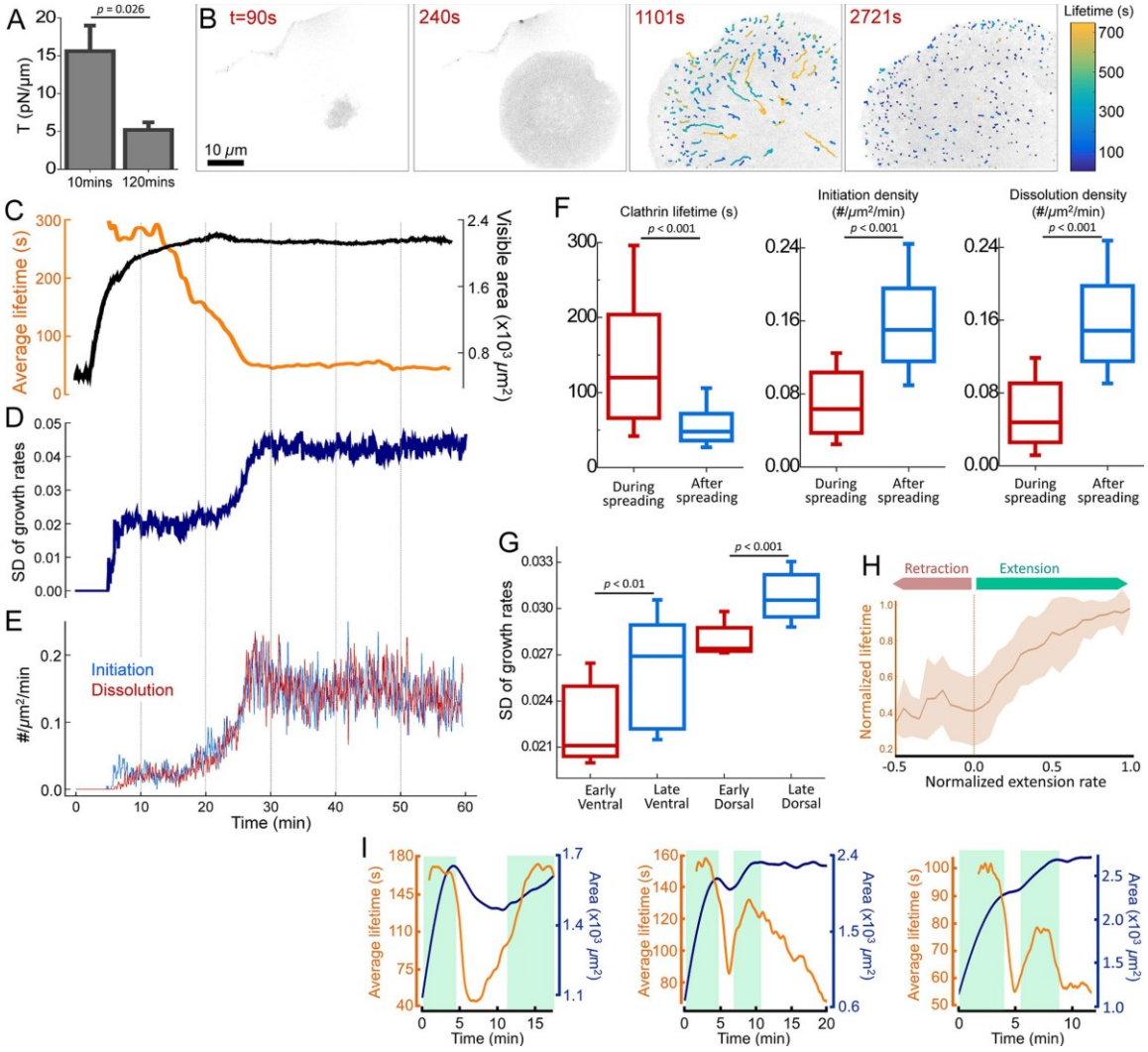

(A) Optically trapped beads are used to measure membrane tether forces of BSC1 cells at early and late stages of spreading. Membrane tension values (mean + standard error) are shown for cells plated for 10 and 120 min (N_{cells} = 12). (B) Snapshots show spreading of a BSC1 cell expressing AP2-EGFP. Detected clathrin coat traces are colored according to the lifetime. (C) Time variations of the average clathrin coat lifetime (orange) and visible spreading area (black) of the cell in B. SD of growth rates (D), and initiation and dissolution densities of clathrin coats (E) are plotted for the same cell. Shortening of lifetimes, increasing SD of growth rates, and increased initiation and dissolution rates establish increased endocytosis rates with the completion of spreading. (F) Box plots show the cumulative comparison of the clathrin coat lifetime and initiation/dissolution densities obtained during and after spreading of BSC1 cells (N_{cells} = 24, N_{traces} = 41,989).

Continued

Figure 4.2: Continued

(G) SD of growth rates are calculated for the ventral and dorsal surfaces of BSC1 cells at early and late stages of spreading (measurements are separated by 30–40 min; $N_{cells} = 11$). Boxes extend to the quartiles, with a line at the median. Whiskers extend from the 10th to 90th percentiles. (H) The plot shows the normalized clathrin coat lifetime (mean±SD) vs. normalized extension rate of the ventral surface (area/time) obtained from 24 spreading cells. (I) Spreading area (blue) and average clathrin coat lifetime (orange) in cells featuring periods of spreading (shaded green regions) as well as retraction or pause. p values were obtained using the two-tailed t test.

Polarization of cells induces spatial heterogeneity in effective membrane tension (Dai and Sheetz, 1999; Lieber et al., 2015). Theoretical studies predict a strong front-to-rear tension gradient at the ventral surface of protruding cells (Fogelson and Mogilner, 2014). We found that the spatial heterogeneity in clathrin coat dynamics outlines the predicted tension gradient at the ventral surface of asymmetrically spreading cells (Fig. 4.3). Figure 4.3B shows clathrin lifetime maps of two spreading cells in which every data point is given the average value of the closest three clathrin coats' lifetime. We found that long-lived clathrin-coated structures are predominantly located in the vicinity of the leading edge. To better quantify this trend, for each time point of spreading, we calculated the lifetime dipole moment, which is a vector pointing in the direction of increasing clathrin coat lifetime. We detected a significant correlation between the direction of the lifetime dipole and the cells' center-of-mass displacement even when cells change directions (Pearson's $r = 0.53$; Fig. 4.3, B–D). As a control, we randomly exchanged the lifetime values between clathrin coats and recalculated the dipoles. The rose diagrams generated using the angular separation between the simulated lifetime dipoles and cells' original displacement directions were omnidirectional, indicating that

the control analyses had no preference for the correct direction (Fig. 4.3D). We also found that clathrin coat distribution is significantly heterogeneous even when the net cellular displacement is due to slight asymmetry of the spreading. Initiation and dissolution densities are the lowest within cellular regions with the highest extension rate (Fig. 4.3E).

Note: In the preceding paragraph, I cared for the cells and captured the movies, and Nathan Willy developed and implemented the methodology of lifetime dipole analysis.

Figure 4.3 Heterogeneous clathrin dynamics maps the tension gradient in protruding cells.

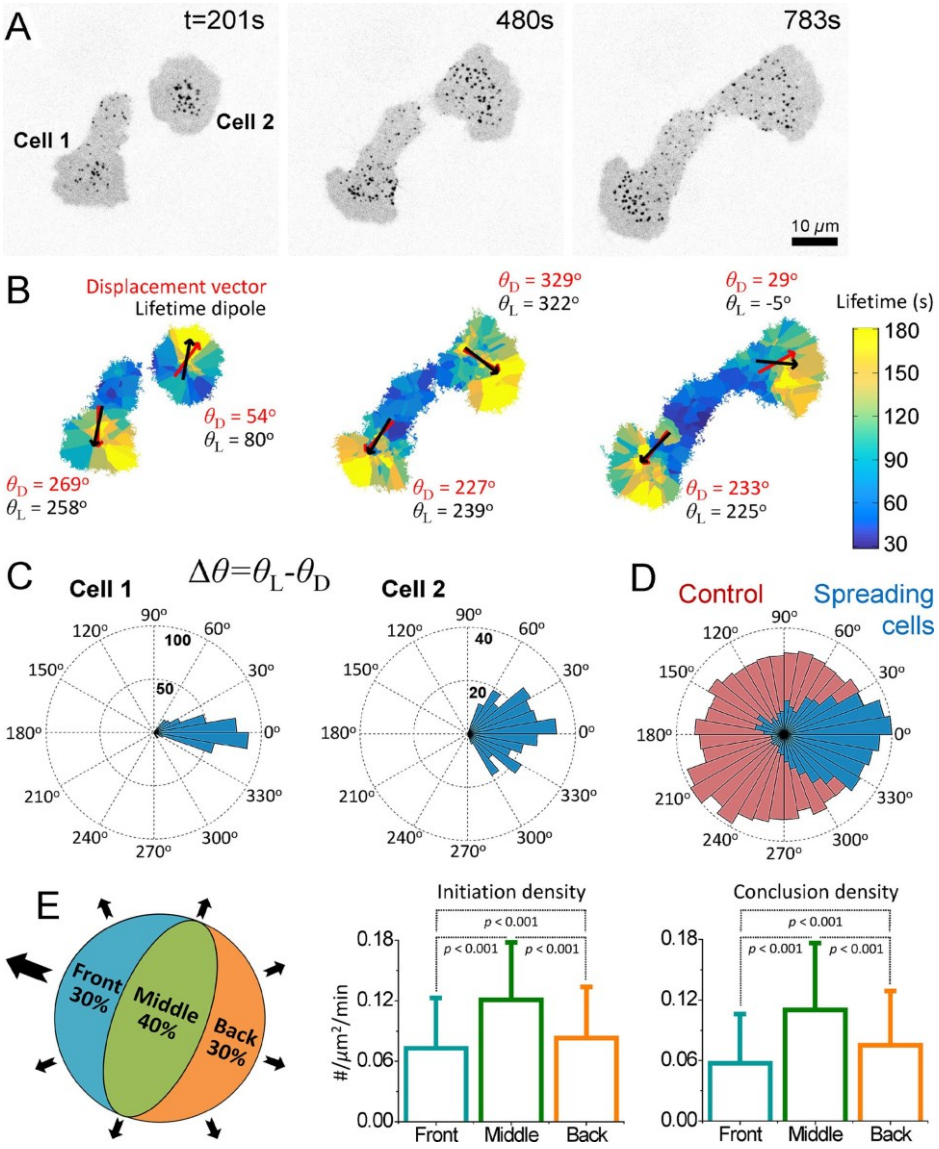

(A) Snapshots show two asymmetrically spreading BSC1 cells expressing AP2-EGFP. (B) Lifetime maps of the cells in A. This representation allows analyzing the local lifetime and density information by the color and size of the domains, respectively, that is, the domain sizes are inversely related to the local density of clathrin coats. The clathrin coat lifetime dipole moments are shown by black vectors for each cell. The displacement directions of the cellular centers of mass for the given frames are shown by red vectors. Θ_L and Θ_D represent the angles of the lifetime dipoles and displacement vectors, respectively. (C) Rose plots are assembled using the angular separation between the lifetime dipole vectors and the displacement vectors ($\Delta\Theta = \Theta_L - \Theta_D$) for the two spreading cells in A and B.

Continued

Figure 4.3: Continued

(D) The blue angular histogram shows $\Delta\Theta$ values obtained from 15 spreading cells (total spreading time is 123 min). The red histogram shows the cumulative result of five simulations (using the same 15 cells) in which Θ_L values are determined after clathrin coat lifetimes are randomly exchanged within a cell. (E) Asymmetrically spreading cells are sectioned into three regions (front: 30% of the cell area next to the leading edge; back: 30% of the cell area at the opposite side of the leading edge; middle: the remaining 40% of the cell area in between the front and back regions) in each frame of spreading movies. Both the front and back are extending regions. However, initiation and conclusion densities (shown as bar plots; mean + SD) are the lowest at the front region, which has the highest extension rate. p values were obtained using the two-tailed t test.

Tether force measurements revealed a significant front-to-rear tension gradient at the lamellipodial fragments of migrating keratocytes (Lieber et al., 2015). Such fragments cannot be isolated from migrating astrocytes for tension measurements. However, at the dorsal surface of these cells, we detected significant spatial heterogeneity in CME dynamics accompanying the expected tension gradient. Clathrin coats originating in the proximity of the leading edge have longer lifetimes (69 ± 51s [leading edge] vs. 58 ± 39s [lamella], $p < 0.001$; Fig. 4.4D) and narrower growth rate distributions (0.035 ± 0.003 [leading edge] vs. 0.041 ± 0.005 [lamella], $p < 0.02$; Fig. 4.4E). As a visualization tool for the spatial distribution of the clathrin dynamics, we generated growth rate maps in which each pixel is given the value of the SD of the growth rates detected in a circular neighborhood. In this representation, regions of the cell that have slower clathrin dynamics have smaller SD values (Fig. 4.4C). A comparative analysis of clathrin coat initiation and dissolution densities at the two regions is infeasible due to the complex three-dimensional (3D) geometries of the membrane ruffles appearing at the leading edge (Kural et al., 2015). Collectively, our results demonstrate that the cellular processes

associated with spatial divergences in plasma membrane tension increase the heterogeneity of CME in cells.

Note: For the following figure, Nathan Willy cared for the cells, captured the movies, and analyzed the data in sections A-E. Spencer Heidotting cared for the Drosophila and captured the movies found in F-J, while I performed the analysis. I developed the methodology of generating a map of the standard deviation of growth rates, but was inspired by the maps developed previously by Nathan Willy, which can be seen in Figure 4.3.

Figure 4.4 Heterogeneous CME during in vitro and in vivo cell migration.

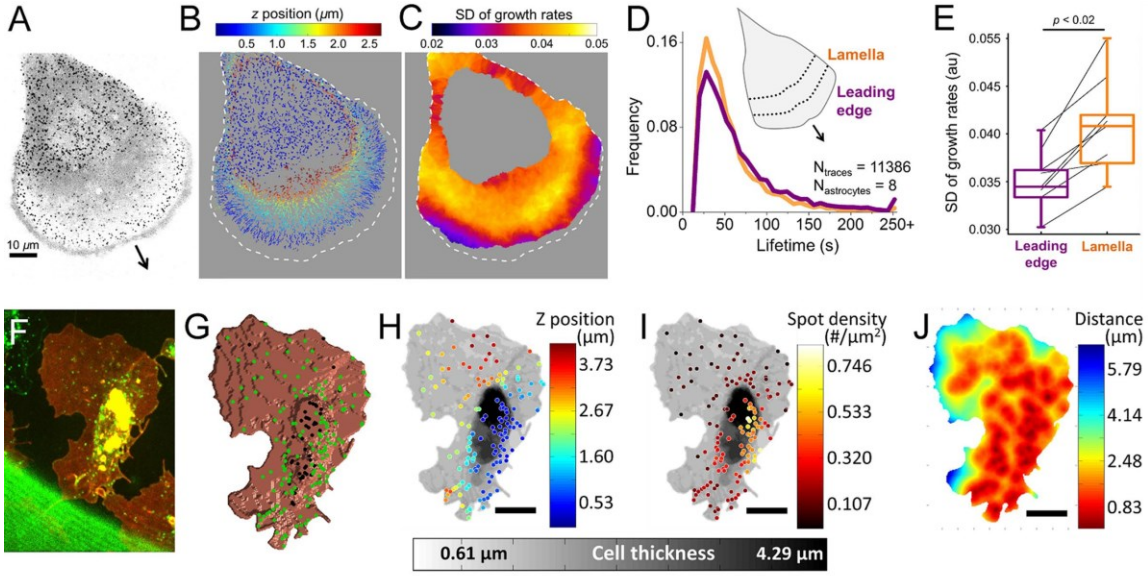

(A) Maximum z-projection image shows clathrin-coated structures at the ventral and dorsal surfaces of an U373 astrocyte expressing AP2-GFP. The arrow points toward the direction of extension. (B) Clathrin coat traces obtained from the cell in A are color-coded according to their z-position relative to the substrate. (C) Growth rate map of the dorsal surface is created by calculating the SD of clathrin growth rates within a 4.8-μm radius. SD values are lower in the vicinity of the leading edge due to slower clathrin dynamics. Dashed lines represent the cell boundary. (D) Normalized distributions show lifetimes of dorsal clathrin coats positioned within an 8-μm neighborhood of the leading edge (indigo) and the dorsal coats positioned in the lamellar region between 8 and 16 μm from the leading edge (orange). (E) Box plots show the SD of growth rate distributions assembled using the leading edge and lamellar clathrin coat populations from eight astrocytes (N_{traces} = 11,386). Connected lines indicate the values obtained from the same astrocyte. The narrower distribution obtained for the leading edge group (indigo) indicates slower clathrin dynamics at this region. Boxes extend to the quartiles, with a line at the median. Whiskers extend from the 10th to 90th percentiles. p value was obtained using the two-tailed t test. (F) Hemocytes expressing clathrin-GFP (green) and CD4-tdTomato (red) are imaged at the ventral surface of late Drosophila embryos. (G) CD4 signal is used to generate a 3D mask representing the surface of the hemocyte. Positions of the clathrin coats within 320-nm neighborhood of the surface are shown with green dots. (H, I) Grayscale represents the thickness of the hemocyte. Endocytic clathrin coats are color coded according to their z-positions in H and local density of clathrin spots calculated within a 5-μm cube in I. (J) Each pixel in the hemocyte image is color coded according to its average distance to the three closest clathrin coats. Scale bars in H–J are 8μm.

4.3.2 Spatiotemporal variations in clathrin dynamics of Drosophila embryos

We expect spatiotemporal heterogeneity in clathrin coat dynamics to be prominent during developmental processes associated with dynamic tissue mechanics. It was previously

shown that tension-based regulation of receptor endocytosis have important functions in development of Drosophila embryos (Pouille et al., 2009). Since quantification of clathrin lifetimes is error prone within tissue contexts, we used growth rates and spatial distribution of clathrin-coated structures to probe CME in this system (Chapter 2). During late stages of Drosophila embryogenesis, hemocytes migrate along the ventral nerve cord to populate the entire embryo. Unlike in vitro migration systems, embryonic hemocytes are physically constrained by the 3D environment and therefore do not form membrane ruffles at their lamellipodial extensions (Tucker et al., 2011). Figure 4.4F shows the maximum z-projection image of a hemocyte expressing fluorescently tagged clathrin and CD4 (membrane marker). We assessed the 3D positions of clathrin structures to distinguish the endocytic coats, which are in the vicinity of the cell surface (Fig. 4.4, G and H; Kural et al., 2012), and used alternative visualization tools to analyze the spatial distribution of endocytic clathrin coats. In Figure 4.4I, positions of endocytic clathrin coats are color coded according to the density of neighboring coats within the 5-μm neighborhood. In Figure 4.4J, the heat map shows each pixel's average distance to the three closest clathrin coats. Both representations illustrate that the density of endocytic clathrin coats are the lowest at the thin lamellipodial extensions of hemocytes (Fig. 4.4K).

During dorsal closure of the Drosophila embryo, tension on the amnioserosa (AS) tissue increases and the tissue volume reduces gradually (Ma et al., 2009; Saias et al., 2015). As expected, we detected significant reduction in clathrin dynamics at later stages of the dorsal closure (SD: 0.036 ± 0.003 [early] vs. 0.032 ± 0.002 [late], $p < 0.01$; Fig.

4.5A). Using SD maps, we also discovered that CME dynamics is spatially heterogeneous at the dorsal surface of the embryo (Fig. 4.5, B and D). The growth rate analysis revealed that clathrin dynamics are markedly slower at the AS compared with the two flanks of the lateral epidermis (LE) tissue (SD: 0.032 ± 0.002 [AS] vs. 0.035 ± 0.002 [LE], $p < 0.02$; Fig. 4.5C). Such a divergence in endocytic dynamics was anticipated, considering the distinct physical properties of AS and LE cells and the mechanical roles they play during dorsal closure (Brodland et al., 2014; Ducuing and Vincent, 2016; Pasakarnis et al., 2016).

Note: In the following figure, Drosophila were cared for and imaged by Spencer Heidotting, while I performed the analysis.

Figure 4.5 Spatiotemporal variations in clathrin dynamics can be detected within tissues of Drosophila embryo.

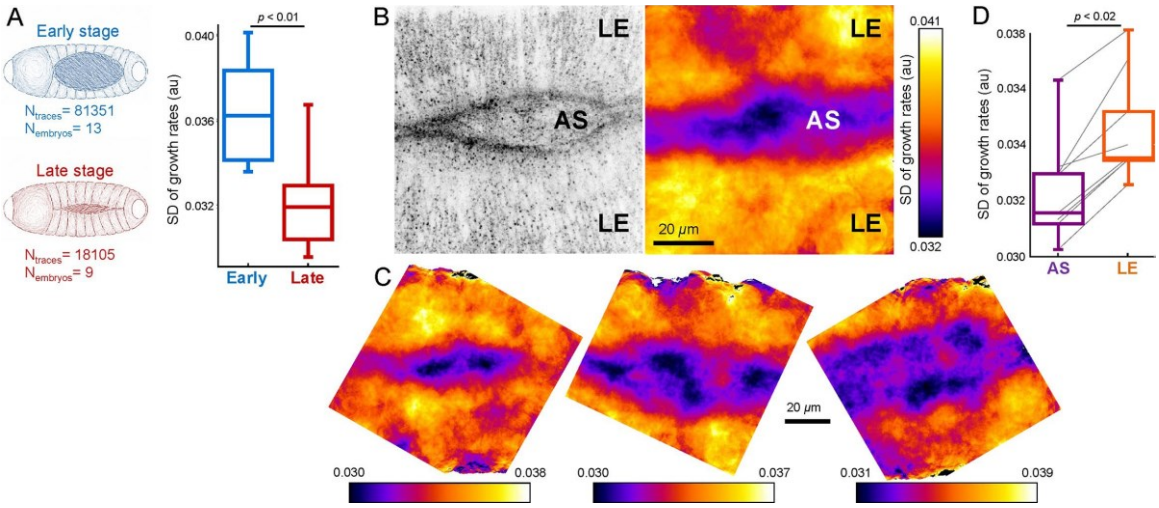

(A) Clathrin dynamics slow down with increasing tension during late stages of the dorsal closure. Box plots show the SD of clathrin growth rate distributions obtained from early and late stage AS tissues. Reduced SD is a hallmark of slowed-down endocytosis (Chapter 2). (B) Left, clathrin-coated structures at the dorsal surface of a Drosophila embryo. AS appears as narrow opening between the two flanks of lateral epidermis (LE). Right, SD map of the clathrin growth rates obtained from the same area. The map is created by calculating the SD of apical clathrin growth rates within an 8-µm radius. Lower SD values in the AS region display slower clathrin dynamics with respect to the neighboring LE. (C) More examples demonstrating the heterogeneous clathrin dynamics at the dorsal surface of late Drosophila embryos. (D) Box plots show the SD of clathrin growth rate distributions obtained from LE and AS of eight embryos. Connected lines indicate the values obtained from the same embryo. Boxes extend to the quartiles, with a line at the median. Whiskers extend from the 10th to 90th percentiles. p-values were obtained using the two-tailed t-test.

4.4 Discussion

We show that spatial and temporal variations in cell membrane tension dominate the dynamics of clathrin-coated structures. Endocytic machinery must overcome the major constituents of the effective membrane tension, that is, in-plane tension and membrane-cytoskeleton adhesion, to deform the plasma membrane (Sheetz, 2001). In-plane tension is assumed to be in equilibrium across the entire plasma membrane due to fast flow of membrane lipids. However, membrane-cytoskeleton adhesion can be heterogeneous and

induce stark differences in the clathrin dynamics between distinct surfaces of a cell (Dai and Sheetz, 1999; Boulant et al., 2011). Similarly, adhesion to the substrate can inhibit curvature formation and slow down clathrin coat dynamics locally. Therefore, non-uniform adhesion of a cell to the substrate creates another layer of heterogeneity in clathrin dynamics (Batchelder and Yarar, 2010; Chapter 2).

We believe that spatiotemporal heterogeneity in clathrin coat dynamics plays important roles in central cellular processes. Mechanoinhibition of endocytosis at early stages of cell spreading might elevate the rate of extension of the plasma membrane area (Gauthier et al., 2009, 2011). Inhibition of endocytosis at the leading edge of migrating cells may facilitate cell protrusion by allowing net membrane deposition to this region (Bretscher, 2014). Similarly, increased tension at the amnioserosa tissue of developing embryos may account for the gradual reduction of the cell volume through inhibition of endocytosis in the late stages of the dorsal closure. Future studies should be directed toward investigating the mechanoregulation of endocytosis in vivo and elucidating the roles it plays at the organismal level.

4.5 Materials and Methods

4.5.1 Cell culture and fluorescence microscopy

BSC1 and U373 cells stably expressing σ2-EGFP were cultured in DMEM (Life Technologies) containing penicillin/streptomycin and 10% fetal bovine serum (FBS). Gene-edited SUM159 cells were grown in F-12 medium containing 5% FBS and 1 μm/ml hydrocortisone (Aguet et al., 2016). Live cells and embryos were imaged using a

Nikon Eclipse (TI-E) microscope equipped with a 100× objective lens (Nikon CFI Plan-Apochromat Lambda, NA 1.45), a CSU-W1 spinning disk confocal head (Yokogawa Electric Corporation) and an electron-multiplying charge-coupled device (EMCCD) camera (iXon DU897 Ultra; Andor Technology). Sample temperature and z-position were stabilized using a temperature controlled chamber and perfect focusing system (PFS), respectively. NIS Elements software was used for image acquisition.

Spreading cells were imaged on glass bottom dishes (Greiner Bio-One) directly after plating. The plating time prior to astrocyte migration experiments was 8–24 h. Live cell imaging was performed at 37°C ambient temperature within L15 (Thermo Fisher Scientific) supplemented with 10% FBS. Images were acquired at 0.25–0.5 Hz, and laser exposure lasted for 50–300 ms per frame. The final concentrations of MβCD and deoxycholic acid (Sigma-Aldrich) were 10 and 0.4 mM in serum-free L15, respectively. Hypotonic shock was performed using 1:5 dilution of the imaging medium using deionized water. In the figures and movies fluorescence acquisitions were inverted to increase visibility.

4.5.2 Fly strains and in vivo imaging

Note: Drosophila care and imaging performed by Spencer Heidotting.

We used the UAS/GAL4 system to monitor clathrin dynamics in Drosophila embryos. Arm-GAL4, CLC-GFP, and CD4-tdTom strains were provided by the Bloomington Drosophila Stock Center. srpHemo-GAL4 was a gift from Norbert Perrimon (Harvard Medical School). Embryos were collected and aged for 11–13 h at 25°C. After

dechorionation, embryos were mounted on coverslips and immersed in halocarbon oil. Clathrin dynamics at the dorsal and ventral surfaces were imaged at 22°C using 3D time-lapse acquisitions. In amnioserosa, apical clathrin coats were determined by filtering out the bright puncta corresponding to organelle-bound clathrin-coated structures as described earlier (Chapter 2). In Figure 4.5A, maximum amnioserosa openings for the early- and late-stage embryos were 81.5 ± 13.0 and 28.2 ± 10.6 μm, respectively.

To analyze hemocyte images, clathrin coats were found using a simple threshold of the clathrin channel and localized using the center of intensity of the fluorescence signal (Kural et al., 2012). Similarly, the membrane was identified using a threshold on the CD4 channel. Using the built-in MATLAB function, isosurface, a triangular mesh of the membrane surface was generated. Clathrin coats were defined to be endocytic if they were < 320 nm from the nearest surface voxel. The spot density was determined by counting all endocytic coats around a spot within a 5-μm cube and then dividing that by the sum of the area from the triangulated mesh found within the cube. The distance map was generated by determining the average distance of the three closest endocytic clathrin spots for each pixel on the surface.

4.5.3 Two-dimensional tracking of clathrin-coated structures

We used cmeAnalysis software for 2D single particle tracking (Aguet et al., 2013). We used a previously developed trace rejection scheme to filter traces that do not follow a characteristic clathrin coat intensity profile (Chapter 2). We used the traces that pass the

rejection scheme in the calculation of lifetime distributions, growth rate distributions, initiation/dissolution densities and lifetime dipoles.

To determine the temporal evolution of the average clathrin coat lifetime, for each frame of a movie, we added together the lifetime of each trace that exists in that frame and divided by the number of traces considered.

4.5.4 Three-dimensional tracking of clathrin-coated structures

We used the z-position information to distinguish the dorsal and ventral clathrin coats in cells (Figures 1C, 2G, and 4B). cmeAnalysis software was used to analyze each z-plane of 3D time-lapse movies (followed by the trace rejection scheme detailed above). The resulting data were combined to link traces which occur at the same lateral position in two adjacent z-planes. Coincident traces had to remain within one pixel (160 nm) x–y distance for at least three frames. The resulting trace was assigned the maximum intensity value among all traces considered for combination. Axial positions were calculated using the intensity-weighted mean z-position of all traces considered. The algorithm for trace combination ran from the outermost z-planes to the innermost, alternating between the top and the bottom to ensure that there was no directional bias and all possible trace combinations were considered. See Appendix B for additional details.

4.5.5 Growth rate distributions

Clathrin coat intensity traces were normalized by subtracting a global minimum and dividing by the resulting maximum. From this normalized trace, each 12-s interval was used in a least-squares fit to determine the growth rate of each interval. A trace had to be

at least 12 s long to be included in the distribution. An arbitrary bin width (0.03) was found to delineate five distinct growth phases (fast dissolution, slow dissolution, plateau, slow formation, and fast formation) (Chapter 2).

To determine the SD of the growth rates per frame, we generated a list of the intensity slope of each trace within that frame and took the SD of that list. When the data were sparse, we used the walking average of three adjacent frames. We used PFS to eliminate sample defocusing triggered by the squeezing procedure. We found that the adjustment of the PFS resulted in a single frame of artificial growth rate values due to abrupt changes in the clathrin coat fluorescence intensities. Those frames were excluded from the analyses.

SD maps of clathrin coat growth rates in Figures 4.4 and 4.5 were made by, for each pixel within the cell, calculating the SD of all growth rates within 4.8 and 8 μm, respectively.

4.5.6 Lifetime maps and dipole vectors

Note: Developed by Nathan Willy.

Lifetime maps in Figure 4.3 were made of a given frame by calculating the average lifetime of the three closest clathrin-coated structures for each pixel within the cell. Patches of color were regions where the set of closest clathrin coats were the same, so color is an indication of local lifetime and the size of the patch is an indication of local clathrin coat density (larger patches indicates lower density).

Lifetime dipoles were calculated using the equation $\sum_{i=1}^{N}(T_i - \bar{T})\, r_i$, where T_i and r_i are the lifetime and the position of the ith clathrin-coated structure and $\bar{T}$ is the average lifetime of all clathrin-coated structures in the frame. Abortive clathrin coats with lifetimes less than 20 s, hotspots, and clathrin-coated plaques that do not disappear until the end of the acquisitions were excluded from the calculation of lifetime dipoles. In the randomization scheme used for the control analyses, the positions of clathrin-coated structures remained untouched to validate that the reciprocity between the lifetime dipole and cell displacement was due only to the spatial distribution of lifetimes within the cell.

4.5.7 Tether force measurements

Note: Performed by Scott Huber.

We used optically trapped beads to quantify membrane tether forces. An optical tweezers system was built based on a previous design; however; only one of the two traps was used in this application (Bustamante et al., 2009). Polystyrene beads (1 μm; Spherotech) were coated with fibronectin (Sigma-Aldrich) before the experiments. Cells were incubated for 10 min or 2 h before the experiments for measuring membrane tension at different stages of spreading. Membrane tension values (T) are calculated using $T = F_T^2/8\pi^2 B$, where F_T is the measured membrane tether forces and B is the bending modulus of the plasma membrane, and the value was assumed to be 0.27 pN μm (Hochmuth et al., 1996).

4.7 Acknowledgements

We thank Steeve Boulant, Tomas Kirchhausen, and Norbert Perrimon for the cell and fly lines.

Chapter 5 Curvature Generation by Endocytic Clathrin Coats

Derived from a manuscript in submission by: Ferguson, JP, Cakez, C, Hasan, F, Chang, H, Li, D, Betzig, E, Cocucci, E, and Kural, C.

In this chapter my contributions are development of tracking software; some tracking; and analysis of all results of tracking, including interpolation of values to generate trace-aligned averages, interpolation of images to generate radial kymographs, and compartmentalization of structures into area deciles.

5.1 Abstract

Sculpting a flat patch of membrane into an endocytic vesicle requires curvature formation on the cell surface, which is the primary function of endocytic protein complexes. The mechanism through which membrane curvature is imposed during formation of clathrin-coated vesicles is an ongoing controversy. Using super-resolved live cell fluorescence imaging, we demonstrate that curvature generation by clathrin-coated pits can be detected in real time within cultured cells and tissues of developing metazoan organisms. We found that the footprint of clathrin coats increase monotonically until the formation of curved pits. These findings rule out the possibility of an abrupt flat-to-curved transition

during late stages of clathrin-coated pit formation. Therefore, curvature generation by clathrin coats does not necessitate a dynamically unstable clathrin lattice.

5.2 Introduction

Clathrin-mediated endocytosis is the most extensively studied internalization mechanism of membrane lipids and proteins from the cell surface (Connor and Schmid, 2003). Over the past decades, a multitude of biophysical and biochemical methodologies have been employed to elucidate structural and dynamic properties of endocytic clathrin coats (Robinson, 2015). However, fundamental aspects of clathrin-mediated endocytosis remain controversial due to the lack of experimental approaches that allow correlation of ultra-structural and dynamic properties of clathrin-coated structures. Clathrin triskelions can assemble into coats (polyhedral cages and lattices) in a seemingly infinite number of geometries upon their recruitment to the plasma membrane by AP2, the main endocytic clathrin adaptor (Heuser, 1980; Heuser, 1989). Regardless of shape and size, formation of endocytic vesicles require curvature generation during the lifespan of clathrin coats. However, how and at what point of its growth a clathrin coat develops curvature has been a matter of debate for almost four decades (Kirchhausen, 1993; Kirchhausen, 2009; Lampe, Vassilopoulos, and Merrifield, 2016).

Currently, there are two competing models as to how clathrin and its accessory proteins generate curvature. Based on electron micrographs, it was originally proposed that clathrin initially grows into a flat array on the plasma membrane prior to transitioning into a curved coat (Heuser, 1980; Larkin, Donzell, and Anderson, 1986)

(Fig. 4.1A, top). This flat growth is postulated to reach 70-100% of the final surface area before remodeling into a clathrin-coated pit through transformation of the hexagonal clathrin lattice into a curved polyhedron with pentagonal and hexagonal faces (Heuser, 1980; Avinoam et al., 2015; Bucher et al., 2018). Eventually, 12 pentagonal faces must be introduced to the coat to generate a closed clathrin cage (Shraiman, 1997; Musacchio et al., 1999) (Fig. 4.1B). This model was rejected by others because insertion of even a single pentagonal face into a hexagonal lattice requires a substantial structural rearrangement, which is energetically unfavorable (Kirchhausen, 1993; Kirchhausen, 2009). As an alternative, it is suggested that clathrin-coated pits can form gradually without major structural rearrangement. According to this model, as clathrin triskelions are integrated into the coat, they organize into pentagonal as well as hexagonal faces to generate a fixed amount of curvature (Fig. 4.1A, bottom). This is motivated by classification of clathrin-coated structures into two categories: spherical, productive pits versus flat and less productive plaques; and each category has a distinct internalization mechanism (Kirchhausen, 2009; Saffarian, Cocucci, and Kirchhausen, 2009). The debate regarding curvature formation by clathrin pits has been recently rekindled by studies employing correlative fluorescence and electron microscopy of clathrin-coated structures (Lampe, Vassilopoulos, and Merrifield, 2016; Avinoam et al., 2015; Bucher et al., 2018).

Figure 5.1 Flat-to-curved transition necessitates a major change in the projected area of clathrin coats.

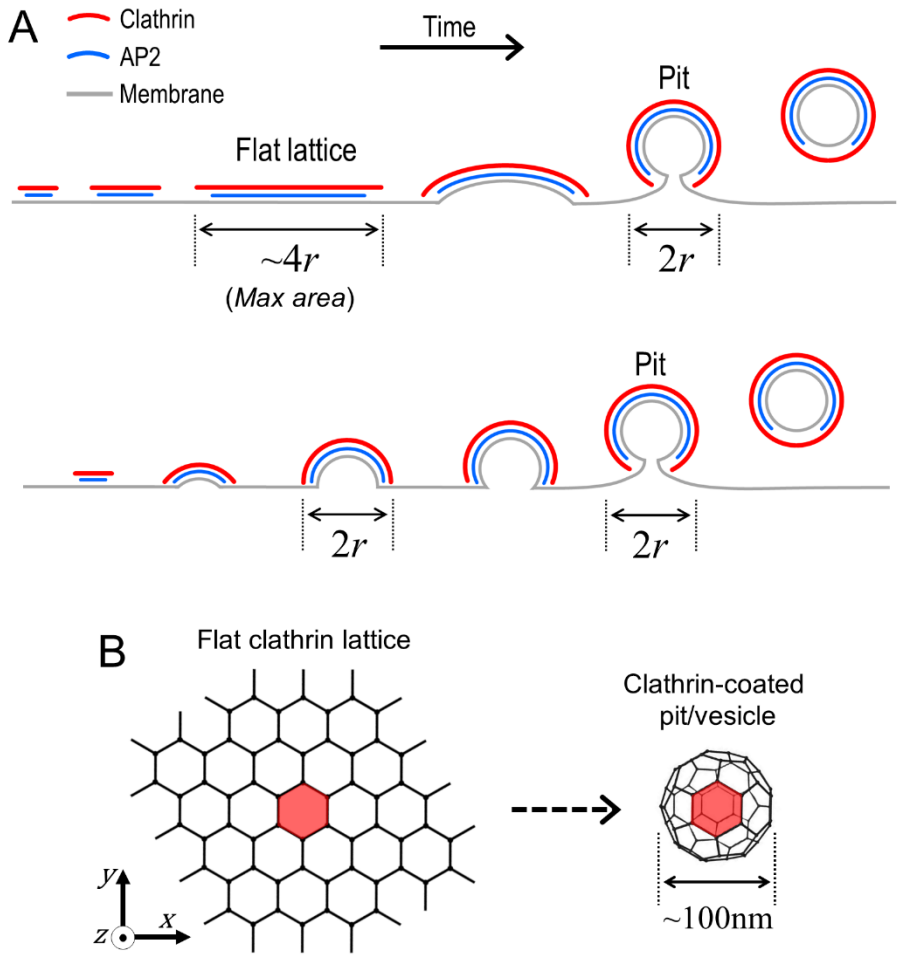

(A) Schematics depicting the cross-sections of clathrin coats as suggested by prevalent curvature generation models. According to the flat-to-curved transition models (upper), clathrin coats initially grows into a flat hexagonal lattice constituting 70-100% of the final surface area of the coated vesicle ($4\pi r^2$; r is the radius of the pit/vesicle). A disc-shaped, flat clathrin lattice is anticipated to reach a diameter of 3-4r prior to the transition into a pit (Heuser; 1989; Avinoam et al., 2015; Bucher et al., 2018). Upon this transition, the projected area reduces to πr^2. The constant curvature model (lower) predicts a gradual increase in the projected area until the diameter reaches 2r, which is also the diameter of the clathrin pit/vesicle. (B) To illustrate the extent of the projected area change upon a flat-to-curved transition, 60 triskelions are organized into a flat hexagonal lattice (left) and a buckyball-shaped cage containing 12 pentagons and 20 hexagons (right). A hexagon is highlighted with red in each image to aid comparison.

5.3 Results

One of the major observables that distinguish the two models is the change in the projected area (i.e., footprint) of the clathrin coat as it gains curvature. While the constant curvature model predicts a steady rise in the projected area of the coat, the flat-to-curved transition requires an abrupt ~3-4 fold reduction in the same measure (Fig. 5.1B; also see Fig. 6 of Heuser (1980) and Fig. 1 of Bucher et al. (2018)). Electron microscopy provides high-resolution snapshots of clathrin-coated structures at different curvature levels (Heuser, 1980; Avinoam et al., 2015; Bucher et al., 2018; Sochacki et al., 2017). However, due to the lack of temporal dimension, electron micrographs fail to provide direct evidence for the mechanism of clathrin-driven curvature generation. Conventional live cell fluorescence imaging allows researchers to elucidate the formation and dissolution dynamics of endocytic clathrin-coated structures (Kural and Kirchhausen, 2012; Chapter 2; Auget et al., 2013). However, in these studies structural properties of clathrin coats are obscured by the diffraction of fluorescence, which limits the spatial resolution. Under super-resolved fluorescence live cell imaging, clathrin-coated pits appear as a ring pattern, which correspond to a two-dimensional projection of a spheroid clathrin coat, i.e. clathrin-coated pit (Bates et al., 2007; Fiolka et al., 2012; Li et al., 2015). We employed TIRF-SIM (total internal reflection fluorescence structured illumination microscopy) to image the formation of clathrin-coated pits in cultured cells (in vitro) and tissues of developing Drosophila melanogaster embryos (in vivo) with high

Figure 5.2 TIRF-SIM allows analysis of clathrin-coated pit formation in cultured cells and in tissues of Drosophila embryos with high spatiotemporal resolution.

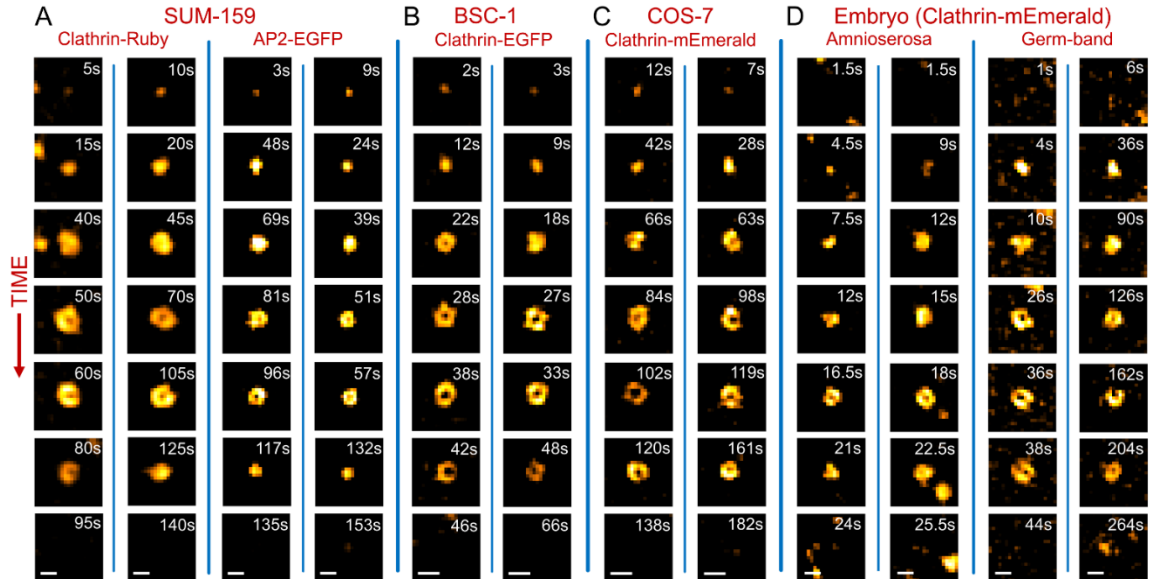

Each column shows snapshots from individual clathrin-coated pit traces. Formation of pits (marked by a ring pattern) can be observed under various in vivo and in situ conditions including SUM159 cells expressing clathrin-Ruby and AP2-EGFP as endocytic markers (A), BSC-1 cells expressing clathrin-EGFP (B), COS-7 cells expressing clathrin-mEmerald (C), and amnioresora and germ-band tissues of Drosophila embryos expressing clathrin-mEmerald (D). Two traces are shown for each condition. Scale bars, 200 nm.

spatial and temporal resolution and monitor curvature generation in real time (Li et al., 2015) (Fig. 5.2).

Automated tracking of clathrin-coated structures captured in conventional fluorescence microscopy assays is predicated on locating diffraction-limited spots represented by the point-spread function (PSF) of the imaging system (Chapter 2; Auget et al., 2013; Miller et al., 2015). This PSF is often approximated with a two-dimensional Guassian function to determine the position and fluorescence intensity of the spot. However, high-resolution clathrin coat images generated using TIRF-SIM often cannot be approximated as a Gaussian function due to the ring pattern that marks formation of

the clathrin pit. To circumvent this, we developed a custom tracking software for manual selection of clathrin-coated pit traces that fit highly restrictive criteria: Selected traces must appear independent of other structures from their formation to dissolution, and must contain a single phase of fluorescence growth followed by a single decline. We found that these criteria reject ~90% of the traces that would be selected as clathrin-coated pits by our standard tracking algorithm. We excluded the rejected traces from further analysis.

TIRF-SIM acquisitions under various in vitro and in vivo conditions revealed that the projected area of clathrin-coated pits increase monotonically until the ring pattern arises, which is followed by a relatively fast disappearance of fluorescence due to uncoating (Fig. 5.2). To perform a bulk analysis, we created the time average of clathrin-coated pit traces extracted from BSC-1 and COS-7 cells imaged with high-NA TIRF-SIM and calculated the temporal evolution of the projected area using an edge-finding algorithm (Fig. 5.3A). Contrary to the predictions of the flat-to-curved transition models, we detected no decrease in the footprint of the coat prior to appearance of the ring pattern. Instead, we found that the ring pattern is observable as the projected area makes a plateau and reaches the maximum (Fig. 5.3A, B). The radii of the ring patterns obtained in this way are in good agreement with the previous reports on the average size of clathrin-coated pits (Heuser 1980; Avinoam et al., 2015; Bucher et al., 2018; Sochacki et al., 2017; Miller et al., 2015).

Figure 5.3 Clathrin coats reach maximum projected area by formation of pits.

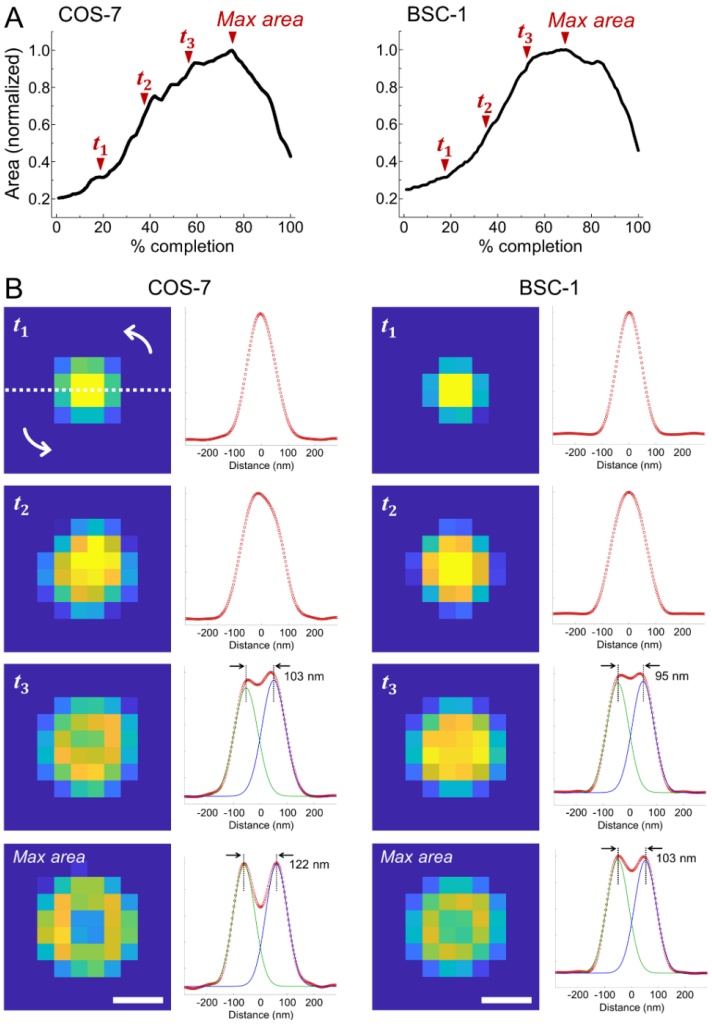

(A) We obtained average clathrin-coated pit formation and dissolution images using 34 and 81 individual traces obtained from COS-7 cells expressing clathrin-mEmerald and BSC-1 cells expressing clathrin-EGFP, respectively. In both cases, the area of the average image increases monotonically until a plateau is reached, which is followed by a relatively sharp decrease. (B) Average images are shown for four equally spaced % completion points, last of which is the maximum area point (denoted as t1, t2, t3 and max area in A). The ring pattern appears as the area converges to the maximum. Next to each image is the radial average (red circles), which is obtained along a cross-section rotated 180° around the center (Fig. 5.9). We determined the ring size by fitting two Gaussian functions (green and blue) to the radial average and calculating the peak-to-peak separation. The average ring diameters reach up to 122 nm and 103 nm for COS-7 and BSC-1 cells, respectively. Scale bars, 90 nm.

Figure 5.4 Clathrin-coated pits have the maximum footprint.

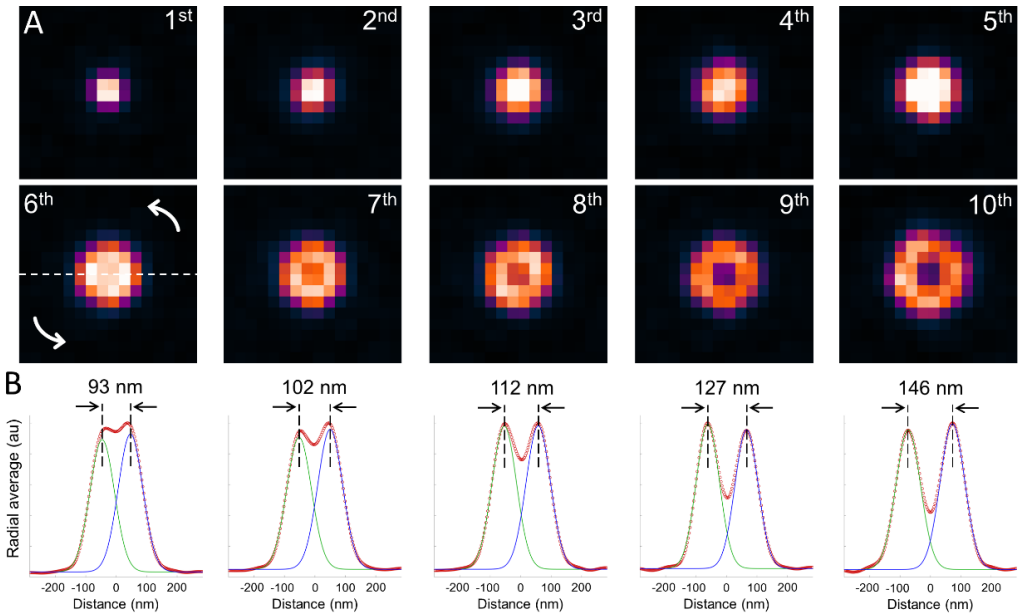

(A) Using clathrin-coated pit traces extracted from COS-7 cells expressing clathrin-mEmerald, clathrin coat images are separated into 10 groups based on the projected area (1st being the smallest and 10th the largest area group; N_{images}= 889). The ring pattern is the most apparent in the largest area (the 10th) group. (B) The radial average of the largest 5 groups in (A) are plotted and Gaussian fits are used to quantify the ring size. (C) The average of the largest area groups are shown for clathrin coat images extracted from BSC-1 cells expressing clathrin-EGFP (N_{images}=1409), SUM-159 cells expressing clathrin-Ruby (N_{images}=1786) and AP2-EGFP (N_{images}=18718) and Drosophila embryos expressing clathrin-mEmerald (N_{images}=1264). In the bottom panel, ring sizes are determined as explained in B.

Flat-to-curved transition models propose that the clathrin coat is flat when the maximum projected area is reached (Fig. 5.1). In contrast to this prediction, when images constituting clathrin-coated pit traces are grouped based on their projected area (Fig. 5.4), we found that the ring pattern is the most apparent in the average images obtained from the largest area decile (Fig. 5.5). The fact that clathrin-coated pits populate the largest area decile show that there exist no flat intermediate state with a greater projected area.

Figure 5.5 Average of all images in a decile.

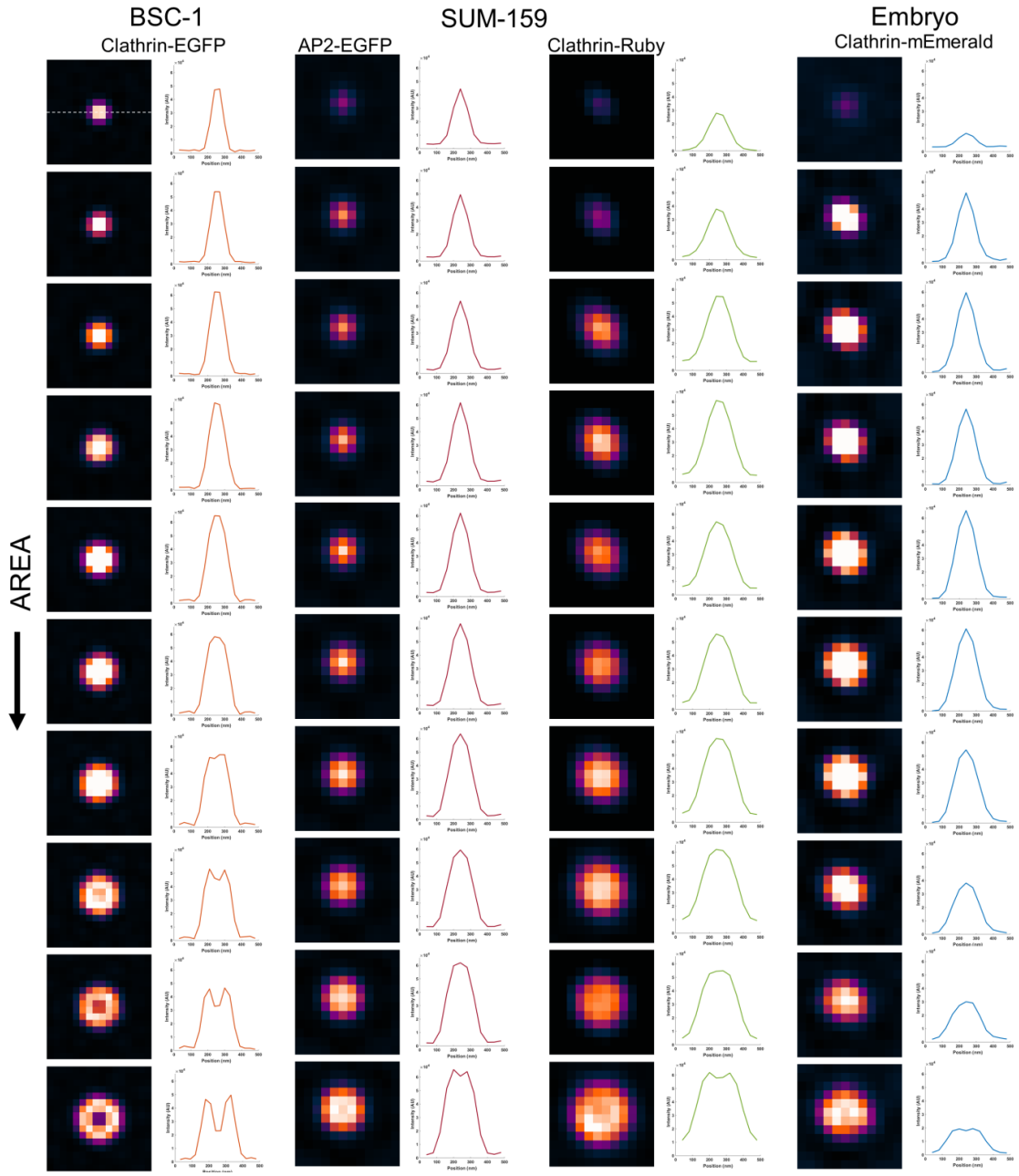

For each condition, average images of different area groups are ranked from smallest (top) to largest (bottom). Intensity along the cross-section is plotted next to each image.

5.4 Discussion

These results clearly demonstrate that curvature generation by clathrin-coated pits takes place through a mechanism that is independent of a flat-to-curved transition as proposed by previous studies. The resolving power of TIRF-SIM (~90 nm; (Li et al., 2015)) is sufficient to detect the proposed 3-4 fold area reduction that results in a ~100 nm diameter clathrin-coated pit (Fig. 5.1B). If such a transition occurs, it has to be at very early stages of the coat formation (Scott et al., 2018). Note that we used very strict criteria to limit our analyses solely to clathrin-coated pits. We do not rule out the possibility of a flat-to-curved transition mechanism that is proposed to take place at the edges of large clathrin patches (i.e. plaques) (den Otter and Briels, 2011), which is out of the scope of this work.

Flat-to-curved transition of the clathrin coat requires a major structural reorganization that disrupts the hexagonal arrangement of the flat clathrin lattice (Kirchhausen, 1993). It has been proposed that a dynamically unstable clathrin coat can go through such transitions by allowing rapid exchange of clathrin triskelions. This assumption has been supported by fast fluorescence recovery rates detected after photobleaching of fluorescent clathrin spots in live cells. It is important to note that a majority of the fluorescent spots that appear as individual clathrin-coated structures under diffraction-limited imaging actually contain multiple independent structures that are positioned in close proximity (Fig. 5.6). Therefore, it is worthwhile to consider that the

Figure 5.6 Examples of rejected traces.

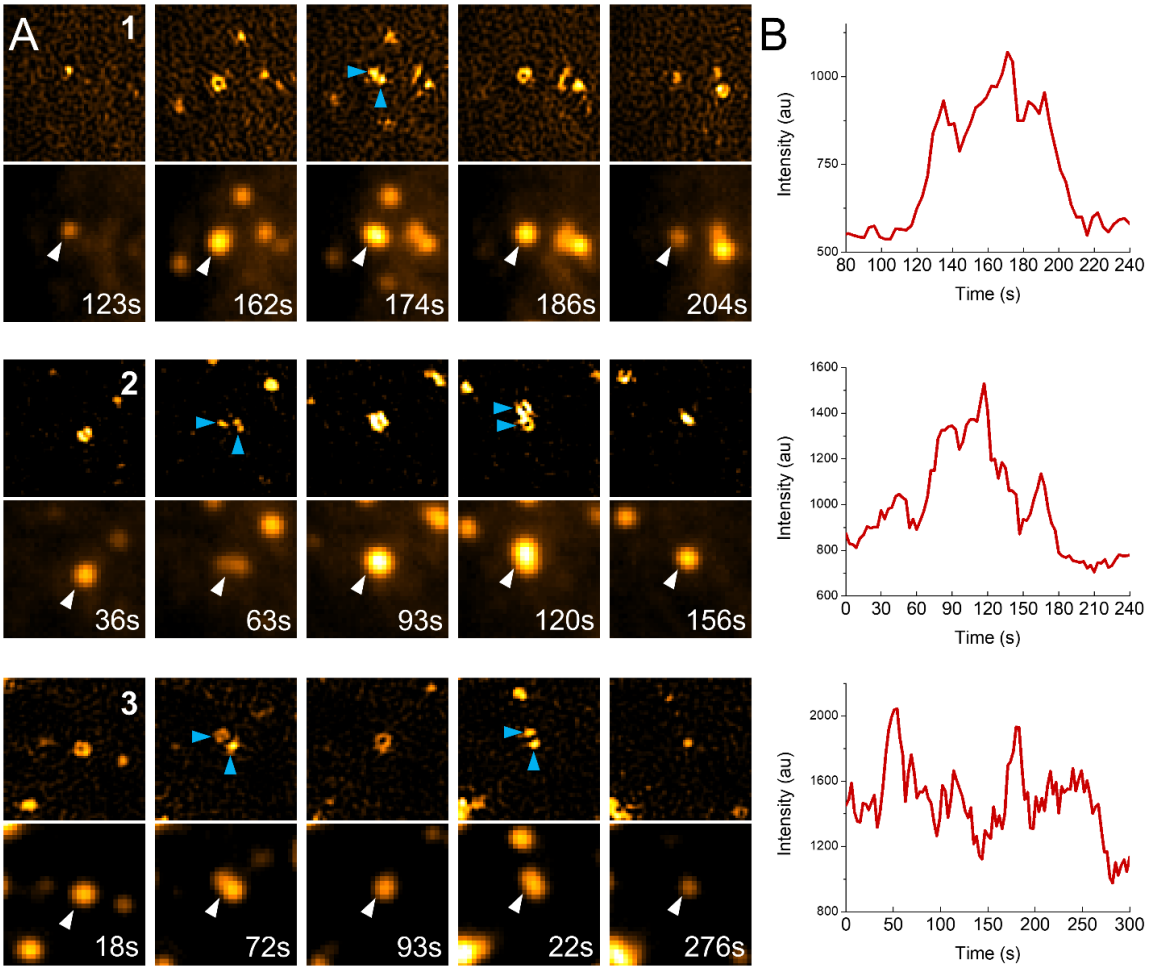

(A) Three examples of diffraction-limited fluorescent spots comprising multiple clathrin-coated structures. Top rows show TIRF-SIM snapshots, where blue arrowheads mark multiple structures in close proximity. Bottom rows show the diffraction-limited TIRF images of the spots (white arrowheads). (B) Plots show the fluorescence intensity traces of the diffraction-limited spots in (A).

detected fluorescence recovery may actually correspond to initiation of adjacent clathrin-coated structures.

We analyzed clathrin-coated pit formation with high spatiotemporal resolution in a wide range of cell types as well as, for the first time, tissues of a developing organism. Even though our findings are more compatible with the constant curvature model, we do

not rule out the possibility of a flat-to-curved transition at very early stages of clathrin coat formation (Scott et al., 2018), i.e. while the coat is smaller than the resolution limit of TIRF-SIM. We note that, theoretically, such a transition can take place without a substantial rearrangement of a hexagonal lattice by incorporating pentagonal faces predominantly at later stages of clathrin-coated pit formation (den Otter and Briels, 2011). Altogether, our results signify the importance of employing methodologies comprising high resolution in both spatial and temporal dimensions for constructing dynamic models.

5.5 Materials and Methods

5.5.1 Cell Culture

BSC-1 cells stably expressing EGFP-CLTA and COS-7 cells transiently expressing mEmerald-CLTB were cultured and prepared for microscopy as described in Li et al. (2015). SUM-159 cells genome edited to express σ2-EGFP (Auget et al., 2016) and transiently expressing mRuby-CLTB (Addgene; Plasmid #55852) were cultured in F-12 medium with hydrocortisone, penicillin-streptomycin and 5% fetal bovine serum (FBS). Gene Pulser Xcell electroporation system (Bio-Rad Laboratories, CA, USA) was used for transient transfection of SUM-159 cells following manufacturer's instructions. SUM-159 cells were cultured on 35mm glass bottom dishes (MatTek) and imaged 24-48 hours after transfection in phenol-red-free L15 (Thermo Fisher Sci.) supplemented with 5% FBS at 37°C ambient temperature.

5.5.2 Drosophila embryos

UAS-CLC-mEmerald flies were mated with a GAL4-Arm (Bloomington Drosophila Stock Center) line to produce embryos expressing CLC-mEmerald in the amnioserosa and surrounding germ-band tissue. The embryos were collected and aged for 10-12 hours at 25°C. After dechorionation, embryos were mounted on coverslips and immersed in voltalef oil for imaging at 22°C.

5.5.3 TIRF-SIM

High-NA TIRF-SIM images of COS-7 and BSC-1 cells were acquired with 1.7-NA 100x objective (Olympus Life Science, CA, USA) as described in Li et al. (2015). SUM-159 cells and Drosophila embryos were imaged using the TIRF-SIM system at the Advanced Imaging Center (AIC) of the Janelia Research Campus. This system comprises a 1.49-NA 100x objective lens (Olympus Life Science, CA, USA) fitted on an inverted microscope (Axio Observer; ZEISS) equipped with a sCMOS camera (ORCA-Flash4.0; Hamamatsu). Structured illumination was provided by a spatial light modulator as described in Li et al. (2015) and movies were acquired using 20ms exposure time and with frame rates ranging from 0.15 to 0.5 Hz. To image clathrin activity in tissues of Drosophila embryos, the apical surface of amnioserosa and germ-band cells were positioned within the evanescent field of the TIRF-SIM illumination by gently pressing the embryos against the coverslip.

5.5.4 Image Analysis

Clathrin-coated structures in the TIRF channel were tracked using two-dimensional cmeAnalysis software (Auget et al., 2013). The traces extracted this way were filtered based on their intensity profiles as described in Chapter 2. Briefly, to distinguish complete clathrin coat formation events, only the traces that contain both positive and negative intensity slopes (corresponding to coat growth and dissolution, respectively) were selected.

To analyze the images in the TIRF-SIM channel, a program was written in MATLAB 2017b (Mathworks) for the user to manually locate acceptable traces based on the following rejection criteria: 1) The structure must not come into contact with any other structure at any point during its lifetime (to exclude pair spots). 2) The structure must perform a single phase of intensity increase followed by a single phase of intensity decrease (to exclude hotspots). Once a structure was selected, the user defined the first and last frames of the structure's existence. The *x*-*y* position of the structure was taken as the intensity-weighted center of the image. The area was calculated using the MATLAB built-in function, edge, set to calculate the Canny edge of a small window containing only the structure of interest. When the edge finder failed to close the edge, the algorithm allowed the user to close the edge manually (Fig. 5.7). The area within the closed boundary is calculated as the sum of the pixels enclosed. Deciles were generated for each

Figure 5.7 User selection of incomplete edge finding.

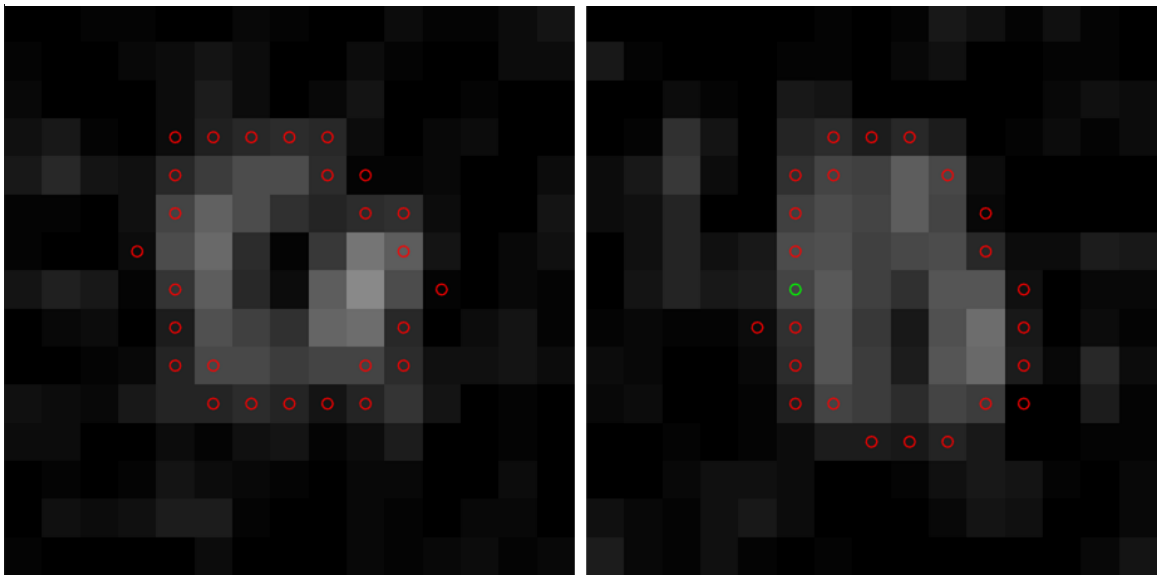

Red circles in each image correspond to the edges detected by the Canny edge-detection algorithm. The pixels within this boundary are used to define the designated area of the structure (left). When the Canny algorithm fails to close the boundary (right), the user has the option to manually assign the missing edge pixels (green circle).

sample type based on these area measurements. Decile averages are the pixel-by-pixel average of the images that fall into the respective area group.

Time averages of clathrin-coated pit traces are determined using high-NA TIRF-SIM images centered on the intensity-weighted center of the structure at each time point. These image sequences are of varying lengths, so each is extended to a length of 100 frames by linearly interpolating respective pixels at each time point (Fig. 5.8). Images corresponding to each time/completion point are averaged pixel-by-pixel to obtain the time averages. In each frame, the area is calculated using the Canny edge-detection algorithm as described above (Fig. 5.3A).

To get the radial averages shown in Figures 3 and 4, the images were upscaled by a factor of 10 with bicubic interpolation. For each upscaled image, 36 radial kymographs (separated by 5° increments and concentric with the intensity-weighted center of the structure; Fig. 5.9A) are averaged and fit to the sum of two Gaussian functions (Fig. 5.9B):

$$F = B + A_1 e^{-\frac{(x-x_1)^2}{2\sigma^2}} + A_2 e^{-\frac{(x-x_2)^2}{2\sigma^2}}$$

where B is the background, A_1 and A_2 are the amplitudes, x_1 and x_2 are the center points, and σ is the standard deviation. σ values for the largest area deciles are 40.6 nm for COS-7 Clathrin-mEmerald, 37.3 nm for BSC-1 Clathrin-EGFP, 68.7 nm for SUM-159 Clathrin-Ruby, 45.4 nm for SUM-159 AP2-EGFP and 51 nm for embryo Clathrin-mEmerald. As expected, the standard deviations are the smallest for the data sets obtained by high-NA TIRF-SIM (i.e. COS-7 and BSC-1) and the largest for the SUM-159 Clathrin-Ruby dataset due to longer fluorescence wavelength.

Figure 5.8 Demonstration of temporal interpolation.

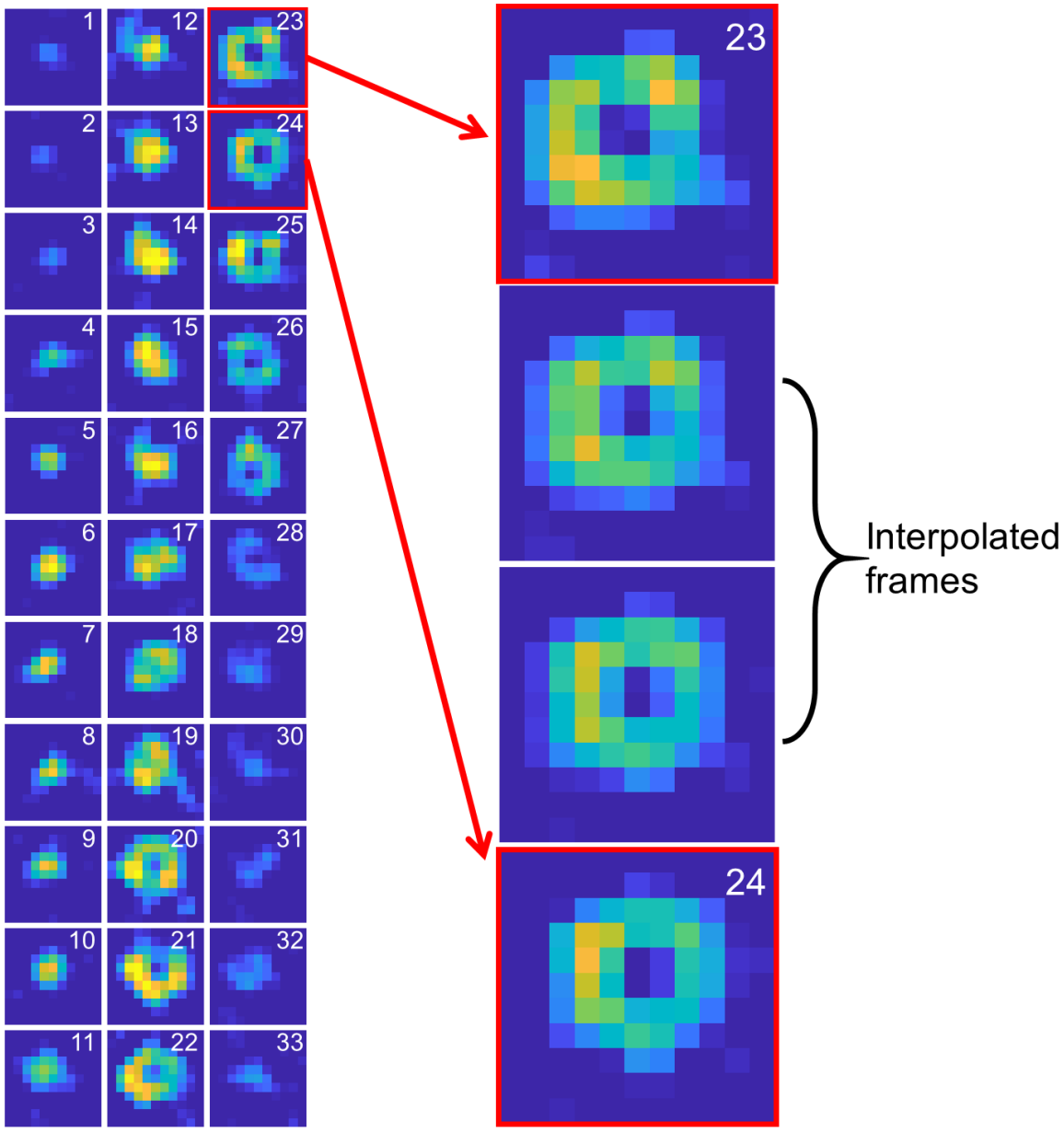

33 consecutive TIRF-SIM images corresponding to formation and dissolution of a clathrin-coated pit in a COS-7 cell expressing clathrin-mEmerald (left). Blowup image shows the linear interpolation linking frames number 23 and 24 (right).

Figure 5.9 Radial kymographs for each cell type.

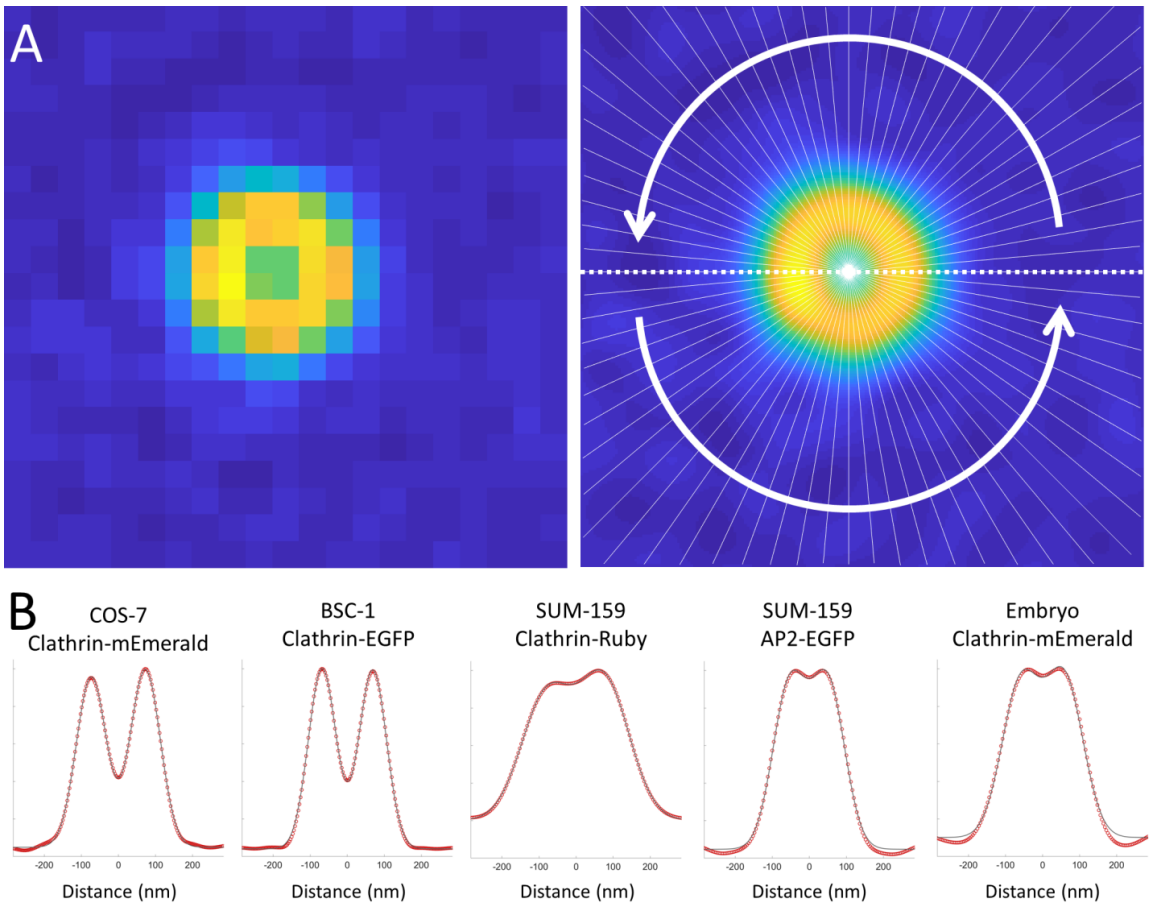

(A) An average clathrin-coated pit image (left) and its upscaled version (right). Kymographs are calculated along the radial white lines separated by 5°. (B) Radial averages are determined by averaging the radial kymographs in (A). Plots show the radial averages (red circles) of the largest area deciles for the conditions shown in Figure 5.5, where the gray line is the sum of the Gaussian fits.

5.7 Acknowledgements

We thank the Advanced Imaging Center, Janelia Research Campus for the support using high-temporal-resolution TIRF-SIM, in particular, the help from A. Taylor and S. Khuon. The Advanced Imaging Center is generously supported by the Gordon and Betty Foundation as well as the Howard Hughes Medical Institute.

Chapter 6 Conclusions and Future Work

We developed the state of the art in measurement of membrane tension using fluorescence microscopy to monitor the dynamics of CME. We developed growth rate analysis to perform real-time measurement of CME dynamics. We performed various mechanical alterations of the cell to induce changes in membrane tension while monitoring CME dynamics. These experiments have revealed a close link between membrane tension and CME. Utilizing this knowledge we achieved predictive models for tension-driven, natural cellular phenomena such as migration and spreading. These observations suggest that membrane tension must be continuously linked to CME dynamics via energy requirements of bending the membrane. Therefore, it is most likely that productive CCPs form under continuous curvature generation.

However, the challenge of isolating *productive* CCPs from the population of CCSs found on the membrane is daunting. The current state-of-the-art that we regularly utilize relies on statistical methods for locating and tracking objects of significance (Auget et al., 2012). In practice, we are confident that it locates all objects of significance in a fluorescent movie; however it also locates insignificant objects. Even then, only a subset of significant objects fit criteria that would compel us to consider them productive CCPs. In Chapter 5 we performed manual tracking to identify productive CCPs, but this

has cost us many hours of repetitive labor. As is the trend across many industries, it seems likely that machine learning could allow for an automated procedure to be developed. I believe machine learning is the only way to succeed in automated detection of productive CCPs, and it will be a valuable project for a future lab member to pursue.

If we were able to isolate productive CCPs in our analysis, that would eliminate a major source of noise. Electron microscopy has shown that clathrin also forms flat structures on the membrane surface (Avinoam et al., 2015). While the proportion of these structures might provide insight into membrane tension, such objects would provide little temporal information to a fluorescence-based tension measurement methodology.

An additional confounding factor to analysis are structures located closer together than the diffraction limit. Spinning-disk confocal microscopy is useful for minimizing out-of-focus light, but there are imaging methodologies that achieve spatial resolution beyond the diffraction limit. Many of these require an extreme reduction in temporal resolution, but one method shows promise for future use in our lab. Structured illumination microscopy (SIM) utilizes structured light to extract higher frequency information from the sample (Kner et al., 2009). In brief, light impinges upon the sample from multiple directions and in multiple phases, and this directionally distinct phase information generates interference that can be used to probe higher spatial frequencies. Experimentally, the improvements in resolution can be as great as 4-fold (Li et al., 2015). In Chapter 5 we used this to increase the information obtained from individual objects while meeting restrictive criteria, but SIM could also improve general detection, tracking,

and classification schemes. We expect to purchase or build a SIM system in our lab in the next few years.

In order to perform experiments using SIM sooner, we were accepted to the visiting scientist program at Howard Hughes Medical Institute's Janelia Research Campus. While there, we were able to perform total internal reflection fluorescence-(TIRF-) SIM, a form of SIM with a very high signal-to-noise ratio (this data was presented in Chapter 5). Additionally, we utilized their lattice light sheet microscope to obtain high-speed images of migrating hemocytes in drosophila embryos. A lattice light sheet microscope operates by illuminating the sample parallel to the field of view with a thin sheet of light, rather than perpendicular illumination with a scanned, focused point of light like in SDCM. The use of a sheet rather than a point reduces the power density of photonic exposure to the cells and allows for an increased rate of image capture. In our lab, we found that imaging hemocytes in live drosophila embryos resulted in rapid photobleaching and insufficient temporal resolution. However, we were able to capture this data at Janelia using a lattice light sheet microscope and the analysis will be the research of future students.

Hemocytes are an interesting cell type because they perform active migration very near to the surface of drosophila embryos. Migration is an interesting tension-mediated, natural phenomenon to which we can apply our analytical techniques. In Chapter 4 we demonstrated our ability to predict cell movement and analyzed stationary images of hemocytes. The data obtained at Janelia will enable the first study of membrane tension

in a migratory cell within a living organism. This is a crucial step in validating our hypothesis that CME dynamics are a useful indicator of membrane tension in living organisms.

CME is a tremendously heterogeneous process and there appear to be limits and variability in the range of response to tension modification, depending on cell type and environment. However, with advances in imaging and analytical techniques we have distilled information about the tension on the membrane, and even predicted the movement of a cell on a glass substrate. Future experiments will extend our knowledge into the natural environment of the cell, and reduce noise in our measurements. Complete knowledge of the membrane tension profile will provide insight to cellular interactions vital to the study of disease (Batta et al., 2018). CME is a particularly important process for neurons, which exchange neurotransmitters at a very fast rate (Loebrich, 2014). Our procedure is still insufficient for diagnostic work, but one day might enhance critical studies of disease development and progression.

Bibliography

Aegerter-Wilmsen, T., Heimlicher, M.B., Smith, A.C., de Reuille, P.B., Smith, R.S., Aegerter, C.M., and Basler, K. (2012). Integrating force-sensing and signaling pathways in a model for the regulation of wing imaginal disc size. Development 139, 3221–3231.

Aghamohammadzadeh, S., and Ayscough, K.R. (2009). Differential requirements for actin during yeast and mammalian endocytosis. Nat. Cell Biol. 11, 1039–1042.

Aguet, F., Antonescu, C.N., Mettlen, M., Schmid, S.L., and Danuser, G. (2013). Advances in analysis of low signal-to-noise images link dynamin and AP2 to the functions of an endocytic checkpoint. Dev. Cell 26, 279–291.

Aguet, F., Upadhyayula, S., Gaudin, R., Chou, Y., Cocucci, E., He, K., Chen, B.-C., Mosaliganti, K., Pasham, M., Skillern, W., et al. (2016). Membrane dynamics of dividing cells imaged by lattice light-sheet microscopy. Mol. Biol. Cell 27, 3418–3435.

Apodaca, G. (2002). Modulation of membrane traffic by mechanical stimuli. Am. J. Physiol. Renal Physiol. 282, F179–F190.

Avinoam, O., Schorb, M., Beese, C.J., Briggs, J.A.G., and Kaksonen, M. (2015). Endocytic sites mature by continuous bending and remodeling of the clathrin coat. Science (80-.). 348, 1369–1372.

Batchelder, E.M., and Yarar, D. (2010). Differential Requirements for Clathrin-dependent Endocytosis at Sites of Cell–Substrate Adhesion. Mol. Biol. Cell 21, 3070–3079.

Batchelder, E.L., Hollopeter, G., Campillo, C., Mezanges, X., Jorgensen, E.M., Nassoy, P., Sens, P., and Plastino, J. (2011). Membrane tension regulates motility by controlling lamellipodium organization. Proc. Natl. Acad. Sci. 108, 11429–11434.

Bates, M., Huang, B., Dempsey, G.T., and Zhuang, X. (2007). Multicolor super-resolution imaging with photo-switchable fluorescent probes. Science 317, 1749–1753.

Batta, G., Soltész, L., Kovács, T., Bozó, T., Mészár, Z., Kellermayer, M., Szöllosi, J., and Nagy, P. (2018). Alterations in the properties of the cell membrane due to glycosphingolipid accumulation in a model of Gaucher disease. Sci. Rep. 8, 1–13.

Boucrot, E., Saffarian, S., Zhang, R., and Kirchhausen, T. (2010). Roles of AP-2 in clathrin-mediated endocytosis. PLoS One 5.

Boulant, S., Kural, C., Zeeh, J.-C., Ubelmann, F., and Kirchhausen, T. (2011). Actin dynamics counteract membrane tension during clathrin-mediated endocytosis. Nat. Cell Biol. 13, 1124–1131.

Bretscher, M.S. (2014). Asymmetry of Single Cells and Where That Leads. Annu. Rev. Biochem. 83, 275–289.

Brodland, G.W., Veldhuis, J.H., Kim, S., Perrone, M., Mashburn, D., and Hutson, M.S. (2014). CellFIT: A cellular force-inference toolkit using curvilinear cell boundaries. PLoS One 9.

Bucher, D., Frey, F., Sochacki, K.A., Kummer, S., Bergeest, J.P., Godinez, W.J., Kräusslich, H.G., Rohr, K., Taraska, J.W., Schwarz, U.S., et al. (2018). Clathrin-Adaptor ratio and membrane tension regulate the flat-To-curved transition of the clathrin coat during endocytosis. Nat. Commun. 9.

Bustamante, C., Chemla, Y.R., Moffitt, J.R., Bustamante, C., Chemla, Y.R., and Moffitt, J.R. (2014). High-Resolution Dual-Trap Optical Tweezers with Differential Detection : Instrument Design High-Resolution Dual-Trap Optical Tweezers with Differential Detection : Instrument Design. 4, 1–9.

Cocucci, E., Aguet, F., Boulant, S., and Kirchhausen, T. (2012). The first five seconds in the life of a clathrin-coated pit. Cell 150, 495–507.

Cocucci, E., Gaudin, R., and Kirchhausen, T. (2014). Dynamin recruitment and membrane scission at the neck of a clathrin-coated pit. Mol. Biol. Cell 25, 3595–3609.

Collins, A., Warrington, A., Taylor, K.A., and Svitkina, T. (2011). Structural organization of the actin cytoskeleton at sites of clathrin-mediated endocytosis. Curr. Biol. 21, 1167–1175.

Conner, S.D., and Schmid, S.L. (2003). Regulated portals of entry into the cell. Nature 422, 37–44.

Cureton, D.K., Massol, R.H., Whelan, S.P.J., and Kirchhausen, T. (2010). The length of vesicular stomatitis virus particles dictates a need for actin assembly during clathrin-dependent endocytosis. PLoS Pathog. 6.

Dai, J., and Sheetz, M.P. (1995). Regulation of endocytosis, exocytosis, and shape by membrane tension. Cold Spring Harb. Symp. Quant. Biol. 60, 567–571.

Dai, J., Sheetz, M.P., Wan, X., and Morris, C.E. (1998). Membrane tension in swelling and shrinking molluscan neurons. J. Neurosci. 18, 6681–6692.

Dai, J., Ting-Beall, H.P., and Sheetz, M.P. (1997). The Secretion-coupled Endocytosis Correlates with Membrane Tension Changes in RBL 2H3 Cells. J. Gen. Physiol.

Dai, J., and Sheetz, M.P. (1999). Membrane tether formation from blebbing cells. Biophys. J. 77, 3363–3370.

Damke, H., Baba, T., Warnock, D.E., and Schmid, S.L. (1994). Induction of mutant dynamin specifically blocks endocytic coated vesicle formation. J. Cell Biol. 127, 915–934.

den Otter, W.K., and Briels, W.J. (2011). The Generation of Curved Clathrin Coats from Flat Plaques. Traffic 12, 1407–1416.

Desprat, N., Supatto, W., Pouille, P.A., Beaurepaire, E., and Farge, E. (2008). Tissue Deformation Modulates Twist Expression to Determine Anterior Midgut Differentiation in Drosophila Embryos. Dev. Cell 15, 470–477.

Diz-Muñ Oz, A., Fletcher, D.A., and Weiner, O.D. (2013). Use the force: membrane tension as an organizer of cell shape and motility.

Diz-Muñoz, A., Thurley, K., Chintamen, S., Altschuler, S.J., Wu, L.F., Fletcher, D.A., and Weiner, O.D. (2016). Membrane Tension Acts Through PLD2 and mTORC2 to Limit Actin Network Assembly During Neutrophil Migration. PLoS Biol. 14, 1–30.

Ducuing, A., and Vincent, S. (2016). The actin cable is dispensable in directing dorsal closure dynamics but neutralizes mechanical stress to prevent scarring in the Drosophila embryo. Nat. Cell Biol. 18, 1149–1160.

Ehrlich, M., Boll, W., van Oijen, A., Hariharan, R., Chandran, K., Nibert, M.L., and Kirchhausen, T. (2004). Endocytosis by Random Initiation and Stabilization of Clathrin-Coated Pits. Cell 118, 591–605.

Ferguson, J.P., Willy, N.M., Heidotting, S.P., Huber, S.D., Webber, M.J., and Kural, C. (2016). Deciphering dynamics of clathrin-mediated endocytosis in a living organism. J. Cell Biol. 214, 347–358.

Ferguson, J.P., Huber, S.D., Willy, N.M., Aygün, E., Goker, S., Atabey, T., and Kural, C. (2017). Mechanoregulation of clathrin-mediated endocytosis. J. Cell Sci. 130, 3631–3636.

Ferguson, S.M., Brasnjo, G., Hayashi, M., Wolfel, M., Collesi, C., Giovedi, S., Raimondi, A., Gong, L.-W., Ariel, P., Paradise, S., et al. (2007). A Selective Activity-Dependent Requirement for Dynamin 1 in Synaptic Vesicle Endocytosis. Science (80-.). 316, 570–574.

Fiolka, R., Shao, L., Rego, E.H., Davidson, M.W., and Gustafsson, M.G.L. (2012). Time-lapse two-color 3D imaging of live cells with doubled resolution using structured illumination. Proc. Natl. Acad. Sci. 109, 5311–5315.

Fogelson, B., and Mogilner, A. (2014). Computational estimates of membrane flow and tension gradient in motile cells. PLoS One 9.

Gaidarov, I., Santini, F., Warren, R.A., and Keen, J.H. (1999). Spatial control of coated-pit dynamics in living cells. Nat Cell Biol 1, 1–7.

Gauthier, N.C., Rossier, O.M., Mathur, A., Hone, J.C., and Sheetz, M.P. (2009). Plasma Membrane Area Increases with Spread Area by Exocytosis of a GPI-anchored Protein Compartment. Mol. Biol. Cell 20, 3261–3272.

Gauthier, N.C., Fardin, M.A., Roca-Cusachs, P., and Sheetz, M.P. (2011). Temporary increase in plasma membrane tension coordinates the activation of exocytosis and contraction during cell spreading. Proc. Natl. Acad. Sci. 108, 14467–14472.

Gauthier, N.C., Masters, T.A., and Sheetz, M.P. (2012). Mechanical feedback between membrane tension and dynamics. Trends Cell Biol. 22, 527–535.

Hassinger, J.E., Oster, G., Drubin, D.G., and Rangamani, P. (2017). Design principles for robust vesiculation in clathrin-mediated endocytosis. Proc. Natl. Acad. Sci. U. S. A. 114, E1118–E1127.

Herant, M., Heinrich, V., and Dembo, M. (2005). Mechanics of neutrophil phagocytosis: behavior of the cortical tension. J. Cell Sci. 118, 1789–1797.

Heuser, J. (1980). Three-dimensional visualization of coated vesicle formation in fibroblasts. J. Cell Biol. 84, 560–583.

Heuser, J.E., Keen, J.H., Amende, L.M., Lippoldt, R.E., and Prasad, K. (1987). Deep-etch visualization of 27S clathrin: A tetrahedral tetramer. J. Cell Biol. 105, 1999–2009.

Heuser, J. (1989). Effects of cytoplasmic acidification on clathrin lattice morphology. J. Cell Biol. 108, 401–411.

Hochmuth, R.M., Shao, J.Y., Dai, J., and Sheetz, M.P. (1996). Deformation and flow of membrane into tethers extracted from neuronal growth cones. Biophys. J. 70, 358–369.

Hong, S.H., Cortesio, C.L., and Drubin, D.G. (2015). Machine-Learning-Based Analysis in Genome-Edited Cells Reveals the Efficiency of Clathrin-Mediated Endocytosis. Cell Rep. 12, 2121–2130.

Houk, A.R., Jilkine, A., Mejean, C.O., Boltyanskiy, R., Dufresne, E.R., Angenent, S.B., Altschuler, S.J., Wu, L.F., and Weiner, O.D. (2012). Membrane tension maintains cell polarity by confining signals to the leading edge during neutrophil migration. Cell 148, 175–188.

Jacinto, A., Woolner, S., and Martin, P. (2002). Dynamic analysis of dorsal closure in Drosophila: From genetics to cell biology. Dev. Cell 3, 9–19.

Kaur, S., Fielding, A.B., Gassner, G., Carter, N.J., and Royle, S.J. (2014). An unmet actin requirement explains the mitotic inhibition of clathrin-mediated endocytosis. Elife 2014, 1–17.

Khatibzadeh, N., Gupta, S., Farrell, B., Brownell, W.E., and Anvari, B. (2012). Effects of cholesterol on nano-mechanical properties of the living cell plasma membrane. Soft Matter 8, 8350.

Kiehart, D.P., Galbraith, C.G., Edwards, K.A., Rickoll, W.L., and Montague, R.A. (2000). Multiple forces contribute to cell sheet morphogenesis for dorsal closure in Drosophila. J. Cell Biol. 149, 471–490.

Kirchhausen, T. (1993). Coated pits and coated vesicles - sorting it all out. Curr. Opin. Struct. Biol. 3, 182–188.

Kirchhausen, T. (2009). Imaging endocytic clathrin structures in living cells. Trends Cell Biol. 19, 596–605.

Kner, P., Chhun, B.B., Griffis, E.R., Winoto, L., and Gustafsson, M.G.L. (2009). Super-resolution video microscopy of live cells by structured illumination. Nat. Methods 6, 339–342.

Koenig, J.H. (1983). The Relationship Between the Number Amount of Transmitter Released of Synaptic Vesicles and the.

Koenig, J.H., and Ikeda, K. (1989). Disappearance and reformation of synaptic vesicle membrane upon transmitter release observed under reversible blockage of membrane retrieval. J. Neurosci. 9, 3844–3860.

Kural, C., and Kirchhausen, T. (2012). Live-cell imaging of clathrin coats (Elsevier Inc.).

Kural, C., Tacheva-Grigorova, S.K., Boulant, S., Cocucci, E., Baust, T., Duarte, D., and Kirchhausen, T. (2012). Dynamics of Intracellular Clathrin/AP1- and Clathrin/AP3-Containing Carriers. Cell Rep. 2, 1111–1119.

Kural, C., Akatay, A.A., Gaudin, R., Chen, B.-C., Legant, W.R., Betzig, E., and Kirchhausen, T. (2015). Asymmetric formation of coated pits on dorsal and ventral surfaces at the leading edges of motile cells and on protrusions of immobile cells. Mol. Biol. Cell 26, 2044–2053.

Lampe, M., Vassilopoulos, S., and Merrifield, C. (2016). Clathrin coated pits, plaques and adhesion. J. Struct. Biol. 196, 48–56.

Larkin, J.M., Donzell, W.C., and Anderson, R.G.W. (1986). Potassium-dependent assembly of coated pits: New coated pits form as planar clathrin lattices. J. Cell Biol. 103, 2619–2627.

Legoff, L., Rouault, H., and Lecuit, T. (2013). A global pattern of mechanical stress polarizes cell divisions and cell shape in the growing Drosophila wing disc. Development 140, 4051–4059.

Li, D., Shao, L., Chen, B.C., Zhang, X., Zhang, M., Moses, B., Milkie, D.E., Beach, J.R., Hammer, J.A., Pasham, M., et al. (2015). Extended-resolution structured illumination imaging of endocytic and cytoskeletal dynamics. Science (80-.). 349.

Lieber, A.D., Schweitzer, Y., Kozlov, M.M., and Keren, K. (2015). Front-to-rear membrane tension gradient in rapidly moving cells. Biophys. J. 108, 1599–1603.

Loebrich, S. (2014). The role of F-actin in modulating Clathrin-mediated endocytosis: Lessons from neurons in health and neuropsychiatric disorder. Commun. Integr. Biol. 7.

Loerke, D., Mettlen, M., Yarar, D., Jaqaman, K., Jaqaman, H., Danuser, G., and Schmid, S.L. (2009). Cargo and Dynamin Regulate Clathrin-Coated Pit Maturation. PLoS Biol. 7.

Ma, X., Lynch, H.E., Scully, P.C., and Hutson, M.S. (2009). Probing embryonic tissue mechanics with laser hole drilling. Phys. Biol. 6.

Masters, T.A., Pontes, B., Viasnoff, V., Li, Y., and Gauthier, N.C. (2013). Plasma membrane tension orchestrates membrane trafficking, cytoskeletal remodeling, and biochemical signaling during phagocytosis. Proc. Natl. Acad. Sci. 110, 11875–11880.

Merrifield, C.J., Feldman, M.E., Wan, L., and Almers, W. (2002). Imaging actin and dynamin recruitment during invagination of single clathrin-coated pits. Nat. Cell Biol. 4, 691–698.

Mettlen, M., Loerke, D., Yarar, D., Danuser, G., and Schmid, S.L. (2010). Cargo- and adaptor-specific mechanisms regulate clathrin-mediated endocytosis. J. Cell Biol. 188, 919–933.

Mettlen, M., and Danuser, G. (2014). Imaging and Modeling the Dynamics of Clathrin-Mediated Endocytosis. Cold Spring Harb. Perspect. Biol. 6, a017038–a017038.

Miller, S.E., Mathiasen, S., Bright, N.A., Pierre, F., Kelly, B.T., Kladt, N., Schauss, A., Merrifield, C.J., Stamou, D., Höning, S., et al. (2015). CALM Regulates Clathrin-Coated Vesicle Size and Maturation by Directly Sensing and Driving Membrane Curvature. Dev. Cell 33, 163–175.

Musacchio, A., Smith, C.J., Roseman, A.M., Harrison, S.C., Kirchhausen, T., and Pearse, B.M.F. (1999). Functional organization of clathrin in coats: Combining electron cryomicroscopy and x-ray crystallography. Mol. Cell 3, 761–770.

Pasakarnis, L., Frei, E., Caussinus, E., Affolter, M., and Brunner, D. (2016). Amnioserosa cell constriction but not epidermal actin cable tension autonomously drives dorsal closure. Nat. Cell Biol. 18, 1161–1172.

Pouille, P.A., Ahmadi, P., Brunet, A.C., and Farge, E. (2009). Mechanical signals trigger myosin II redistribution and mesoderm invagination in drosophila embryos. Sci. Signal. 2, 1–9.

Raucher, D., and Sheetz, M.P. (1999). Membrane expansion increases endocytosis rate during mitosis. J. Cell Biol.

Rauskolb, C., Sun, S., Sun, G., Pan, Y., and Irvine, K.D. (2014). Cytoskeletal tension inhibits Hippo signaling through an Ajuba-Warts complex. Cell 158, 143–156.

Robinson, M.S. (2015). Forty Years of Clathrin-coated Vesicles. Traffic 16, 1210–1238.

Saffarian, S., and Kirchhausen, T. (2008). Differential evanescence nanometry: Live-cell fluorescence measurements with 10-nm axial resolution on the plasma membrane. Biophys. J. 94, 2333–2342.

Saffarian, S., Cocucci, E., and Kirchhausen, T. (2009). Distinct dynamics of endocytic clathrin-coated pits and coated plaques. PLoS Biol. 7.

Saias, L., Swoger, J., D'Angelo, A., Hayes, P., Colombelli, J., Sharpe, J., Salbreux, G., and Solon, J. (2015). Decrease in Cell Volume Generates Contractile Forces Driving Dorsal Closure. Dev. Cell 33, 611–621.

Saleem, M., Morlot, S., Hohendahl, A., Manzi, J., Lenz, M., and Roux, A. (2015). A balance between membrane elasticity and polymerization energy sets the shape of spherical clathrin coats. Nat. Commun. 6, 6249.

Schmid, S.L. (1997). CLATHRIN-COATED VESICLE FORMATION AND PROTEIN SORTING:An Integrated Process. Annu. Rev. Biochem. 66, 511–548.

Scott, B.L., Sochacki, K.A., Low-Nam, S.T., Bailey, E.M., Luu, Q., Hor, A., Dickey, A.M., Smith, S., Kerkvliet, J.G., Taraska, J.W., et al. (2018). Membrane bending occurs at all stages of clathrin-coat assembly and defines endocytic dynamics. Nat. Commun. 9, 419.

Sheetz, M.P. (2001). Cell control by membrane – cytoskeleton adhesion. Nature 2, 366–369.

Shraiman, B.I. (1997). On the role of assembly kinetics in determining the structure of clathrin cages. Biophys. J. 72, 953–957.

Snijder, B., Sacher, R., Rämö, P., Damm, E.M., Liberali, P., and Pelkmans, L. (2009). Population context determines cell-to-cell variability in endocytosis and virus infection. Nature 461, 520–523.

Sochacki, K.A., Dickey, A.M., Strub, M.P., and Taraska, J.W. (2017). Endocytic proteins are partitioned at the edge of the clathrin lattice in mammalian cells. Nat. Cell Biol. 19, 352–361.

Solon, J., Kaya-Çopur, A., Colombelli, J., and Brunner, D. (2009). Pulsed Forces Timed by a Ratchet-like Mechanism Drive Directed Tissue Movement during Dorsal Closure. Cell 137, 1331–1342.

Subtil, A., Gaidarov, I., Kobylarz, K., Lampson, M.A., Keen, J.H., and McGraw, T.E. (1999). Acute cholesterol depletion inhibits clathrin-coated pit budding. Proc. Natl. Acad. Sci. 96, 6775–6780.

Sun, M., Northup, N., Marga, F., Huber, T., Byfield, F.J., Levitan, I., and Forgacs, G. (2007). The effect of cellular cholesterol on membrane-cytoskeleton adhesion. J. Cell Sci. 120, 2223–2231.

Tan, X., Heureaux, J., and Liu, A.P. (2015). Cell spreading area regulates clathrin-coated pit dynamics on micropatterned substrate. Integr. Biol. 7, 1033–1043.

Taylor, M.J., Perrais, D., and Merrifield, C.J. (2011). A high precision survey of the molecular dynamics of mammalian clathrin-mediated endocytosis. PLoS Biol. 9.

Toomre, DK, Langhorst, MF, Davidson, MW, n.d., Spinning disk confocal microscopy, figure, viewed 17 July 2018, <http://zeiss-campus.magnet.fsu.edu/articles/spinningdisk/introduction.html>

Tsujita, K., Takenawa, T., and Itoh, T. (2015). Feedback regulation between plasma membrane tension and membrane-bending proteins organizes cell polarity during leading edge formation. Nat. Cell Biol. 17, 749–758.

Tucker, P.K.P., Evans, I.I.R., and Wood, W. (2011). Ena drives invasive macrophage migration in Drosophila embryos. Dis. Model. Mech. 4, 126–134.

Willy, N.M., Ferguson, J.P., Huber, S.D., Heidotting, S.P., Aygün, E., Wurm, S.A., Johnston-Halperin, E., Poirier, M.G., and Kural, C. (2017). Membrane mechanics govern spatiotemporal heterogeneity of endocytic clathrin coat dynamics. Mol. Biol. Cell 28, 3480–3488.

Appendix A Micropipette Aspiration

Micropipette aspiration experiments proved to be difficult with our mostly borrowed tools. I must give thanks to Dr. Chris Hammel for lending us the pipette puller, Dr. Paul Selvin for lending us the micromanipulator and microaspirator, and Dr. Candice Askwith for allowing us to use her microforge.

The first hurdle was to attach the micromanipulator to our microscope so that we can perform experiments while imaging. We attempted to purchase a product from the microscope manufacturer for this purpose, but found that it did not work with the attachments we already had. I had been trained in usage of the student machine shop for situations such as this, so I produced the necessary parts from scrap metal in the shop.

The next difficulty was to develop pipettes ideal for applying suction. I located a recipe guide for the micropipette puller to turn a solid piece of capillary glass (Borosilicate glass with a 1mm outer diameter and 0.58mm inner diameter) into a pair of pipettes with specific tip shapes. Unfortunately, the recipe guide did not have all of the details we required so it took a significant amount of trial and error to develop successful tips. And even then there was large risk of breaking the fine tip with an outer diameter of ~10μm and inner diameter of ~3μm, so duplicates had to be prepared regularly. For future reference, the recipe I had most success with is stored at recipe number 81 in the

machine with a heat of 480, no pulling force, velocity of 120, and time of 200. At one point, we tried using a microforge to fine-tune the final parameters of the pipette tip. However, the number of tips we had to produce, combined with the journey to another lab to use the microforge, meant that this procedure was saved for unique experiments that failed to reach publication.

The last challenge was to position the tip correctly during the experiment. The only visual aid the user has is the vague visual distortion provided by a clear object, the size of which is significantly larger than the depth-of-field of the optics. The first sight is made by the shadow cast by the pipette tip on the objective while scanning the tip over the objective. Once the shadow located, the user can put the focus significantly above the cell samples by ~100μm, so that the tip can be lowered into focus safely away from the cells. A visual inspection can verify the orientation of the tip and if it needs adjustment. The tips usually separate from the pipette puller with a slight bevel and it is ideal to have the flattest side of the tip facing the cell. If necessary, it is recommended to lift the tip a safe distance away from the cells before rotating it to the correct orientation. Once the tip is located, the user can position it at a known place in the field of view. All of this is done using the white light. Once the tip position is known, the user can switch to laser illumination to locate a cell, as control of the cell stage is independent of the micromanipulator.

During imaging, the pipette tip is lowered as slowly as possible until there is a visual perturbation of the cell in the fluorescence channel signifying contact. The user may now apply suction according to the experimental condition.

The machine was never calibrated, so an absolute measurement of applied pressure was never achieved. Additionally, the capillary forces involved were unpredictable, so it is unclear if we ever successfully reached an equilibrium pressure. The result is that experiments lacked consistency, so comparisons needed to be made in bulk, i.e. suction or no suction, and cells with wildly aberrant behavior were excluded due to variability in suction pressure and cell contact.

Appendix B Three Dimensional Tracking

I developed the 3D tracking algorithm based on the state-of-the-art 2D tracking code provided by Auget et al. (2013). The basic premise is that we would perform experiments where significant fluorescent puncta could be detected in more than one plane of a 3D time-lapse acquisition. The data would be analyzed as a series of 2D time-lapse datasets for each z-position (stacks), and traces would be linked in the z-dimension dimension based on significant adjacency in the x-y plane. However, the computation time required to determine adjacency of each trace grows as the number of traces in one stack multiplied by the number of traces in the other stack, i.e. $O(n^2)$ in big O notation. The number of traces in each stack was prohibitive to this methodology.

However, MATLAB is very efficient at performing matrix operations. So if the positions of traces could be represented as points on a discrete matrix the comparison could be performed much faster as element-wise matrix multiplication. The last problem is to link the traces in the 2D matrix to traces in our database. The solution to each of these problems is to represent each trace as a value in a 2D matrix where the value is the nth prime number and n is its unique position among all traces in all stacks. The position is discretized so that where there is no trace the value in the matrix is zero. In this way,

the values from the product matrix can be factorized to identify the two contributing traces. The two traces can then be linked based on the criteria provided in section 2.5.4.

This method saves computation time because previously all traces in one stack had to be compared with all traces of the other stack to check for adjacency. With this method the adjacency is a byproduct of the element-wise multiplication so only adjacent traces need be factorized. Performing the factorization where it is known to contain exactly 2 relatively small factors is also very quick.

The principle downside to this method is that all of the stacks must be run separately through the 2D tracking algorithm. It is possible there could be more significant speed increases and greater accuracy by developing a 3D tracking algorithm. The group who developed the 2D tracking algorithm have since developed a 3D tracking algorithm, but the work is unpublished and the documentation is non-existent. Nevertheless, the algorithm presented here may already be obsolete when a future student in the lab deciphers how to use the new 3D tracking algoritm.